

AMERICAN UNIVERSITY OF BEIRUT

CURE CYCLE IN-PROCESS MONITORING OF ADVANCED
COMPOSITES VIA REUSABLE FLEXIBLE ULTRASONIC
SENSING FILM

by
ELIE NEHME MAHFOUD

A dissertation
submitted in partial fulfillment of the requirements
for the degree of Doctor of Philosophy
to the Department of Mechanical Engineering
of the Maroun Semaan Faculty of Engineering and Architecture
at the American University of Beirut

Beirut, Lebanon
January 2023

AMERICAN UNIVERSITY OF BEIRUT

CURE CYCLE IN-PROCESS MONITORING OF ADVANCED
COMPOSITES VIA REUSABLE FLEXIBLE ULTRASONIC
SENSING FILM

by
ELIE NEHME MAHFOUD

Approved by:



Signature

Dr. Mohammad Said Harb, Assistant Professor
Department of Mechanical Engineering

Advisor



Signature

Dr. Kamel Abu Ghali, Professor
Department of Mechanical Engineering

Chair of Committee



Signature

Dr. Samir Mustapha, Associate Professor
Department of Mechanical Engineering

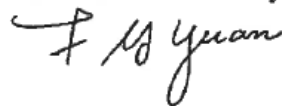
Member of Committee



Signature

Dr. Ali Abdul-Aziz, Associate Professor
College of Aeronautics and Engineering
Kent State University

Member of Committee
(Co-Advisor)



Signature

Dr. Fuh-Gwo Yuan, Professor
Mechanical and Aerospace Engineering
NC State University

Member of Committee

Date of dissertation defense: January 24, 2023

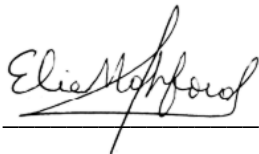
AMERICAN UNIVERSITY OF BEIRUT

DISSERTATION RELEASE FORM

Student Name: Mahfoud Elie Nehme
 Last First Middle

I authorize the American University of Beirut, to: (a) reproduce hard or electronic copies of my dissertation; (b) include such copies in the archives and digital repositories of the University; and (c) make freely available such copies to third parties for research or educational purposes:

- As of the date of submission
- One year from the date of submission of my dissertation.
- Two years from the date of submission of my dissertation.
- Three years from the date of submission of my dissertation.



February 7, 2023

Signature

Date

ACKNOWLEDGEMENTS

First and foremost, this dissertation is dedicated to my advisor Dr. Mohammad Harb. During my time at AUB, Dr. Harb has been my mentor, friend, and big brother. He has supervised my transition to an independent researcher, and taught me that research is about much more than just doing the work. I want him to know that he has trained a doctoral student to succeed in life, and not just in profession. For that, I will always be grateful for his patience and trust.

This work would have never been possible without all the help I had from faculty, staff, and fellow students. I would like to thank Dr. Samir Mustapha for his guidance and kind words throughout this period. I've always considered him as my second advisor. I would also like to thank the lab managers, especially Mr. Ghassan Deeb, Mr. Dory Rouhana, and Mr. Hisham Ghalayini, for their laboratory assistance and trust in handling equipment and having access to the needed labs. I spent most of my working time in Oxy 409 where both undergraduate and graduate students worked on their projects/research. We hung out together, laughed, and learned from each other. I want to thank all colleagues and friends I met in this small space, especially Jad El Najjar and Rawad Malaeb.

I would like to thank the committee members, the department of Mechanical Engineering, and the Maroun Semaan Faculty of Engineering and Architecture at AUB for this generous opportunity which spread over five and a half years. A special thanks to Mrs. Nancy Batakji for her kind administrative help.

To my small circle of friends and family, you are the reason I held on and succeeded. To Michel and Ibrahim, to the good times we have during this country's worst years. To my sister, to Ziad, Mays, and Samir, thank you for the joy you bring to our home. To my brother, thank you for all the help you provide while you are away. To the Wehbes, my extended family, your generous chaos give me a new perspective on love. To my father, my backbone, your hard work is what motivates me. You have always been certain of my success. To my mother, my all, to our 'sebhiye' on the weekends. You define giving. You give your all so we can be happy and at comfort. This is for all the worry you have regarding what and when I eat, for all the stitches you repair, and for all the love you generously spread. To Coco, to the sunlight that shone two years ago. Your sense of wonder awakened mine, and you gave me a new meaning for life. May your loving soul never fade. May you stay in my heart, forever. To Rim, to the fire in my heart, to the reason I smile. You are me in another universe. We don't believe in a customary god, but I believe we were sent here to find each other, be together, for eternity. To our road-trips back and forth, to our lives here and there, to our little home. To our dinners, to our fights, to our laughter. Thank you for all you keep doing for us. This is for you, just as I am.

Lastly, I devote this to myself, my own being. I want to thank myself for bearing with my own thoughts during the most difficult times. This is for all the fear of failure, all the loneliness of the 312 abyss at dawn. This is for me, a reminder that I am always worthy.

ABSTRACT

Elie Nehme Mahfoud

for

Doctor of Philosophy

Major: Mechanical Engineering

Title: Cure Cycle In-process Monitoring of Advanced Composites via Reusable Flexible Ultrasonic Sensing Film

Environmental and cost-saving advantages derived from the use of composites attract the aerospace and automotive industries as these materials offer significant structural and aerodynamic advantages over traditional metal structures. The composites industry, however, is concerned with the manufacturing processes as they cannot provide fast enough cycle time to match metal alloy processes. This research aims to develop a sensing technology in the form of a reusable in-situ cure monitoring and assessment system that can predict the formation of manufacturing defects and monitor the degree of cure.

First, a thin-film material is chosen from various PTFE-based material by prioritizing the debonding effect and signal transmission through the composite part. Then, the film is used to sandwich piezoelectric actuators and sensors to monitor out-of-autoclave carbon fiber composite plates using ultrasonic Lamb waves by temporarily adhering to the manufactured part creating an effective electromechanical coupling between the sensing film and the laminate. Initial results, through the analysis of the fundamental antisymmetric A_0 mode at low frequencies, indicate that analyzing the velocity and amplitude of these waves over cure time determines minimum viscosity, gelation, and vitrification points. Experimental results also prove the feasibility of using such a reusable film for different post-curing cycles, always determining certain cure parameters.

Since some of the concerns this industry faces are the energy and time spent on long curing cycles to achieve permanent bonding between the matrix and fibers, the reusable PTFE thin sensing film is then used to monitor the same cure parameters for a shorter curing cycle than that suggested by the CFRP manufacturer. The results show that the determined three cure parameters are offset by the same time deducted from the cycle, highlighting the practicability of using such technology. To verify the viability of this approach, tensile testing and dynamic mechanical analysis (DMA) are performed on these composites. Tensile testing results show that the average tensile modulus for the shortened cycle is of similar values if not slightly higher than that of the normal cycle. DMA results verify both previous conclusions: time shift of cure parameters and enhanced mechanical and thermal properties of the shortened cycle.

With the help of DMA results, a computational model for the CFRP plate is developed to imitate the experimental in-process monitoring. The storage modulus for the used CFRP is extracted throughout the curing cycle and its trend is implemented into COMSOL combined structural and electrostatics multiphysics to simulate the same mechanical fluctuations of the CFRP during curing. Then, Lamb waves are excited and sensed via sandwiched piezoelectric transducers in a reusable PTFE sensing film to monitor the structural health of the structure. The three cure parameters are determined for both curing

cycles, validating the efficiency of this numerical method. Also, while closely analyzing these computationally-generated curves, an additional cure parameter defined as “gelation initiation” is proposed. Additionally, the decomposition of different wavefield modes is scrutinized to describe their scattering throughout the layered structure. A new entrapped antisymmetric mode appears inside the CFRP laminate at the start of the cure, which suggests that the previously studied A_0 mode had been initially converted from the CFRP S_0 mode.

Finally, the curing of adhesives used for structural bonding is monitored. By joining two fully cured CFRP plates with a prepreg epoxy film to be cured in the oven, the same previous methods are used to analyse the data extracted from the ultrasound monitoring of this adhesive. Additional S_0A_0 mode that is converted at the overlap is also analyzed. Then, post-cure monitoring on the CFRP plates is performed to remove the effect of heat and determine more accurate cure parameters. In the numerical model, sole A_0 mode is actuated to enhance the scrutiny of mode conversion at the overlap. The numerical results, although heavily dependent on the adhesive film DMA curing results input, still highlight the desired cure points. Lastly, cocuring of both adhesive film and non-cured CFRP prepreg laminates is also tested experimentally where the A_0 amplitude curve show more sensitivity towards the added epoxy cure parameters.

TABLE OF CONTENTS

ACKNOWLEDGEMENTS	1
ABSTRACT	2
ILLUSTRATIONS	7
TABLES	12
INTRODUCTION AND BACKGROUND.....	13
1.1. Motivation.....	13
1.2. Traditional Cure Monitoring.....	14
1.3. Ultrasonic Cure Monitoring.....	16
1.4. Computational Cure Monitoring.....	18
1.5. Length of the Curing Cycle	20
1.6. Background for Thin Film Material Selection.....	21
1.7. Lamb Waves Fundamentals.....	22
1.8. Objectives and Outline.....	26
MATERIAL SELECTION AND IN-PROCESS MONITORING..	
.....	29
2.1. Material Selection	29
2.1.1. Bonding Test	29
2.1.2. Signal Transmission	30
2.2. Cure Cycle Monitoring	35

2.2.1.	Experimental Setup	35
2.2.2.	Results	39
2.2.2.1.	Trendline Analysis and Comparison	41
2.2.2.2.	Post-cure Monitoring	47
2.3.	Sensing Feasibility of the Proposed System	50
2.4.	Summary	52
CURE CYCLE SHORTENING		54
3.1.	Ultrasonic Non-Destructive Testing	54
3.2.	Tensile Testing	58
3.3.	Dynamic Mechanical Analysis	61
3.4.	Summary	70
NUMERICAL MODELING		72
4.1.	Experimental Cure Monitoring	73
4.2.	Computational Modeling	79
4.2.1.	Material Properties	79
4.2.2.	Combined Modules and Numerical Solving	82
4.2.3.	Results	89
4.3.	Discussion	93
4.3.1.	Viscoelastic Considerations	93
4.3.2.	Lamb Wavefields	95
4.3.3.	Added Cure Parameter	99
4.3.4.	Study Limitations	103

4.3.5.	Practical Importance of the Numerical Model	104
4.4.	Summary	106
CURE MONITORING OF ADHESIVE FILMS AND COCURE MONITORING WITH CFRP LAMINATES		108
5.1.	Background	108
5.2.	Experimental Adhesive Cure Monitoring	113
5.2.1.	CFRP Post-cure Monitoring	117
5.2.2.	Removal of CFRP Temperature Effect	119
5.3.	Numerical Adhesive Cure Monitoring	121
5.3.1.	Adhesive Film DMA Curing	121
5.3.2.	Numerical Model Input and Results	122
5.4.	Cocuring	127
5.5.	Summary	131
CONCLUSIONS AND FUTURE WORK		133
REFERENCES		138

ILLUSTRATIONS

Figure 1.1: Displacement of particles in an (a) antisymmetric and (b) symmetric Lamb wave modes. The median dotted line of the plate is shown. [71].....	23
Figure 1.2: (a) Tuning curves showing voltage amplitude of each mode vs frequency, and (b) dispersion curves showing group velocity of each mode vs frequency, both for the cured 1mm-thick unidirectional CFRP plate	26
Figure 2.1: Thin film specimens (a) before and (b) after peel test.	30
Figure 2.2: Experimental setup for signal intensity measurement using sandwiched PZTs (not drawn to scale).	32
Figure 2.3: Normalized amplitude for S_0 mode at 250 kHz for the different materials in all three cases where Sandwiched PZTs act as (a) Actuators and (b) Sensors.	33
Figure 2.4: Second signal transmission setup at the center of a 1000 x 1000 mm ² Al-1050 plate. In this figure: B is Glass cloth PTFE, C is Skived PTFE and D is Cast PTFE.	33
Figure 2.5: Sensed signals by the bare PZTs when actuated from the sandwiched ones with excitation frequencies of (a) 100 kHz and (b) 200 kHz.....	35
Figure 2.6: Cure cycle of the out-of-autoclave prepreg as proposed by the manufacturer.	37
Figure 2.7: First cure monitoring experiment setup showing different paths that are tracked for each actuator-sensor.	38
Figure 2.8: Measured signal from the PTFE sandwiched actuator-sensor film at 10 mins into the curing cycle.....	40
Figure 2.9: (a) Group velocity and (b) Voltage of A_0 mode generated and received by the skived PTFE sandwiched PZTs over the $[0]_3$ unidirectional laminate.	40
Figure 2.10: (a) Group velocity and (b) Voltage of A_0 mode generated and received along different paths in the first cure monitoring experiment.	43
Figure 2.11: Group velocity and Voltage of A_0 and S_0 mode generated and received over the $[0]_3$ unidirectional laminate.	45
Figure 2.12: Raw data points from the <i>UNIact</i> – <i>UNIsen</i> path showing the wave behavior before and after Vitrification.	46

Figure 2.13: Group velocity and Voltage of A_0 and S_0 mode generated and received over the [0/90/0] woven laminate.	47
Figure 2.14: (a) Group velocity and (b) Voltage of A_0 mode generated and received along different already-cured material.	49
Figure 2.15: Group velocity and Voltage of A_0 mode generated and received over the [0/90/0] woven laminate for the 4hr-soak and 3hr-soak experiments.	52
Figure 3.1: Cure cycle proposed by the manufacturer (4hr-soak) and the shortened cycle tested (3hr-soak) shown with vacuum pressure in an out-of-autoclave setup.	55
Figure 3.2: Raw data points from the curing experiment comparing cure stages for both cycles.	56
Figure 3.3: Some samples after cure and trim, before tensile testing.	59
Figure 3.4: Stress-Strain curves for four random tensile-tested specimens.	59
Figure 3.5: Results of the tensile test for all specimens for both cure cycles.	61
Figure 3.6: Setup of DMA experiments showing the specimen in single cantilever mode.	63
Figure 3.7: DMA results showing loss factor, gain and loss moduli vs cure time for both cycles.	63
Figure 3.8: DMA temperature ramp results for oven-cured specimens showing averaged storage modulus and $\tan \delta$ curves for both cycles.	68
Figure 3.9: Creep test results for (a) all specimens from both cycles, and (b) averaged curves for each cycle, also showing temperature and loading schemes.	69
Figure 4.1: Layup process of the CFRP composite along with the described sensing film layers.	74
Figure 4.2: DMA 4hr-soak curing results for the woven CFRP specimens tested with the shown frequencies.	76
Figure 4.3: The amplified DMA storage modulus average curves for both cycles that are implemented into the computational model.	78
Figure 4.4: Segmented DMA results that are implemented into COMSOL for a parametric study on the mechanical properties of the woven CFRP. (a) Shows E_1 and E_2 for the 4hr-soak cure cycle segmented directly from the averaged E' curve, (b) shows the v_{23} and v_{13} curves for the 4hr-soak cycle based on literature and adjusted proportionally for the rubbery and glassy regions from their fully cured value, and (c)	

shows the density variations during curing based on chemical shrinkage and thermal expansion variations.	82
Figure 4.5: Geometry created using the aided design within COMSOL. The parts are spaced from each other in the z-direction only for the purpose of demonstration in this image.....	84
Figure 4.6: The fully meshed model with a maximum element size of 3 mm. There are 4443, 10432, and 39756 tetrahedrons, prisms, and hexahedrons, respectively present in the model, totaling at around 55E+3 elements.	87
Figure 4.7: An algorithm showing the steps taken before and during solving the computational model.....	88
Figure 4.8: Computational signal for the fully cured state of the 4hr-soak cycle with and without PTFE film.	90
Figure 4.9: Comparing numerically computed signals from COMSOL to raw experimental data.	91
Figure 4.10: (a) Group velocity and (b) Amplitude of the first received A_0 mode packet for both curing cycles extracted from the numerical model simulations.....	93
Figure 4.11: Signal comparison for the fully cured 4hr-soak cycle CFRP with and without viscoelastic considerations derived from literature.	94
Figure 4.12: Upper and lower views of the Lamb waves velocity profiles inside the PTFE-CFRP-Aluminum structure at 450 min cure time for the 4hr-soak cycle along the (a) X velocity component, and (b) Z velocity component.....	97
Figure 4.13: Upper and lower views of the Lamb waves velocity profiles inside the PTFE-CFRP-Aluminum structure at 10 min cure time for the 3hr-soak cycle along the (a) X velocity component, and (b) Z velocity component.....	99
Figure 4.14: Rearrangement of the gelation and vitrification cure parameters points for the numerical results. (a) and (b) show, respectively, the group velocity and voltage curves vs experimental cure time. (c) and (d) show, respectively, the numerically generated group velocity and voltage curves vs FEA cure time.....	101
Figure 4.15: Rearranged states for the DMA 4hr-soak curing results of the woven CFRP specimens tested with different frequencies. The rearrangement includes the new assumed “gelation initiation” cure parameter where the rubbery region starts. The relocated vitrification point also shifts the rubbery region end / glassy region start. ...	103
Figure 4.16: Progress of reaction (POR) curves normalized vs cure time as derived from (a) group velocity curves and (b) voltage curves. These results are shown for both cycles experimentally and numerically.....	105

Figure 5.1: (a) Actuated and sensed signals by the inclusion of a second PZT actuator to transmit one mode only, either A_0 or S_0 . The mode conversion occurs in both cases. (b) Pristine sensed signal through actuated wave propagation vs the reconstructed signal by adding the two S_0 - and A_0 -actuated signals.	111
Figure 5.2: (a) Solely S_0 -actuated signal and (b) solely A_0 -actuated signal, seen by the y-direction velocities at two different times to emphasis on the mode conversion phenomenon in each case.	112
Figure 5.3: Experimental setup of the adhesive film cure monitoring (a) before the two fully cured woven CFRP plates are overlapped, and (b) after they are adhered to each other and the PZTs are installed. The setup is put under vacuum after these steps.....	113
Figure 5.4: The cure cycle implemented for adhesive film curing. At 32 min, the oven temperature reaches 120°C , since the ramp starts at 25°C and the heat rate $\approx 3^{\circ}\text{C}/\text{min}$. Cooling data reaches 214 min but not all shown experiments in this section reach that much cooling time.	114
Figure 5.5: The adhesive film experimental cure monitoring results showing (a) the voltage curves for all three studied modes, and the group velocity curves vs cure time for (b) the S_0 mode, (c) the A_0 mode, and (d) the S_0A_0 mode. The minima, maxima, and onsets of interest are marked in black along with each specific time colored to its corresponding mode curve.....	115
Figure 5.6: CFRP post-cure monitoring results showing the voltages curves for (a) S_0 and (b) A_0 , and the velocity curves for (c) S_0 and (d) A_0	118
Figure 5.7: The adhesive film experimental cure monitoring results after proportionally deducting the thermal effect on CFRP post-curing from each curve, respectively. The figure shows the voltages curves for (a) S_0 and (b) A_0 , and the velocity curves for (c) S_0 and (d) A_0 . Since The S_0A_0 mode is not studied in the same post-curing CFRP fashion, its curves are not included in this figure.	119
Figure 5.8: DMA curing temperature curve with natural cooling and storage modulus curve results of five tested adhesive film specimens.	122
Figure 5.9: Imported material properties of the adhesive film into the numerical model where (a) shows the Young's modulus and (b) shows the Poisson's ratio, both vs the numerical cure time.	123
Figure 5.10: Imported material properties for the post-cured CFRP into the numerical model where (a) shows the E_{11} and E_{22} moduli, (b) shows the G_{13} and E_{33} moduli, (c) shows the ν_{12} Poisson's ratio, and (d) shows the ν_{13} and ν_{23} ratios, all vs FEA cure time. Note that G_{12} follows the trend seen in (a) proportional to 7 GPa and G_{23} follows the trend seen in (b) proportional to 4 GPa.....	125

Figure 5.11: Numerical simulations results in the form of voltage curves for (a) A_0 mode and (b) A_0S_0 mode, and velocity curves for (c) A_0 mode and (d) A_0S_0 mode. The minima, maxima, and onsets of interest are marked in black along with each specific time colored to its corresponding mode curve. 126

Figure 5.12: The cocuring experiment setup with the PTFE sensing film on top of the CFRP-adhesive-CFRP structure. 127

Figure 5.13: The cure cycle oven temperature data collected each five minutes vs cure time. A 10 mins threshold is maintained at the start to replicate the CFRP cure monitoring experiments in previous chapters. Thus, 70°C is reached at 60 min and its soak is done at 240 min, while 120°C is reached at 265 min and its soak is over at 325 min. 128

Figure 5.14: Cocuring results showing voltage and velocity curves for both S_0 and A_0 modes. The S_0A_0 mode is not as distinguishable as previously seen in the adhesive monitoring experiment because the antisymmetric mode is passing through the aluminum tooling plate and is faster than what S_0A_0 would be, thus it is not included in the analysis. Points of interest are marked in black. 129

TABLES

Table 2.1: Thin film material used and peeling test results.	30
Table 2.2: Number of cases recording highest amplitude for S_0 and A_0 Lamb wave mode at 100 and 200 kHz for different thin film materials.	35
Table 3.1: Averaged tensile modulus and tensile strength for both cure cycles.....	61
Table 3.2: Cure parameters deduced from DMA experiment comparing 4hr-soak and 3hr-soak cycles.	65
Table 3.3: Averaged modulus and T_g results for specimens cured in 4hr-soak and 3hr-soak cycles.	67
Table 4.1: The required properties in COMSOL for the present isotropic materials.	79
Table 4.2: Final cured state CFRP mechanical properties for each cycle.	80
Table 4.3: Comparison between the computation time of each ‘solver - step method’ combination.	87

CHAPTER 1

INTRODUCTION AND BACKGROUND

1.1. Motivation

The composites industry has been growing exponentially in the past two decades. According to Holmes [1], the global market size of this industry reached 1.82 billion dollars at the beginning of 2019. This fast growth indicates that various companies are realizing the advantages of this material and are incorporating it in numerous applications from sports equipment to the aerospace industry. The inclusion of fiber reinforced polymers (FRPs) in the automotive industry has expanded from high-end niche vehicles to more affordable commercial cars and motorcycles. The presence of carbon FRPs (CFRPs) in these vehicles is estimated to reduce the latter's weight by 30 to 50%. [2] For example, the latest models in civil aviation, such as the Boeing Dreamliner and Airbus A350, are made of up to 52% CFRP. [3] This weight reduction has a remarkable impact on fuel efficiency and reductions in greenhouse gas emissions. In addition, CFRPs provide high specific strength and stiffness, corrosion and electrical resistance, low thermal expansion, good vibration damping characteristics, and superior fatigue and wear resistance than traditional metals. [4] However, manufacturers still struggle with its production time as the curing cycles are often established based on trial and error and are not optimized to their highest potential as they suffer from high safety factors that these companies establish. [5] This struggle directly affects the consumers' post-cure processing and finishing required hence setting a drawback for the whole composites industry. Reducing this unwanted large safety factor can lead to faster manufacturing of CFRPs which innately makes them more popular with many industries. [6] Another problem that the composites industry faces is the defects within

the composites coming from high porosity levels during manufacturing, and air gaps-induced delaminations occurring during the curing process. [7] Porosity is the bulk of many micro-voids which are induced from wetness or trapped air that, when culminating together, reduce the mechanical properties of the cured composite. [8] Hence, the need for more methods to monitor and evaluate the curing process of carbon fiber composites is growing as these problems require a system that can effectively monitor the composites in real-time during curing while tracking defects and/or damage inside the parts. Several methods already exist for the monitoring of the curing process of the composites. Bekas et al. [9] fabricated a multi-functional sensor consisting of inkjet-printed silver-based circuits and interdigital sensors for the structural health monitoring of a bonded composites repair without weight addition. Whereas Scheerer et al. [10] made a piezo-temperature sensor to be integrated in the manufacturing process of resin transfer moulding (RTM). The goal of this work is to develop such a system that monitors the composite laminates during traditional curing inside an oven while being reusable to lower the cost and material consumption.

1.2. Traditional Cure Monitoring

Cure monitoring is any established process during which a designated material property is measured to evaluate the degree of cure. [11] Established resin cure monitoring methods such as dynamic mechanical analysis (DMA), differential scanning calorimetry (DSC), thermogravimetric analysis (TGA), rheology, and dielectric analysis (DEA) are widely used but mostly limited to a lab setup under ideal conditions and are not feasible to be used at an industrial production and processing level. [12] They are still important, however, as they provide high quality information about glass transition

temperature (T_g), resin viscosity flow, formation of gel and overall crosslinking, cure onsets, completion of cure, and degree of cure. [13] These methods also give several cure parameters in function of time such as minimum viscosity of the polymer, gelation (cross-linking), and vitrification (glassy state) points. [14,15]

Stark et al. [16] tested different carbon fiber samples using DMA under different heating rates, damping frequencies, and overall ramp cycle to study the dependency of the liquid, rubbery, and glassy states to these changes. Braun et al. [17] analyzed molecular processes of an epoxy resin during curing using Fourier transform infrared (FTIR) by DSC and TGA. In-situ measurements identified curing reactions and the effect of temperature on these reactions was studied. Sawicz-Kryniger et al. [18] recently compared and evaluated the performances of Fluorescence probe technique (FPT), DSC, and FTIR in real time epoxy cure monitoring. The new FPT method had an on-line monitoring potential and was found less costly in consumables and instrumentational preparations. Kister and Dossi [19] established a baseline study for cure monitoring CFRP composites inside a DMA machine in a single cantilever setup. They cured a unidirectional carbon/epoxy at three different frequencies and labelled several curing parameters including matrix softening, gelation, vitrification, and solidification of the composite. On the other hand, Bilyeu et al. [20] combined DSC and DMA to construct the time temperature transformation diagram for an epoxy glass FRP. The three-point bending setup enabled them to find vitrification peak more clearly in the tan delta graph compared to the storage modulus.

Most in-situ cure monitoring research involves DEA as it is the most viable for this purpose. Hardis et al. used DSC as a baseline comparison to determine the kinetic parameters of epoxy resin while establishing a relationship between T_g and the

degree of cure from Raman spectroscopy and DEA under a single soaking temperature. [21] Kim and Lee [22] developed a new method to monitor the cure of glass fiber/polyester composite by embodying a dielectric sensor and a thermocouple to measure the dissipating factor and temperature of the part. Their method showed 70% matching compared to standard DSC. Two studies used a laboratory dielectric instrument to detect dielectric properties in conductive FRP composites samples during a resin transfer moulding cure cycle. [23,24] Through a parallel plate, they measured these parameters through the thickness to evaluate the cure kinetics: minimum viscosity, gelation, vitrification, and full cure. Moghaddam et al. [25] designed and embedded microscale interdigital capacitive sensors within glass FRP composites to monitor its curing. These small size sensors barely affect the mechanical performance of the final cured product while maintaining good DEA readings throughout the curing process due to their flexibility and high temperature resistance. Roberts and Davidson [26] used fibre optical sensors to measure electrical resistance measurements and dielectric impedance changes during curing. With the exception of the different DEA techniques, the mentioned methods are usually limited to in-lab setups hence are not feasible at an industrial production and processing level. [27] Industrial production require more feasible methods to monitor their processing on larger scales. This is why research involving ultrasonic methods was popularized in the past two decades to study the resin curing cycle.

1.3. Ultrasonic Cure Monitoring

In recent years, several polymer cure monitoring methods that can also be applied in industry emerged because of their feasibility. Ultrasonic measurements by

transmitting and receiving elastic waves are studied to read sensitive information about the material changes during the curing process. [28] Several studies involved bulk waves to characterize the resin curing on its own since these waves can be correlated directly to the evolving modulus and density of the material. [29,30] Longitudinal and shear moduli are directly proportional to the density and the square of longitudinal and shear wave velocities, respectively. Then, one can also calculate the Young's modulus and Poisson's ratio by simple linear equations relating the latter two properties to the longitudinal and shear moduli. [5,31] This is why these waves are of interest, since the reading of their velocities and attenuation gives knowledge about material stiffness and viscosity, respectively. The evolution of these mechanical properties during curing thus offers good estimation of the degree of cure. [32-34] Challis et al. [35] have shown that using compression and shear ultrasonic waves, the structure growth and cross-linking time of the resin can be determined. Aggelis and Paipetis [32] monitored epoxy resin using bulk ultrasonic waves and identified the gelation and vitrification points respectively through amplitude curves and wave velocity curves using ultrasonic transducers. They showed that velocity is linked directly to the stiffness of the resin. On the other hand, viscosity of the curing resin was found to be related to the attenuation of the propagating wave. [34] This simple correlation only applies in isotropic material like pure resins and metals, whereas in complex orthotropic material like the studied CFRP composites, more multifaceted waves are needed.

Pavlopoulou et al. [36] used an empirical mode decomposition to successfully monitor the cure level of a laminated composite after transmitting guided Lamb waves through the plate. Lionetto and Maffezzoli [37] used air-coupled transducers to determine the onsets of both gelation and vitrification where they found out that the

second onset happens because the kinetics of the reaction slow down, and the latter becomes diffusion controlled. Hudson and Yuan [38] created an automated process to monitor the carbon fiber composite using guided Lamb waves. Their analysis was based on only the amplitude graphs of mainly the antisymmetric A_0 mode of the propagating Lamb waves to determine all three cure parameters at several frequencies. Mizukami et al. [39,40] used a combination of signal processing for Lamb waves and a numerical micromechanics predictive model to respectively obtain attenuation and energy velocity then predict the CFRP complex modulus. They also compared their predictions with DMA measurements to verify the validity of the proposed method. Liu et al. [41] used a Semi-Analytical Finite Element (SAFE) method and manufactured an FBG and PZT smart sensing film embedded within the laminate, to predict the modulus first then monitor it, respectively. The film was later used to detect defects after curing.

1.4. Computational Cure Monitoring

Experimental practices are often expensive and produce generous amounts of waste. Numerical modeling was adopted long before the emergence of user-friendly commercial finite element softwares to reduce the experimental costs both in research and industry and optimize any studied concern before manufacturing. Computational studies of polymer cure monitoring can be divided into two main categories. The first is studying the chemical reactions that are triggered by heat, affecting the degree of cure, and roams around characterizing cycles for more optimized cure. [42,43] The second category of studies focuses on developing predictive viscoelastic models that use some experimental validation to forecast the changes in mechanical behavior during resin or polymer composites curing. [39,41]

Anandan et al. [44] used COMSOL Multiphysics to characterize a cure cycle for a CFRP composite. They obtained cure constants through DSC experiments and combined a chemical cure kinetics module with heat transfer module in the software to change the second soaking stage into a minor ramp with a different initial temperature. Garschke et al. [45] also studied the curing kinetics parameters by DSC and exported the results to a developed model that simulates the heat diffusion of the cure cycle. Their model was also used to predict viscosity. Behzad and Sain [46] also used COMSOL to simulate the curing process of a natural fiber composite and predict the temperature profile by validating experimentally. Then, they used the same model for predicting the cure of a more complex three-dimensional automotive mirror casing part. Another study [47] implemented the same kinetics module in COMSOL with infrared heating. Shi and Dong [48] based their numerical study cure monitoring on resin transfer moulding (RTM) and how curing converges from the edges of the plate to the center.

On the other hand, Dai et al. [49] used the same two modules in COMSOL with an added mechanics module which enables the use of viscoelasticity. By doing so, they predicted the residual stresses for a composite plate during curing and compared the results to a modified viscoelastic CHILE model. Zheng and Zhang [50] decompose the use of viscoelasticity within COMSOL by manually adding a structural relaxation study to the available Williams-Landel Ferry (WLF) stress relaxation shift function. Patham [51] also compared his cure-time-temperature superposition viscoelastic model in the same software to a regular elastic model to see the differences in stress residuals on constrained resin during curing. Yoo et al. [52] was one of the rare studies that implemented experimental DMA storage modulus results into a finite element method

(FEM) software to compare the cure parameters onsets numerically and experimentally. They implemented the storage modulus curves of DMA curing into ABAQUS and measured the strains using dielectrometry sensors. They identified the liquid, rubbery, and solid phases along with gelation and vitrification points in both numerical and experimental studies. Then, they used their validated computational model to simulate the curing of a wheel rim made of the same CFRP composites. Reportedly, no studies were found to apply this principle of importing modulus changes into an FEM software to simulate the curing of composites via guided Lamb waves. Similar to the latter study, this work does not take into consideration the curing kinetics nor the viscoelastic response of the cured material since that would add much more physics modules resulting in too many degrees of freedom and extensive simulation time. Also, both the chemical cure kinetics and the viscoelastic modules require DSC and stress relaxation experiments, respectively, to find certain parameters and constants, which would make this study unrealistically broad.

1.5. Length of the Curing Cycle

To achieve serious cost savings and make advantage of the curing process of the composite laminate, it is essential to reduce the manufacturing time. [53] Hence, cutting the time suggested by the manufacturer of the curing cycle is crucial as it can also improve properties of the finished product, especially in unoptimized out-of-autoclave processes. [54] Numerically, Pantelelis et al. [55] developed a computational method to optimize and design the cure cycle of composites. The method proved viability for several optimality criteria and the efficiency was demonstrated. Experimental cure cycle optimization techniques include the work by Dong et al. [56] on developing a rapidly

cured out-of-autoclave resin then implementing it in a prepreg to minimize the curing cycle time with most optimized properties of the cured part. Costa et al. [57] on the other hand, used DMA, DSC, and rheology to prove that slowing the heating rate of a certain composite from 5 and 10°C/min to 2.5°C/min lowers the gelation temperature and slows down the rapid cure kinetics to better improve the cycle. Other studies focused on optimizing the volume fraction of the fibers on one hand and getting rid of the voids and porosity on the other. [58,59] Hamdan et al. [60] focused on optimizing the manufacturing process as a whole and not just the curing time hence finding optimum pressure and temperature using numerical DOE (design of experiment) method. One major focus in this work is to study the feasibility of the proposed technology when cutting down the curing time and analyze the properties of the composite when shortening the curing time.

1.6. Background for Thin Film Material Selection

One of the main aims of this work is the investigation of the proper material needed to design and fabricate a thin reusable sensing system. A reusable flexible sensing film promotes recycling and induces less wasted material while being faster for monitoring purposes as the pace becomes faster in the setup, prior to the monitoring process. This flexible film sticks temporarily to the CFRP prepreg during curing and is reusable later on, thus also reducing consumables waste and expediting the setup in subsequent experiments. The material selection for this sensing film would be based on chemical, electrical, and mechanical properties. Among several material candidates that possess the required properties such as high melting temperature, elevated temperature withstanding, matching acoustic impedance with epoxy resins which enables it to

capture the wave without much interference [61], and chemical inertness, Polytetrafluoroethylene (PTFE) commonly known as Teflon is a suitable candidate. Teflon has been used as artificial delamination in-between layers for composite testing [62-64] which allows debonding to happen easily by separating the inserted film from the composite. Moreover, PTFE is used as fiber filler for the thermoplastic polymer Polyetheretherketone (PEEK) to fabricate a composite with lower friction coefficient and higher resistance to wear than the virgin PEEK material. [65] Another test showed that the lowest shear stress, lowest breakdown time, and highest contact angle were observed in the PTFE barrier-epoxy resin combination in comparison to other material. [66] In addition, PTFE is known for its liquid repellency as it shows hydro- and oleophobic properties especially in the kitchenware industry. [67] Such properties make it an ideal candidate to be used as the required thin film. Thus, two thin PTFE layers sandwiching piezo-electric transducers (PZTs) would make a fine sensing network that adheres to the composite temporarily during curing while being reusable afterwards.

1.7. Lamb Waves Fundamentals

In 1917, Horace Lamb [68] published his deconstruction of elastic waves present in infinitely-long thin solid media that propagate by reflecting off the upper and lower boundaries of a plate thus expanding into two infinite sets of wave modes: symmetrical (S) in-plane, and anti-symmetrical (A) out-of-plane modes. Named after him, Lamb waves have complex properties that depend on the relationship between plate thickness and the wavelength. [69] Although both symmetric and anti-symmetric Lamb wave modes are constituted of mixed longitudinal and shear vibrations, the former can be simplified by a longitudinal wave motion whereas the latter can be

approximated as a bending wave. The two sets of wave modes are made up of a superposition of longitudinal and shear vibrations, and their propagation characteristics vary with the excitation type, angle, and the structure shape itself. [70] Figure 1.1 shows the particle displacement of symmetric and anti-symmetric modes. The following simplified equations describe the motion of Lamb waves inside a thin linear elastic and isotropic plate that is unbound in the x and y directions:

$$\frac{\omega^4}{C_T^4} = 4k^2 q^2 \left[1 - \frac{p \tan\left(\frac{ph}{2} + \gamma\right)}{q \tan\left(\frac{qh}{2} + \gamma\right)} \right]; \quad (1)$$

$$p^2 = \frac{\omega^2}{C_L^2} - k^2; \quad (2)$$

$$q^2 = \frac{\omega^2}{C_T^2} - k^2; \quad (3)$$

where γ represents the S and A wave modes for values of 0 and $\pi/2$ respectively, h is the plate's finite thickness, k is the wave number, ω is the angular frequency, C_L and C_T are respectively the longitudinal and transverse velocities of the bulk material.

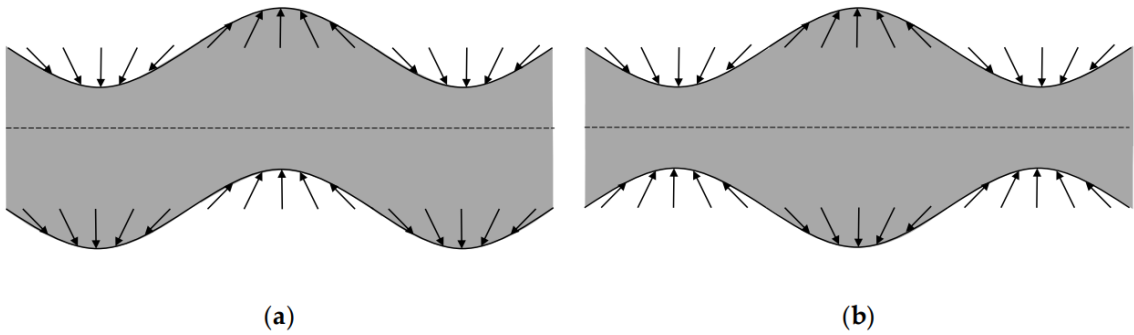


Figure 1.1: Displacement of particles in an (a) antisymmetric and (b) symmetric Lamb wave modes. The median dotted line of the plate is shown. [71]

Since Lamb waves are theoretically present in infinite plates, guided Lamb waves is a more practical term to identify Lamb-like waves that are excited in finite thin

plates and cylindrical structures. [72] These waves have been used in various nondestructive testing (NDT) applications to evaluate and monitor the structural properties and integrity of different metallic and non-metallic structures. Being reliably capable of propagating, highly sensitive to damage, and easily generated and collected, Lamb waves offer high-precision damage detection, making it a competitive substitute to traditional NDT tools. [73] Harb and Yuan [74-76] assembled a fully non-contact system for identification of delamination in composite laminates using the fundamental antisymmetric (A_0) Lamb wave mode. The same research group used Lamb waves for imaging hardly visible damages in metallic and composite plates. [77] Mustapha et al. [78] proposed a practical approach for the detection of debonding in sandwich composite structures using a time-reversal technique based on A_0 Lamb wave mode at low frequency. Okabe et al. [79] offered a new delamination detection method based on the change in the dispersion characteristic from the information obtained about the Lamb wave mode conversion using Macro-Fiber Composite (MFC) actuators and Fiber Bragg Grating (FBG) sensors on a quasi-isotropic CFRP laminate. Mehrabi and Soorgee [80] employed Lamb waves to detect the curing of two adhesives. They identified the process in three stages: uncured, semi-cured, and fully cured resin while having the amplitude of the wave dropping as the adhesive cures. More recently, guided Lamb waves have been used for more variant research such as: characterizing the friction stir welded joints of dissimilar materials using the frequency-wavenumber filtering technique [81,82], optimizing sensor placement on metallic and composite structures for maximum damage detection coverage area having minimum number of PZTs glued to the surface [83], and determining the adhesion quality within three-layer

structures (aluminum/adhesive/composite) which serves as a basis for future large scale manufacturing process quality control [84].

Lamb waves are dispersive, which means that the velocity of each mode is not constant, but dependant on the excitation frequency. [85] For a thin woven CFRP plate of 1 mm thickness, a frequency range between 50 kHz and 300 kHz simplifies the propagating sets of Lamb waves to only the first symmetric and asymmetric modes: S_0 and A_0 , which makes signal processing and mode identification easier. Usually, S_0 is faster than A_0 at low ultrasonic frequencies. As the frequency increases, S_0 velocity decreases while that of A_0 increases, as they both converge towards each other in values transforming into a Rayleigh-Lamb wave. [86] Also, these modes propagate with different displacement amplitudes, making each frequency denoting an amplitude dominant mode over the other regardless of their speeds. All these variants make Lamb waves complex to work with but also easy to distinguish once understood and analyzed.

Figure 1.2 shows the experimental tuning and dispersion curves of a fully cured unidirectional CFRP laminate that consists of 3 layers of out-of-autoclave XPREG XC130 unidirectional prepreg $[0]_3$ and that has a thickness of 1 mm. The frequency range tested is between 10 and 400 kHz where as seen in Figure 1.2 (b), the speed of S_0 fluctuates between 5500 and 6500 m/s whereas the A_0 velocity ascends from 600 to almost 1300 m/s before its amplitude diminishes and the mode disappears at 150 kHz. In Figure 1.2 (a), A_0 is clearly dominant up to a frequency of 100 kHz where S_0 becomes prevalent after that. The symmetric mode has an amplitude peak at 330 kHz whereas the voltage peak for A_0 occurs at 70 kHz. The latter frequency is chosen to excite the CFRP laminate during the cure monitoring experiment due to many factors. First, A_0 is at its highest respective strain compared to S_0 , so not only is A_0 dominant at

this frequency, but the highest difference between the two voltage curves occurs at this point. The decision to work with A_0 also derives from the fact that the anti-symmetric mode propagates in an out-of-plane manner along the moving path, thus it is more suitable for the propagation through the thin PTFE film and into the CFRP composite and the aluminum tooling plate. Whereas the S_0 mode, propagating in-plane, severely attenuates when moving from one material boundary to another.

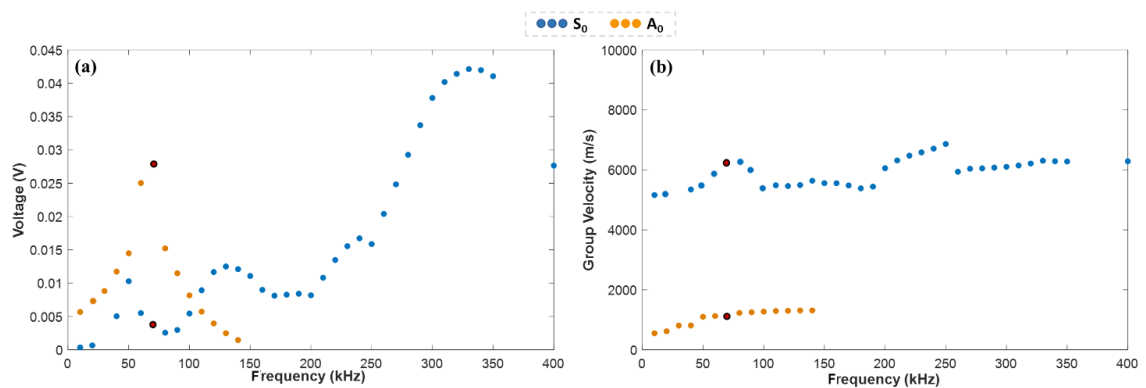


Figure 1.2: (a) Tuning curves showing voltage amplitude of each mode vs frequency, and (b) dispersion curves showing group velocity of each mode vs frequency, both for the cured 1mm-thick unidirectional CFRP plate

1.8. Objectives and Outline

This work examines the use of ultrasonics to monitor the curing cycle of CFRPs through certain wave parameters. To study the feasibility of this monitoring process, Chapter 2 introduces the experimental setup needed in selecting the thin film material by making sure it debonds from the carbon fiber after curing and transmits readable Lamb wave signals throughout the material. Then, this work reports on the online monitoring of unidirectional and woven laminates, the effect of the thin film on the generated Lamb wave modes and provide several trend line analysis discussing cure parameters using the proposed system. After monitoring the curing cycle, the feasibility

of this reusable sensing film is verified by scrutinizing a post-cure cycle for the exact same cured plates.

Chapter 3 starts by briefly explaining the cure monitoring process via analysis of the A_0 mode through velocity and amplitude curves. Then, the cycle time is shortened in its longest soak period and cut by one hour. The same ultrasonic monitoring is done again on the new cycle and the same cure parameters are defined. Tensile testing is then done to prove that this time cutting does not affect the mechanical properties of the finished product. After that, dynamic mechanical analysis is used in its single cantilever setup to monitor the two cycles while curing, and to test for any T_g or static fatigue differences between them after curing. The final verdict is concluded from the results of this traditional resounding method.

Chapter 4 emphasizes on the DMA curing of the same woven composite and more results are shown through storage modulus (E') curves at different frequencies, and the averaged E' curves for both the baseline and the shortened curing cycles are extracted and implemented in COMSOL Multiphysics FEM software. The different modules used to make up the piezoelectricity effect in the software are explained and the numerical model is presented with its detailed components. After that, the results are shown in terms of signal comparison for both cycles to their experimental counterparts. Also, the numerical velocity and amplitude curves are extracted for both cycles. The wavefields are compared in both x and z velocity directions for different curing points. Finally, the viability of this computational method is discussed by comparing numerical and experimental results and showing the advantages and limitations of this study as a new cure parameter is suggested by analyzing the computational data.

Chapter 5 introduces the cure monitoring of epoxy prepreg adhesive films used for structural and joint bonding of two fully cured CFRP plates. The same methods are used to analyse the data extracted from the ultrasound monitoring of this adhesive. Then, post-cure monitoring on the CFRP plates is performed to remove the effect of heat and determine accurate cure parameters. DMA curing is also done on the epoxy film and the results are implemented in the numerical model developed earlier. Sole A_0 mode is actuated numerically to enhance the scrutiny of mode conversion at the overlap. The numerical results show heavy dependence on the adhesive DMA curing inputs, but still highlight the desired cure points. Finally, cocuring of both adhesive film and non-cured CFRP prepreg laminates is also introduced at the end of this chapter where the amplitude curves show more sensitivity towards the added adhesive film cure parameters.

In the end, Chapter 6 summarizes the work done in each previous chapter and focuses on the new overall knowledge gathered throughout the thesis. It also opens up multiple doors for future work and research plans derived from several conclusions in each chapter.

CHAPTER 2

MATERIAL SELECTION AND IN-PROCESS MONITORING

This chapter shows the development of a sensing technology in the form of a reusable in-situ cure monitoring and assessment system that can predict and monitor the degree of cure. Cure debonding and signal transmission tests are performed on various thin-film PTFE-based material such that the one to transmit the highest signal through an aluminum plate is chosen. Then, this film is used to sandwich piezoelectric actuators and sensors to monitor out-of-autoclave carbon fiber composite plates using ultrasonic Lamb waves by temporarily adhering to the manufactured part creating an effective electromechanical coupling between the sensing film and the laminate. Through analysis of speed and amplitude of the fundamental antisymmetric A_0 mode at a low ultrasonic frequency and over the cure cycle time, cure parameters such as gelation and vitrification are determined for two types of CFRP. Post-cure monitoring on the already monitored and cured plates, and cure cycle shortening, are also assessed successfully to test the feasibility of this sensing system.

2.1. Material Selection

2.1.1. Bonding Test

Samples of five different materials shown in Table 2.1, consisting of three PTFE films, one modified PTFE (TFM), and one Fluorinated ethylene propylene (FEP), are investigated for bonding strength and ultrasonic signal transmission. These materials have acoustic impedances close to that of epoxy with low electrical dissipation factor and possess chemical inertness. Long strips (15 x 80 mm²) were cut from each material

and placed directly on the top of an uncured carbon fiber laminate, as shown in Figure 2.1 (a), which was then cured under vacuum following the manufacturer’s curing cycle. After curing, the strips were manually peeled off the sample to study the bonding of the material with the laminate post curing. The peeled samples as seen in Figure 2.1 (b) show that TFM and FEP partially bonded to the plate while the three PTFE samples peeled off easily leaving a smooth surface finish on the plate.

Table 2.1: Thin film material used and peeling test results.

Specimen	Material	Film Thickness (mm)	Peel Test
TF-1	Skived PTFE	0.5	No Bond
TF-2	Glass Cloth PTFE	0.25	No Bond
TF-3	FEP	0.13	Bonded
TF-4	Cast PTFE	0.25	No Bond
TF-5	TFM	0.08	Bonded

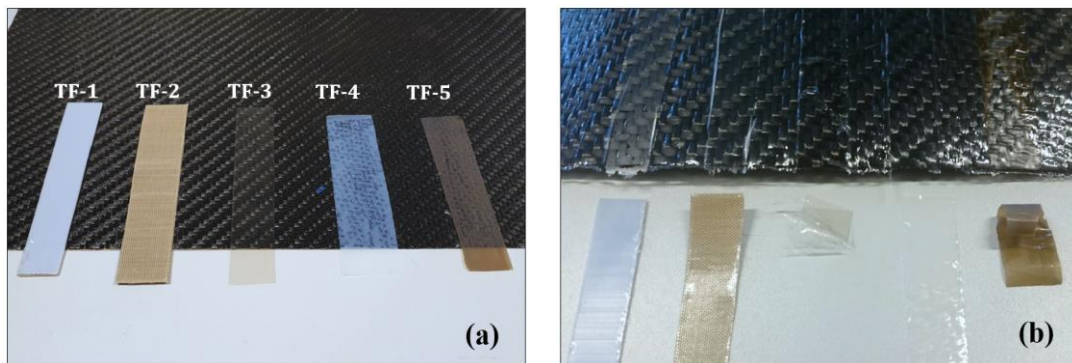


Figure 2.1: Thin film specimens (a) before and (b) after peel test.

2.1.2. Signal Transmission

The non-bonded materials from the previous test were further investigated for their wave propagation effectiveness when sandwiching an ultrasonic transducer. The emphasis of this experiment is on the amplitude of the excited and received signals through the different PTFE materials. A 300 x 300 x 3 mm³ Aluminum (Al-1050) plate

was used as the base structure with five disc-shaped piezoceramic transducers (PZTs), 1 mm thick x 10 mm in diameter, glued directly on the plate and three other discs were placed inside 30 x 15 mm² sandwich of each PTFE material as illustrated in Figure 2.2. The PTFE sandwiched PZTs were not glued to the Aluminum plate but were assumed to have a near perfect adhesion when the whole sample is under vacuum.

Five-peak sinusoidal Hanning-windowed signal, generated by a Keysight 33500B signal generator and amplified by an EPA-104 Piezo System Inc amplifier, was used to excite PZTs. On the other end, sensing PZTs were recording any measured signal via a Keysight InfiniiVision DSO-X 3024A oscilloscope. The actuators and the sensors are 150 mm apart which is enough distance for the two Lamb wave modes, symmetric S_0 and antisymmetric A_0 , to be separated discretely for the selected frequency of 250 kHz. Two main studies were conducted such that the PZTs sandwiched with the PTFE materials were either actuators or sensors. This is because excitation and reception of the signal with the addition of the PTFE layer on only one side is not reversible. The reflections within the PTFE boundaries would differ hence resulting in a difference in the sensed signal. Then, each of the two studies had three different cases depending on the propagation direction of the wave or actuator-sensor combination. For instance, S4B4, S4B3, S4B2 would be respectively case 1, case 2 and case 3 for the first study when the Skived PTFE sandwiched (S) PZT is an actuator and the bare (B) PZTs are sensors; whereas B4S4, B3S4, and B2S4 would be the same cases respectively for the second study when the bare PZTs are actuators and Skived PTFE sandwiched PZT acts as a sensor. In both studies the obtained data are compared to the baseline data measured from S1B1, S1B2, S1B3 or B1S1, B2S1, B3S1.

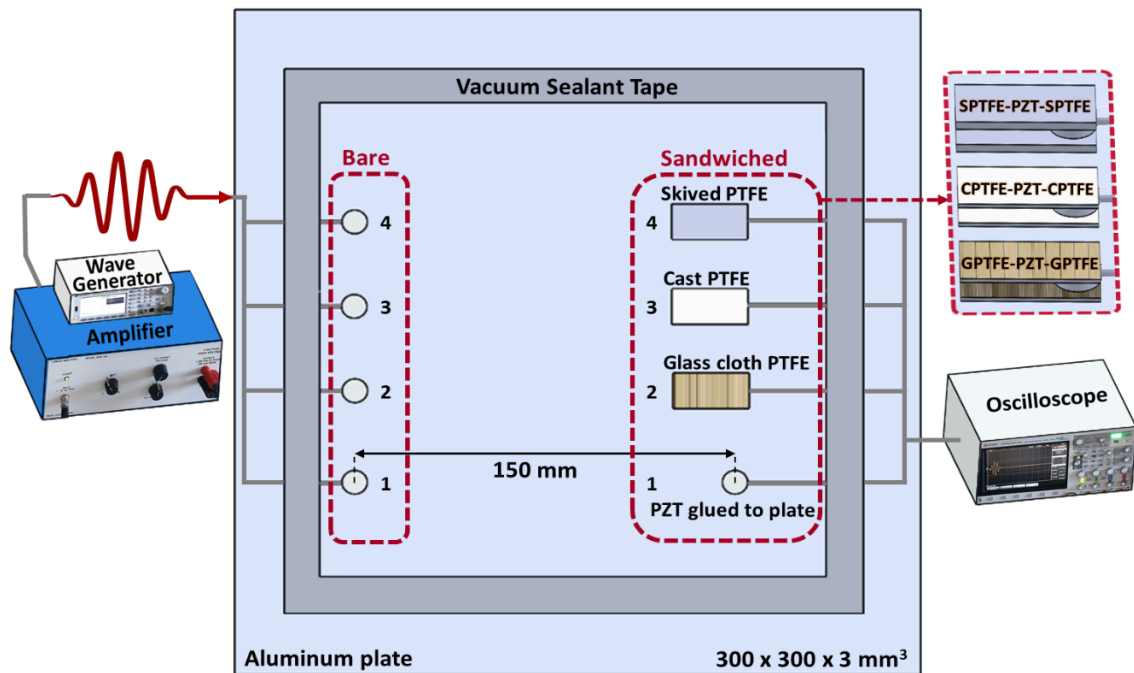


Figure 2.2: Experimental setup for signal intensity measurement using sandwiched PZTs (not drawn to scale).

For the used frequency of 250 kHz, the S_0 mode is dominant over A_0 in aluminium according to the tuning curves from both theory and experiments. [87] The amplitude of the highest peak of the first received S_0 packet in the measured signal is compared for all PTFE sandwiched PZTs to check for the highest transmission among them. The results in Figure 2.3 for all six cases show that Skived PTFE has the best signal transmission compared to Cast and Glass cloth PTFE. The out-of-planar nature of the A_0 mode should make it spread through the added PTFE material in a higher relative amplitude than S_0 , which vibrates in the plane of the propagation direction, unlike A_0 which pulsates perpendicularly, i.e., in the z -direction, to the wave moving direction. This is why the A_0 mode needs to be analyzed through these material too. The plate used is considerably small and the edge reflections coming from S_0 may coincide with

the first received A_0 packet. Hence, another experiment with a bigger plate is conducted.

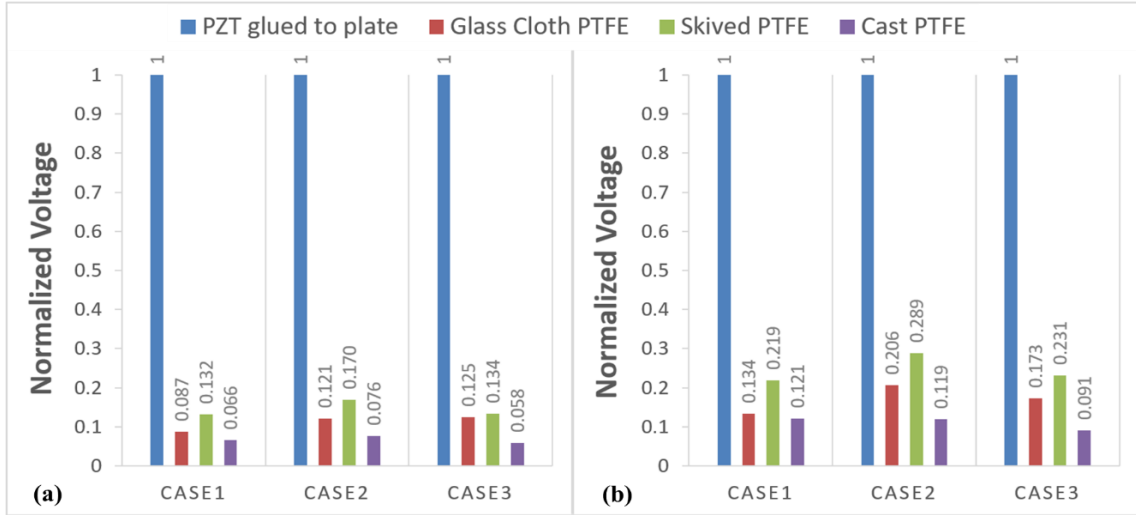


Figure 2.3: Normalized amplitude for S_0 mode at 250 kHz for the different materials in all three cases where Sandwiched PZTs act as (a) Actuators and (b) Sensors.

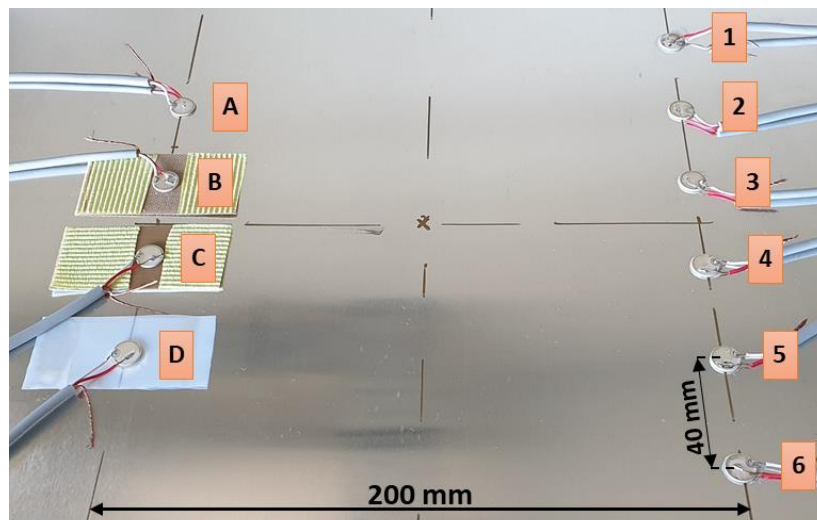


Figure 2.4: Second signal transmission setup at the center of a $1000 \times 1000 \text{ mm}^2$ Al-1050 plate. In this figure: B is Glass cloth PTFE, C is Skived PTFE and D is Cast PTFE.

To better analyze the signal performance along the added PTFE, the signal generation was investigated over other frequencies where A_0 or S_0 are dominant. In Al-1050, according to the same theoretical and experimental tuning curves, the A_0 mode is dominant at 100 kHz while S_0 is the major mode at 200 kHz. It is worth mentioning that these experiments are in line with theory and with Giurgiutiu's work on this [88]. Figure 2.4 shows the setup of the second wave generation experiment which was carried out in the center of a large $1000 \times 1000 \times 3 \text{ mm}^3$ plate to delay unwanted boundary edge reflections. One layer of each PTFE material with a cross-sectional area of $30 \times 60 \text{ mm}^2$ is placed underneath transducers B, C, and D. Vacuum was always used to enhance contact. Two additional PZTs, 1 and 6, were also glued on the right side making one more additional path for each material, thus a fourth case. The materials were only used as actuators for four cases and tested with the two frequencies. Figure 2.5 shows the horizontal path case of signal generation (A2, B3, C4, D5 from Figure 2.4) where it is clear that the two modes are separated, and no reflections overlap with the first received A_0 packet. It is noticeable how the weaker S_0 mode at 100 kHz is barely recorded by the PZTs layered over the PTFE materials. In fact, although S_0 is dominant at 200 kHz, its amplitude is still read lower than A_0 by these PZTs. Table 2.2 summarizes the results of all 16 studied cases where for each frequency, exist four cases for each mode. The table also demonstrates the 8 dominant mode cases: A_0 at 100 kHz and S_0 at 200 kHz.

Unlike the first signal transmission experiment, Skived PTFE does not have the highest amplitude in all cases. For the dominant A_0 mode at 100 kHz and the dominant S_0 mode at 200 kHz, Skived PTFE leads with all four cases and two cases (shared Glass cloth PTFE), respectively. For the weaker S_0 mode at 100 kHz and A_0 mode at 200 kHz, Cast and Glass cloth PTFE have the highest amplitudes, respectively. For the sum of all

cases, Skived PTFE transmits the highest amplitudes in 7 out of 16 cases while it leads in 6 out of 8 dominant mode cases. Knowing that this material has a 0.5 mm thickness while the Cast and Glass cloth PTFE were both 0.25 mm thick, Skived PTFE was clearly chosen to be the sole candidate for the cure monitoring application.

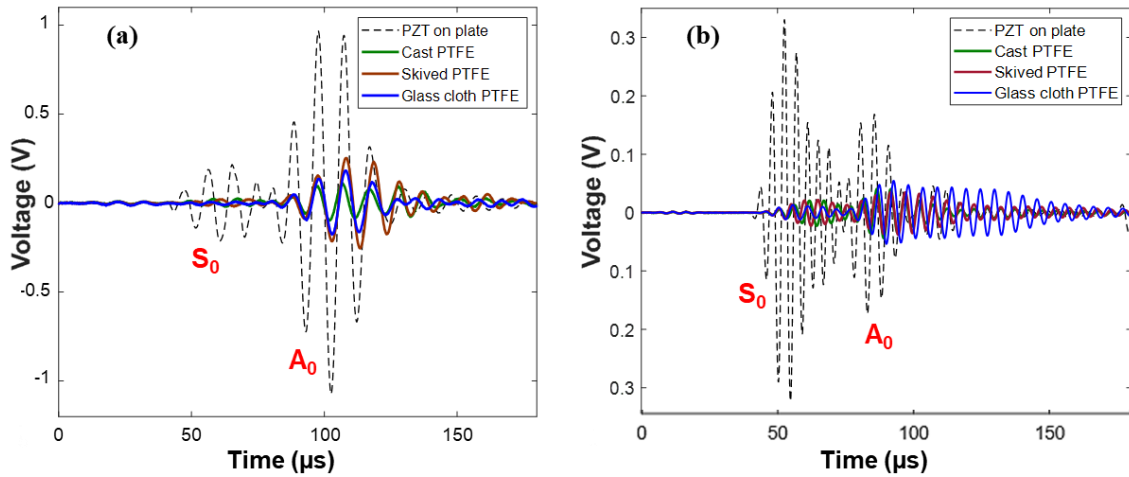


Figure 2.5: Sensed signals by the bare PZTs when actuated from the sandwiched ones with excitation frequencies of (a) 100 kHz and (b) 200 kHz.

Table 2.2: Number of cases recording highest amplitude for S_0 and A_0 Lamb wave mode at 100 and 200 kHz for different thin film materials.

	100 kHz		200 kHz		Total	%	Dominant Modes	%
	S_0	A_0	S_0	A_0				
Glass cloth PTFE	0	0	2	2	4	25	2	25
Skived PTFE	0	4	2	1	7	43.75	6	75
Cast PTFE	4	0	0	1	5	31.25	0	0
Number of Cases	4	4	4	4	16	100	8	100

2.2. Cure Cycle Monitoring

2.2.1. Experimental Setup

Two kinds of composite laminates were considered in this study for the cure monitoring experiments. The first is an autoclavable XPREG XC130 unidirectional Pre-impregnated Carbon Fiber-Reinforced Polymer (CFRP) and the second is an out-of-

autoclave XPREG XC110 woven prepreg CFRP. In this work, both composites were cured in a precision composites curing oven (OV301 *easycomposites*TM) under vacuum and heat. In the absence of an autoclave, the manufacturer suggested using the same out-of-autoclave cycle for both types. While the parts were under vacuum, the heating cycle started at room temperature and heated slowly at a rate 1°C/min until it reached 70°C and left soaking at that temperature for 4 hours. The oven was then heated to 120°C at a 2°C/min heating rate and soaked for 1 hour and then cooled down to room temperature naturally. Figure 2.6 shows this curing cycle including both heat and pressure.

Two separate cure monitoring experiments were done during this study. The first cure monitoring experiment was done on two unidirectional [0]₃ CFRP laminates while the second was investigated on two woven [0/90/0] CFRP laminates. All laminates were 220 x 350 x 1 mm³ in dimensions. Figure 2.7 shows the setup of this experiment where a 700 x 400 x 6 mm³ aluminum plate is used as the tooling plate. The plate is partitioned into three equal sections. Section **A** has an actuating and sensing PZT directly glued on the aluminum which will monitor any change involving the PZTs and Al plate during the curing cycle for any temperature effect. Section **B** holds one CFRP laminate with PZT sensor and actuator directly placed on its top surface. Section **C** holds another CFRP laminate with PZT sensor and actuator sandwiched between two Skived PTFE films over the composite. The Skived PTFE films were 0.5 mm thick each, of the same size as the CFRP plate and with adhesive silicone layers on one side which were cut and joint together having two PZTs in between. All PZTs used were disc shaped PZT-5J material type with 0.5 mm thickness, 7 mm diameter, and had 320°C Curie temperature making them effective for temperatures up to 160°C as

recommended by the manufacturer. The PZT wires are soldered below Curie temperature using 60-40% Sn-Pb solder that has a 190°C melting temperature. Silicone release agent was sprayed on the Al plate under the two CFRP plates to prevent any bonding. The plate was then placed in a vacuum bag with the wires well sealed to prevent air leak during vacuum and then placed in an oven following the manufacturer's recommended curing cycle.

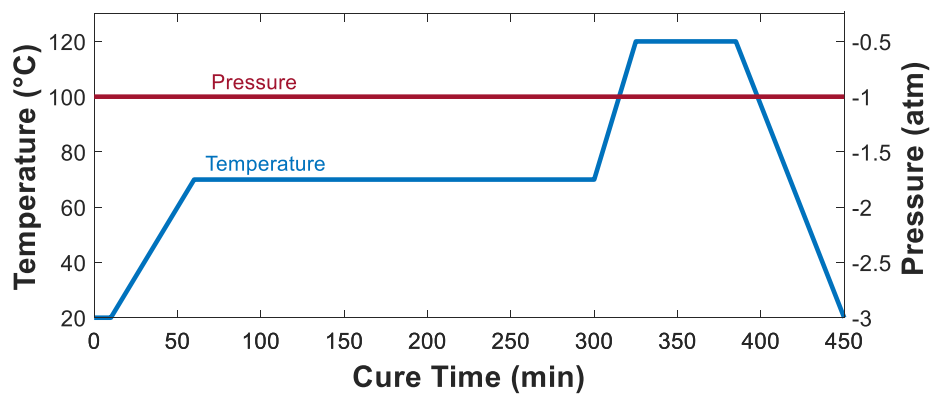


Figure 2.6: Cure cycle of the out-of-autoclave prepreg as proposed by the manufacturer.

The actuation and sensing system used in the earlier experiment was also implemented in this experiment. The amplified signal to the actuator was 160 Vpp (peak-to-peak voltage) at a central frequency of 70 kHz. This frequency was chosen after some testing as it provides highest A_0 amplitude and nearly eliminates S_0 in the unidirectional CFRP. This does not apply to the woven CFRP as both modes are noticeably clear in this prepreg, but we kept the same frequency for the purpose of comparison. Data was being measured by the oscilloscope every 10 minutes from all three sensors in sections A, B, and C for each actuator.

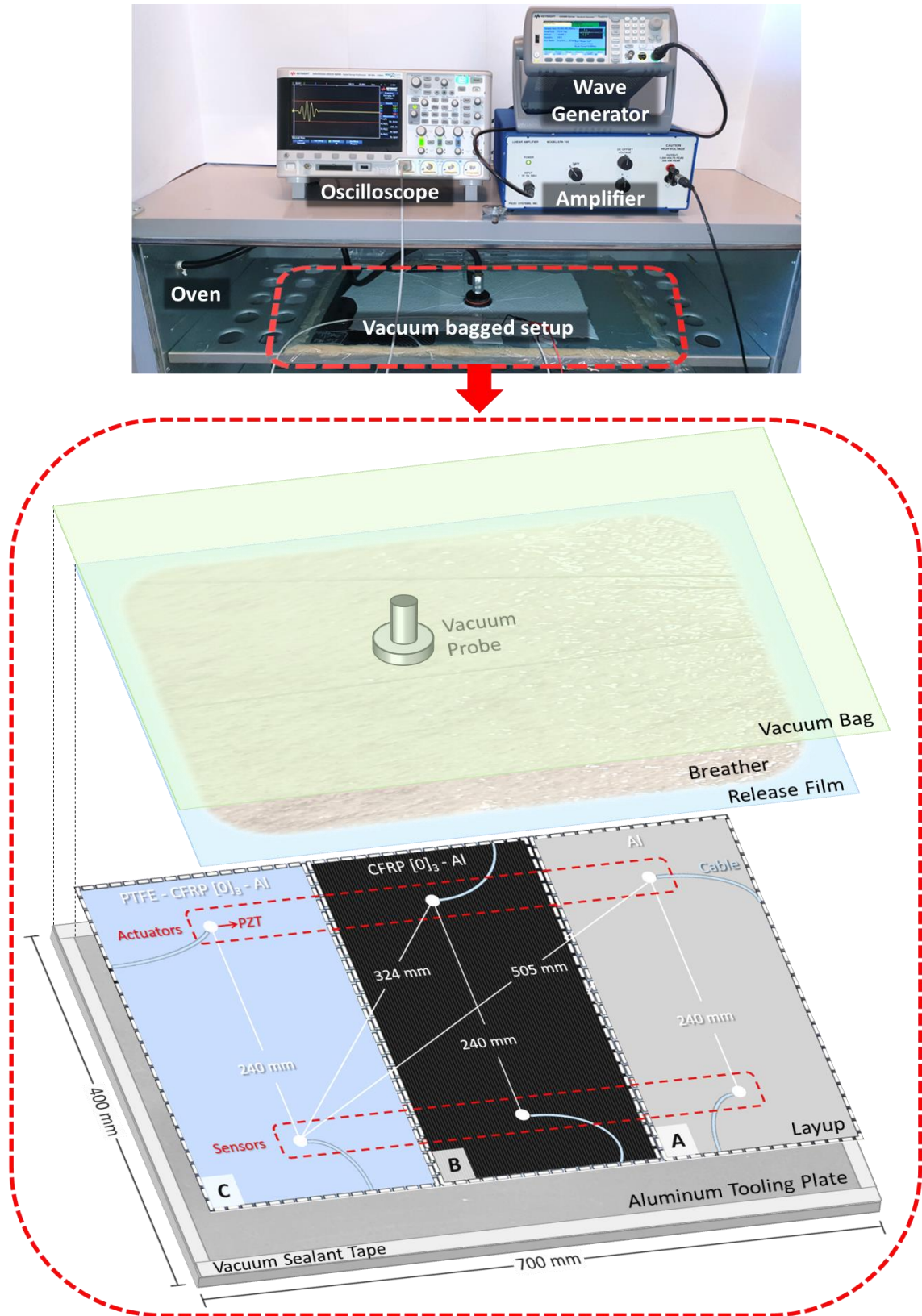


Figure 2.7: First cure monitoring experiment setup showing different paths that are tracked for each actuator-sensor.

2.2.2. Results

The data collected is analyzed through two parameters: the voltage of the received signal and the group velocities of the generated modes. The group velocity is simply the distance between the transmitting and receiving transducers, covered by the propagating signal, divided by the time-of-flight. When the Lamb wave propagates through any material, depending on its properties and the excitation frequency, the excited signal inherits dispersion. This means that the number of peaks in a packet can increase as it travels, and the amplitude of the highest peak decreases as it shifts from the third peak in the input signal to other peaks at the centroid of the sensed signal, which causes slower moving packets as the time between the third peak of the actuator and the centroid of a dispersive wave would increase. This phenomenon is mentioned because while dealing with this data, some signal paths caused the waves to be slightly dispersive causing the analysis to take on two forms: through the signal itself and its envelope. If dispersive, the envelope's highest point would be the centroid, giving the actual group velocity, and the third peak, which is now ahead of the centroid, would give a velocity in between the phase velocity and the group velocity. For simplicity, both are called group velocities and the better trend of the two is chosen. Figure 2.8 shows an example of a measured signal from the PTFE sensing film over the unidirectional composite.

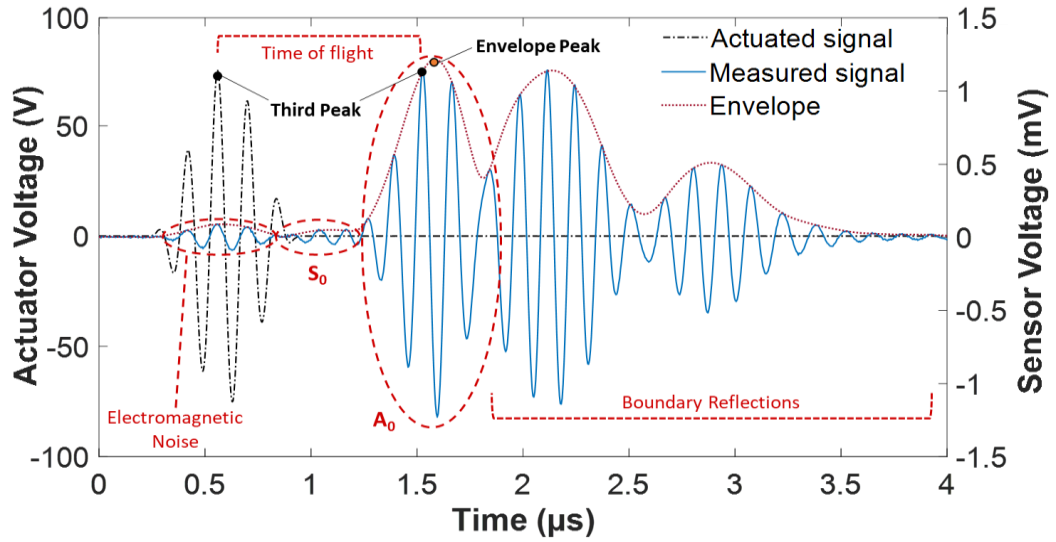


Figure 2.8: Measured signal from the PTFE sandwiched actuator-sensor film at 10 mins into the curing cycle.

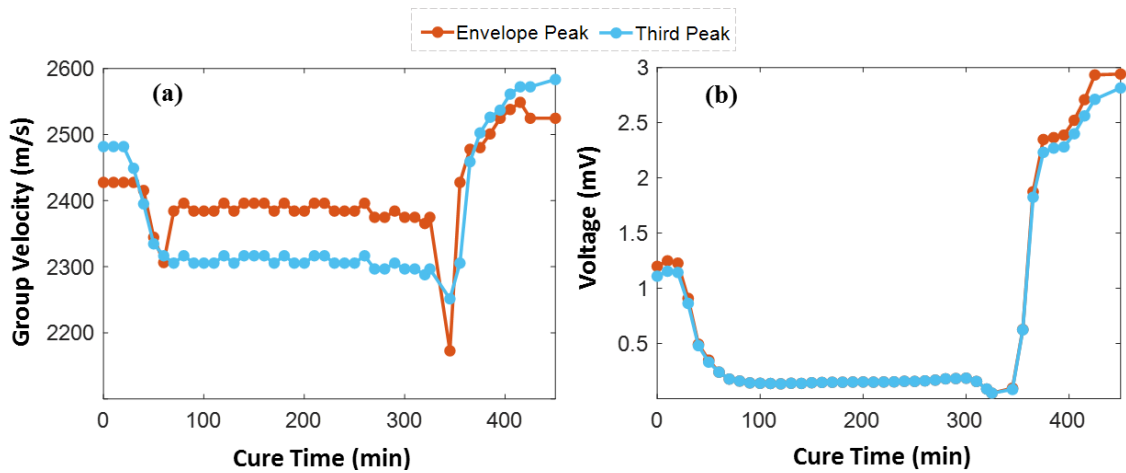


Figure 2.9: (a) Group velocity and (b) Voltage of A_0 mode generated and received by the skived PTFE sandwiched PZTs over the $[0]_3$ unidirectional laminate.

For the same sensing film and CFRP, Figure 2.9 shows data points of group velocity and voltage as function of curing time. It also shows the difference between using the third peak and the envelope to calculate these parameters. While the voltage curves show the same trend with minor differences in the values at the beginning and end of the cycle, the velocity curves are similar except for the obvious shift in the

middle 4-hour soak section as the envelope goes faster by almost 100 m/s during this liquid phase. For most of the paths analyzed, the group velocity curves are better evaluated when using the third peak instead of the moving envelope peak. Thus, in this work, velocity and voltage curves are measured according to the signal's third peak. Future plots will show only the trends of the curves without inclusion of the data points for better visuals.

2.2.2.1. Trendline Analysis and Comparison

Figure 2.10 shows the group velocity and signal amplitude curves for the A_0 Lamb wave mode for seven paths from the first cure monitoring experiment in Figure 2.7. Starting with the bare aluminum path plotted in dark red ($AL_{act} - AL_{sen}$) in Figures 2.10 (a) and (b), its velocity and voltage slightly decrease with the increase in temperature. This could be explained by the almost linear decrease of the elastic modulus of aluminum during the curing cycle due to the increase in temperature [89] which the velocity and attenuation of Lamb wave depend on. With such insignificant change in velocity and voltage compared to the other curves, mainly those of the $PTFE_{act} - PTFE_{sen}$ and $UNI_{act} - UNI_{sen}$ paths, it is feasible to assume that the propagation of Lamb wave in aluminum during the curing cycle stays intact. Notice that at 450 min, the ($AL_{act} - AL_{sen}$) path velocity and voltage curves still haven't gone back to their initial values. This is because the plate temperature after only one hour of natural cooling is still in the 50-60°C range and haven't reached room temperature yet. Once it did after two to three hours, both the velocity and voltage went back to their initial state.

On the other hand, the setup is under vacuum during the cure cycle which would create a near perfect bond between the aluminium and the composite laminates. Thus, the effect of this bond creating a CFRP-Aluminium composite in section B and PTFE-CFRP-Aluminum composite in section A on the generated Lamb wave needs further investigation. The velocity and voltage curves for all other paths, as seen in Figure 2.10, drop at the beginning of the cure cycle due to the consolidation of the prepreg and then becoming a viscous fluid with a plateaued curve until it reached a drop when it starts the gelation process which then increases and stabilizes when it solidifies. It is noticed that the group velocities of all six paths passing through the composite plates are lower than the group velocity from the $AL_{act} - AL_{sen}$ due to the interference of the wave with the laminates which have lower A_0 group velocity than the aluminium plate. That velocity is even much lower for the propagating wave within the same laminate: $PTFE_{act} - PTFE_{sen}$ and $UNI_{act} - UNI_{sen}$. Thus, the aluminium base plate does influence the group velocity of the A_0 mode since the laminates are in contact with the tooling plate due to vacuum and the silicone release agent. But since the monitored parameters are stable throughout the cure cycle as proven, we could assume that the measured data is viable to monitor the cure of a laminate.

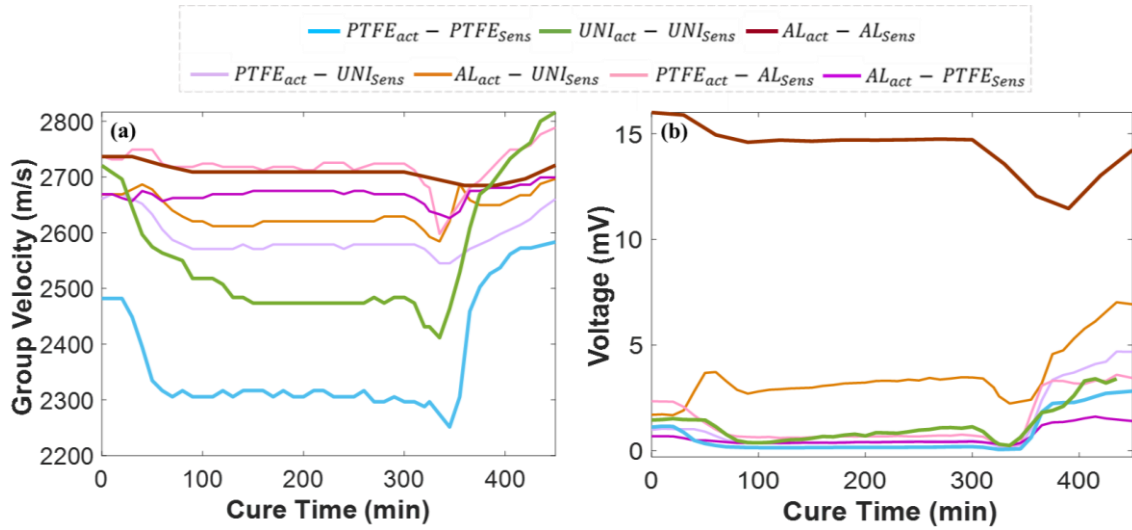


Figure 2.10: (a) Group velocity and (b) Voltage of A_0 mode generated and received along different paths in the first cure monitoring experiment.

Comparing directly the A_0 mode group velocity curves for unidirectional CFRP with and without the use of thin PTFE film in Figures 2.11 (a) and (b), one can see that the velocity of A_0 shifts downwards when having PTFE due to the additional stacking in the PTFE-CFRP-Aluminum laminate under vacuum. However, the trends of the two velocity curves are very similar having a decrease in the velocity from 0 to 100 mins due to the initiation of resin consolidation inside the prepreg. The resin becomes a viscous fluid with a relatively constant velocity between 100 and 300 mins until it reaches a drop when it starts the gelation process at 310 mins. The minima after that indicates full gelation and then both curves increase until reaching an asymptotic value at the end of the cure. But before that, the trend of the incline changes halfway slowing the rate of cure and indicating an onset that Lionetto and Maffezzoli [37] claimed to be the vitrification point which demonstrates the start of the glassy solid state.

The voltage curves show the same trend as the velocity curves except for a clear increase in the amplitude for the plate without PTFE during the liquid phase until it

reaches a maximum around 300 mins before dropping off. This maximum is also present in the PTFE path when zooming in on the curve. This, according to Hudson and Yuan [38], represents the minimum viscosity of the resin before gelation, hence the latter starting after this point occurs. It is of interest to highlight the fact that this maximum occurs around the end of the first soak and the start of the second ramp in the cycle. Gelation is a process where the rubbery state is present in the prepreg after an irreversible transformation in the resin from liquid to gel due to the appearance of a cross-linked network and approaching infinite molecular weight [90]. It takes place between the previous maximum (“minimum viscosity”) and the time of the previously discussed vitrification onset. The minimum point between the two indicates full gelation of the prepreg. Both $PTFE_{act} - PTFE_{sen}$ and $UNI_{act} - UNI_{sen}$ paths have the same times for minimum viscosity at 300 min, gelation at 335 min and vitrification point at 375 min. A few minutes difference is noticed when these points were detected on the velocity and voltage curves. Hence, the first two parameters are always taken from the voltage curves while vitrification is acquired from the velocity curves as it is noticed in previous work. The velocity and voltage curves of S_0 mode plotted in Figures 2.11 (c) and (d) show the absence of S_0 during the liquid stage for the $PTFE_{act} - PTFE_{sen}$ and $UNI_{act} - UNI_{sen}$ paths. The advantage of the $PTFE_{act} - PTFE_{sen}$ path is clearly visible as S_0 appears at the gelation point unlike the $UNI_{act} - UNI_{sen}$ path for which it appears at or just before vitrification. This indicates that monitoring the cure with frequencies where A_0 is dominant is a more reliable method because its out-of-planar nature allows it to pass through the several layers included in this bagging and monitoring process at all states of the prepreg as proven.

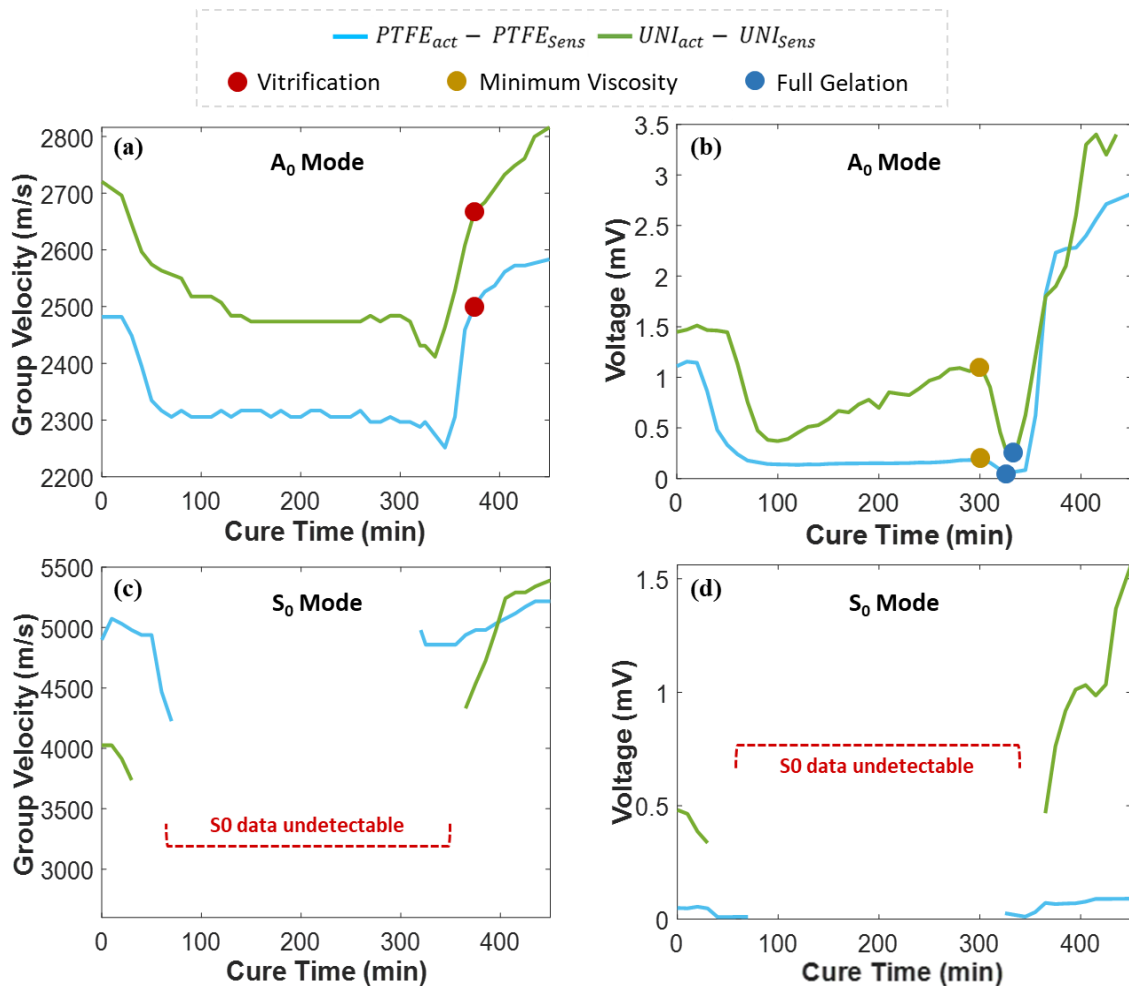


Figure 2.11: Group velocity and Voltage of A₀ and S₀ mode generated and received over the [0]₃ unidirectional laminate.

To further investigate the onset of vitrification of the unidirectional composite which occurred at 375 min, two raw signals from the $UNI_{act} - UNI_{sens}$ path taken at curing times 365 min and 375 min were plotted in Figure 2.12. It is noticed that right at the time of vitrification, the reflections have increased not only in amplitude but also in the number of peaks. This is noticed because after the part solidified, the plate's boundary reflections and reflections from the nearby placed vacuum probe become more noticeable.

The results for the cure monitoring of the woven CFRP in the second experiment are plotted in Figure 2.13. Almost similar trends to the curves from the previous experiment are noticed. However, the vitrification point for the woven laminate happens at 365 min rather than 375 min in the A_0 velocity plots. On the other hand, the A_0 amplitude curve for the $WOVEN_{act} - WOVEN_{sen}$ path seems distinct from the rest of the curves. The trend would be similar to its counterparts if the curve between 80 min and 345 min is flipped horizontally. It seems that the woven CFRP behaves differently than the unidirectional one during this time. This is especially interesting as the PTFE in this case seemed to have helped to identify the real trend. It is important to point out that the curves of the $PTFE_{act} - PTFE_{sen}$ path for both the unidirectional and woven laminates distinctly show the curing phases and the critical cure monitoring points. The S_0 mode in Figures 2.13 (c) and (d) is shown even in the liquid state for the $WOVEN_{act} - WOVEN_{sen}$ path unlike the $UNI_{act} - UNI_{sen}$ before. While the vitrification onset is noticed in the velocity and voltage curves of the S_0 mode, the minimum viscosity and gelation points are only noticed in the velocity curve.

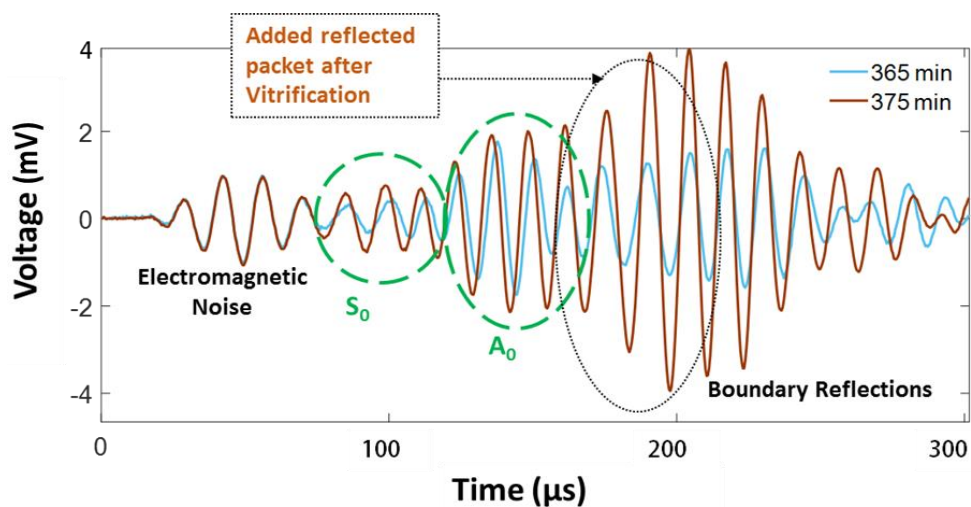


Figure 2.12: Raw data points from the $UNI_{act} - UNI_{sen}$ path showing the wave behavior before and after Vitrification.

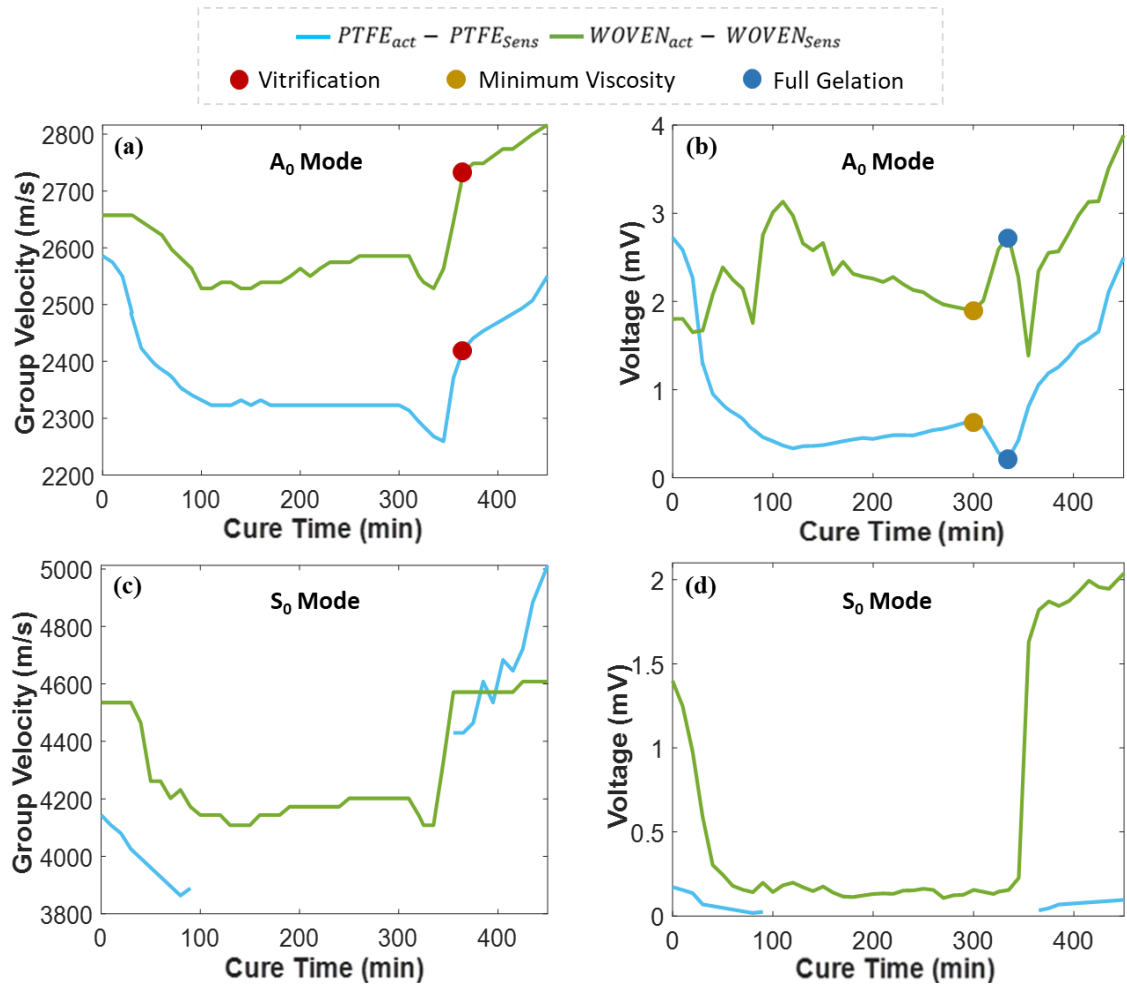


Figure 2.13: Group velocity and Voltage of A_0 and S_0 mode generated and received over the $[0/90/0]$ woven laminate.

2.2.2.2. Post-cure Monitoring

Past curing and removal of the carbon fiber plates from the mould, data was collected for the $UNI_{act} - UNI_{sen}$ and $WOVEN_{act} - WOVEN_{sen}$ paths to monitor the A_0 mode velocity strictly in the cured CFRP. The A_0 mode group velocities were measured at 1365 m/s for the woven CFRP and 1425 m/s for the unidirectional CFRP at 70 kHz, compared to 2830 m/s for the woven CFRP-Aluminum composite and 2816 m/s for the unidirectional CFRP-Aluminum composite. This affirms that when going

through the monitored material, the wave was going inside the aluminum plate too creating a new laminate of both material making the wave faster due to the aluminum characteristics. This phenomenon enhances the cure monitoring since in the liquid stage of the resin, instead of the wave attenuating to degrees that cannot be measured, it is staying visible due to the presence of the aluminum while having the advantages of reading the changes inside the monitored part as seen in the different trendlines.

The two cured plates were placed once more in the same curing cycle and monitored for the second time after already reaching their final glassy state. This was done to check for the indifference in the signal that the $AL_{act} - AL_{sen}$ path showed previously. Figure 2.14 shows the group velocity and voltage curves of these two loose cured plates (woven and unidirectional), the previously discussed aluminum path and one more woven plate that is cured-to-bond with the aluminum plate underneath. The three new velocity curves show the same trend as the aluminum one but with slower speeds. Wang et al. [91] mention that although fibers alone are temperature resistant in terms of mechanical properties, the resin matrix of the CFRP composite is “susceptible” to elevated temperatures thus making the composite rapidly lose strength and stiffness at elevated temperatures that are lower by 20°C or more than its T_g . The measured T_g from DMA experimentation for both unidirectional and woven cured CFRP plates are 110 and 107°C respectively for T_g onset and 122 and 118°C respectively for peak T_g (T_l). This shows in these velocity curves as they are losing velocity almost linearly during the two ramp stages indicating almost linear loss of elastic modulus. The two paths involving aluminum ($AL_{act} - AL_{sen}$ and $WOVEN_{act} - WOVEN_{sen}$ bonded) have a delayed decline in the group velocity or elastic modulus followed by an immediate incline (almost no constant velocity during the 120°C one hour soak), unlike

the two loose carbon plates that have constant velocity during this phase before an increase during the natural cooling stage. The thicker and larger aluminum plate takes more time to reach 120°C homogeneously than the loose thin CFRP plates. Thus, the relatively low values for the T_g onsets mentioned for the two materials above are understandable since they were previously semi-bonded to the Aluminum plate during their first cycle monitoring (during their cure).

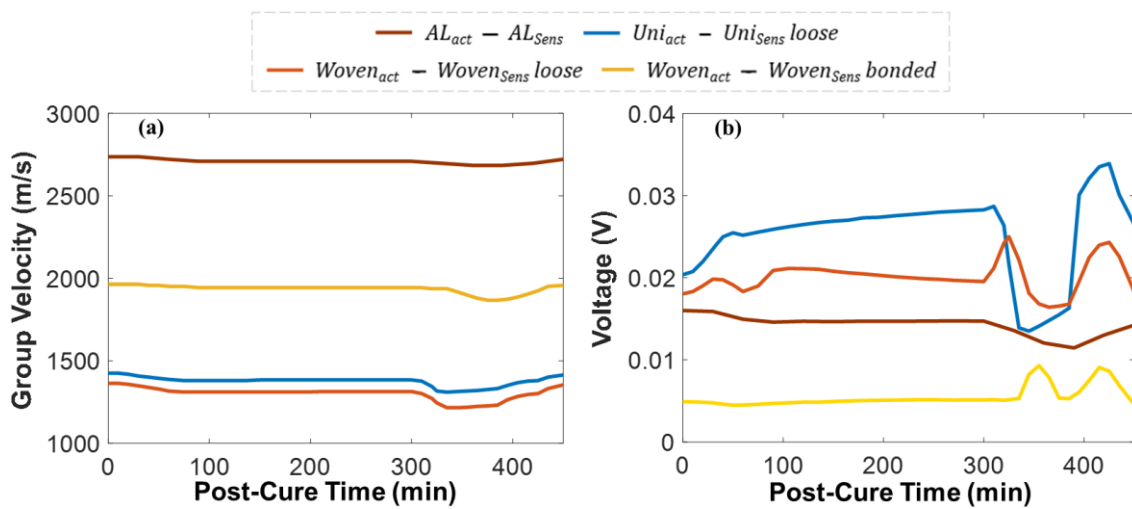


Figure 2.14: (a) Group velocity and (b) Voltage of A_0 mode generated and received along different already-cured material.

The voltage curves on the other hand show that the curves of the two woven CFRP plates are distinct with an unusual trend after min 300 (start of second ramp). Unlike the decrease in voltage seen in $AL_{act} - AL_{sen}$ and $UNI_{act} - UNI_{sen}$ loose paths during this ramp, the two woven plates show an incline in voltage followed by a peak then a decrease leading to the regular trend that the other two curves present after the end of the second soak. This phenomenon present only in woven CFRP plates can be due to the different service temperatures set by the manufacturer to each XC130 and XC110 prepreg material (the difference is mainly in the epoxy resin): the service

temperature for the XC130 (unidirectional one) is 130°C while it is 115°C for the XC110 (woven one). When getting close to the service temperature of the woven CFRP plate and then exceeding it, the resin inside the plate can behave differently and react with the glue that is attached to the PZTs, hence the increase in the voltage during this time. Notice that in the $WOVEN_{act} - WOVEN_{sen} bonded$ voltage curve, this phenomenon is shifted to the right, this is explained by the previous velocity curve analysis: the shift is due to the aluminum taking longer to reach the program temperature. Just as discussed with the Aluminum plate case, the effect of the Lamb wave propagation in the CFRP cured plates is intact in terms of velocity but is not in terms of voltage. The voltage behavior is explained by both T_g and service temperature effects and is still distinct from the previous original cure monitoring analysis, hence the latter is still viable after this investigation. The next section will discuss the feasibility of trimming the cure cycle and monitoring it via the same proposed system.

2.3. Sensing Feasibility of the Proposed System

To validate the previous findings, a change in the curing cycle was made, especially since a reduction of the timeline required for the production and assessment of carbon fiber composites is needed in an industry where manufacturing processes do not provide fast enough cycle time to meet metal alloy processes. To test the possibility of trimming the cure cycle, another experiment is carried out involving the same XPREG XC110 woven carbon fiber prepreg. Very similar to Section C from the previous woven CFRP experiment, this “cycle time reduction” experiment involves the same layup and the same re-usable PTFE-PZTs sandwich sensing film.

The modification in the cycle should be in the longest soak period which is the 4 hours soak at 70°C, especially since the cure parameters, as deduced earlier, were present in the second ramp and second soak stages following the end of this first (4 hours) soak period. The aim is to reduce this soaking period by one hour making the total time of the modified curing cycle 390 min instead of 450 min. The group velocity and voltage amplitude for the dominant A_0 mode for this 3 hours soak experiment were analyzed and compared to the results of the previous experiment, as shown in Figure 2.15. Both curves follow the same trends, however, the one hour shift between them is noticed after the first soak at 70°C is finished. The vitrification point is more reliably taken from the velocity curves while the minimum and maximum viscosity (gelation) points are better determined from the voltage curves. As seen, the three points are shifted exactly by 60 minutes earlier in the new experiment: vitrification moving from 365min to 305min, full gelation from 335min to 275min, and minimum viscosity (always at the end of the long soak) from 300min to 240min.

Although the trends of these curves shown are similar, the range of values differs slightly. The velocity curve in the new 3 hours soak begins at a slightly lower value than its 4 hours soak experiment velocity curve and then after 20 minutes, it surpasses the latter for the rest of the cycle. On the other hand, the amplitude of this A_0 mode in the 3 hours soak experiment is always lower than that in the 4 hours soak experiment. This could be due to a slight difference between the two experiments in either the layup, the amount of silicone release agent between the layup and the aluminum plate, or even the bonding between the sensing film and the layup. Besides these minor differences, the proposed system seems to function properly when monitoring the cure of the carbon fiber laminates regardless of the curing cycle tested.

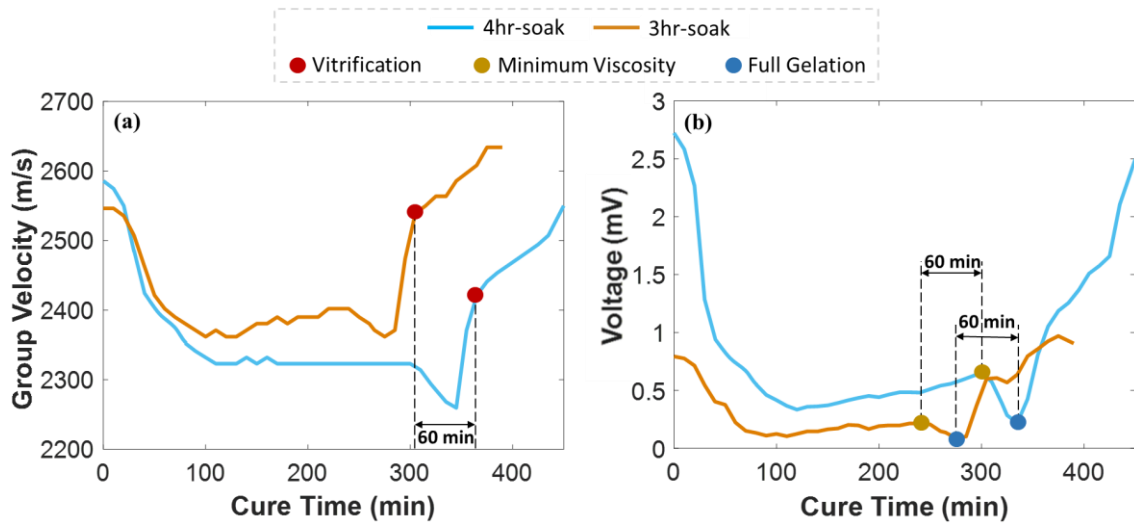


Figure 2.15: Group velocity and Voltage of A_0 mode generated and received over the $[0/90/0]$ woven laminate for the 4hr-soak and 3hr-soak experiments.

2.4. Summary

In this chapter, a reusable flexible thin film of PTFE material was viably used to monitor the curing cycle of two composites: unidirectional and woven pre-impregnated CFRP laminates. First, the best material for the sensing film was chosen by eliminating candidates from both bonding and signal transmission experiments. Then, Skived PTFE was used as a sensing film by having sandwiched two disc shaped PZTs inside. Using this film, identification of important curing parameters such as gelation and vitrification points was done through the analysis of the group velocity and the voltage curves of the generated fundamental Lamb wave modes (mainly the dominant mode A_0 at the used 70 kHz frequency) with the help of the aluminum plate placed below the laminates creating a bond during curing that allowed the monitoring during the liquid phase to be easier. After proving its reliability in terms of cure cycle monitoring, the film was used to monitor a trimmed cycle by one hour for the woven prepreg and prove that the cure

parameters stayed intact. Further studies are required to analyze the behavior of Lamb waves when PTFE layers are present on both sides of the composite plates separating it from the aluminum base plate. Also, more development can be made to further optimize the curing cycle by cutting down more time and enhance the composites industry by making the manufacturing process faster and reducing waste. This system can also be used in future work to monitor in real-time any induced manufacturing defects within the manufactured part while curing.

CHAPTER 3

CURE CYCLE SHORTENING

In the previous chapter, a system that can effectively monitor the composites during curing using ultrasonic waves was implemented successfully. The goal now is to capitalize on that system to shorten the cure cycle time of the tested woven CFRP while making sure that the part is still cured properly. The reusable PTFE thin sensing film is now used to monitor the same cure parameters for a shorter curing cycle than that suggested by the CFRP manufacturer. The results show that the three cure parameters: minimum viscosity, full gelation, and vitrification are offset by the same time deducted from the cycle, verifying that this sensing system is feasible. To validate this ultrasonic detection approach, tensile testing and dynamic mechanical analysis are performed on the same woven CFRP composites. Tensile testing results show that the average tensile modulus for the shortened cycle is of similar values than that of the normal cycle. DMA curing results verify that the time shift of cure parameters is the same as the shortened time, and that the mechanical, thermal, and fatigue properties of the shortened cycle are superior to that of the original one.

3.1. Ultrasonic Non-Destructive Testing

The layed up composite goes into the oven according to the curing cycle set by the manufacturer and shown in Figure 3.1 (4hr-soak). The cure cycle shortening is cut from the longest soak of the cycle, the first one. The modification is cutting 1 full hour of the 4 hours soak period at 70°C, making it a 3hr-soak period. This was done based on a conclusion from Chapter 2 where the cure parameters were present in the second ramp

and second soak stages following the end of this first (4 hour) soak period. Hence the total time of the modified curing cycle would now be 390 min instead of 450 min. The 3hr-soak curing cycle is also shown in Figure 3.1 in the dotted line. The data for both cycles are analyzed through two parameters: A_0 mode group velocity and its amplitude. From previous conclusions, the three curing parameters (minimum viscosity, gelation, and vitrification) are all present in both curves, but the first two appear better in the amplitude curve while vitrification is distinguished more clearly in the velocity curve.

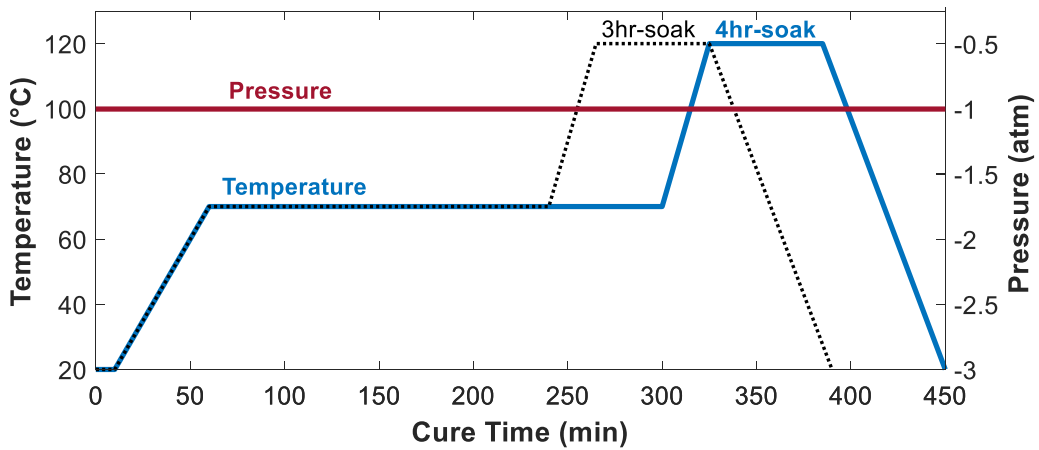


Figure 3.1: Cure cycle proposed by the manufacturer (4hr-soak) and the shortened cycle tested (3hr-soak) shown with vacuum pressure in an out-of-autoclave setup.

The group velocity is basically the distance between the transmitting and receiving transducers, covered by the propagating signal, divided by the time-of-flight between the actuated packet of signal and the first received A_0 mode packet. Figure 3.2 (a) shows the time of flight covered by the first received A_0 packet. The 3rd peak of the wave packet is chosen to calculate the time of flight since it is the highest peak in the five-peak sinusoidal Hanning-windowed signal generated. Although the actuated signal is not shown in the figure, the electromagnetic noise is usually overlapping with it

timewise therefore it is a good estimation to look at it instead; however, the calculations are based on the actual generated signal. Figure 3.2 shows the direct comparison of signals at the three cure parameters points and one final data point at a typical glassy state (minute 390 or 450 for the 3hr-soak and 4hr-soak experiments respectively).

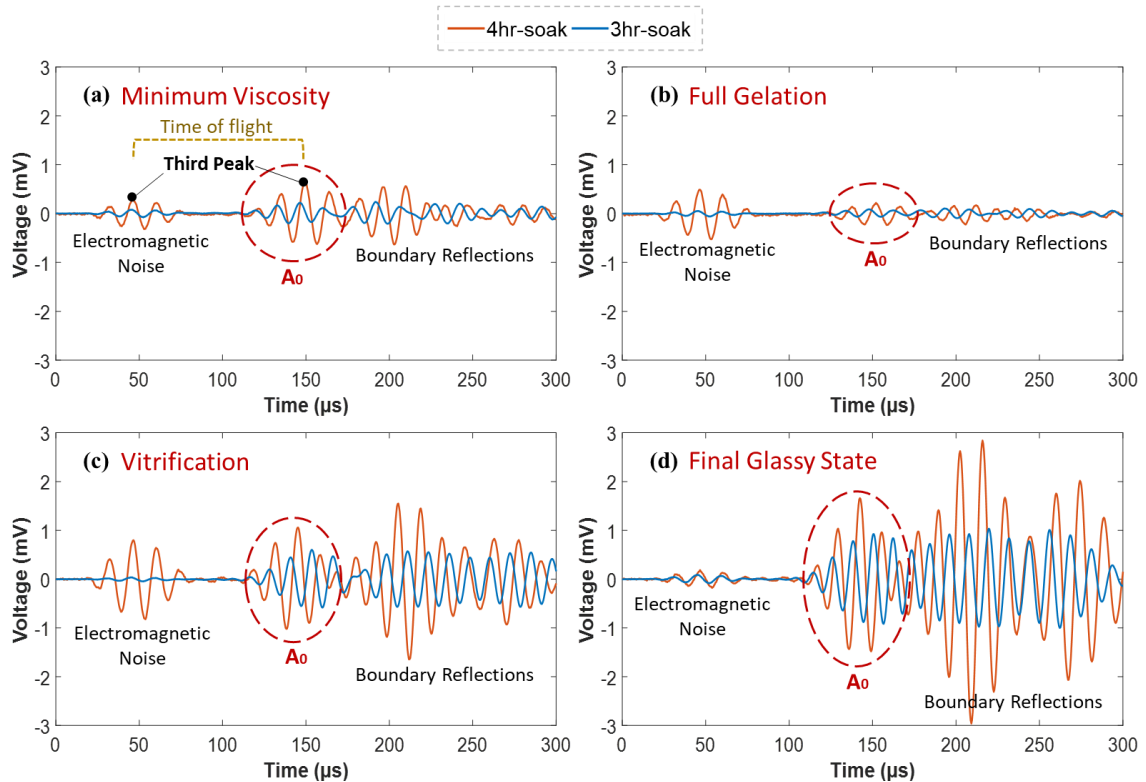


Figure 3.2: Raw data points from the curing experiment comparing cure stages for both cycles.

Figure 2.15 shows the group velocity and voltage curves for both 4hr-soak and 3hr-soak experiments. They follow the same trend, and the one hour shift between them is noticeable after the end of the first soak at 70°C. The cure parameters are deduced for both cycles as follows: the minimum viscosity point is the maximum the end of the first soak. That's where the viscosity of the whole composite, not the resin, is at its lowest; full gelation occurs at the minimum after that, where the viscosity is at its highest in this

rubbery region; then vitrification occurs on the change of slope during the ascent. The latter point is more reliably taken from the velocity curves while the minimum and maximum viscosity (gelation) points are better determined from the voltage curves. Clearly, all three points are shifted exactly by 60 minutes backward in the 3hr-soak experiment: vitrification moving from 365 min to 305 min, full gelation from 335 min to 275 min, and minimum viscosity (always at the end of the long soak- therefore redundant) from 300 min to 240 min. This means that the reduction of the first soak period by one hour kept the curing process functioning normally for the rest of the cycle.

The trends seen in Figure 2.15 are very similar, but the range of values differ from one experiment to another. For example, the velocity curve in the new 3hr-soak cycle starts at a marginally lower value than that in the 4hr-soak experiment but after 20 minutes it surpasses the latter for the rest of the cycle. On the other hand, the amplitude curve of this A_0 wave mode in the 3hr-soak experiment is always lower than that in the 4hr-soak experiment. Several reasons may cause these slight differences in values: minor difference in the layup, inconsistency in the bonding between the sensing film and the layup, or the effect of the shelf life on the CFRP prepreg since the two cycle experiments were tested separated by an extended period of time. These inconsequential variations in the curves' amplitudes have little meaning however. The importance of this cure monitoring method is in the trend of the curve and the time of the cure parameters derived from these curves. After verifying that the cycle reduction of the CFRP kept the curing normal according to the cure parameters deducted by the ultrasonic cure monitoring, more proof is required to make sure that the mechanical properties are kept intact after the part is cured.

3.2. Tensile Testing

The simplest way of inspecting some mechanical properties of the used CFRP is by doing a tensile test which mainly gives information about the tensile strength and the tensile modulus (Young's) of the material. Samples were prepared according to ASTM standards which suggest 25 cm long and 2.5 cm wide samples for the woven composite while leaving some freedom in choosing the thickness (according to the number of laminas) and the tab length (according to the tab material used). [92] Since the layup in the cure monitoring experiments always consisted of 3 layers with [0/90/0] orientation, the same is ought to be used in the samples which makes the thickness around 1 mm. The orientation of the laminas in the tensile testing samples is $[0]_3$ since this will directly give the Young's modulus in the 1st direction of the fibers although the woven nature of this CFRP makes the 0° and 90° directions in-plane have almost the same properties hence it's directly comparable to the previous ultrasonic-experiment layup.

On this basis, 10 specimens were made for each curing cycle, laid-up and cured with 1.5 mm-thick aluminium tabs on each end of the specimen on both sides (4 tabs for each specimen). The tab is 6 cm long and 2 cm wide. Adhesive layers were placed between the tabs and the specimens to ensure bonding while curing. These tabs are essentially used for eliminating slippage of the samples from the UTM grips while the test is running. After curing, the specimens are trimmed properly and each one is tested in the UTM at a 1 mm/min rate. The distance between the two strips of reflective tape, known as gage length, is set to be 10 cm. These white strips are placed to measure the strain in the sample using the laser vibrometer.

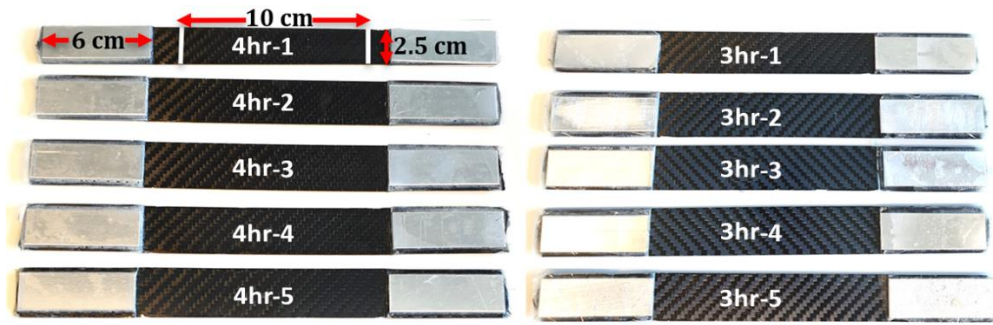


Figure 3.3: Some samples after cure and trim, before tensile testing.

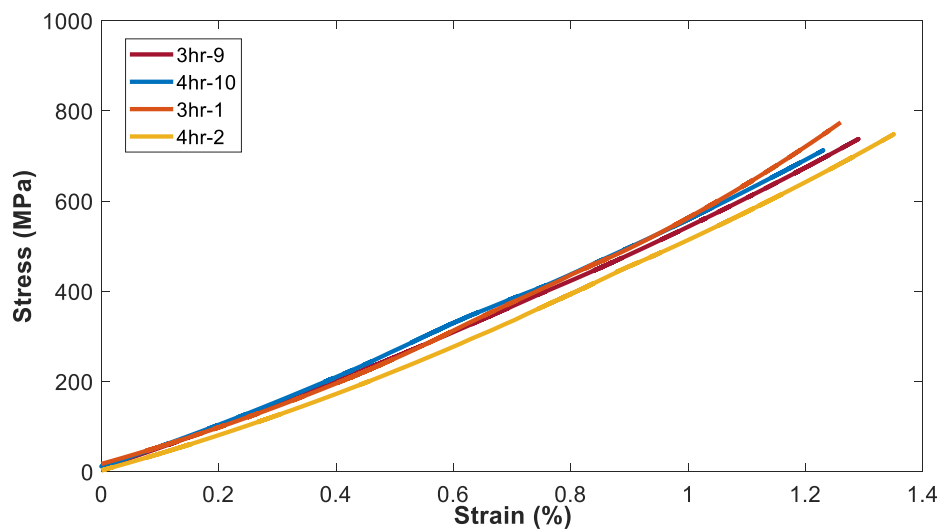


Figure 3.4: Stress-Strain curves for four random tensile-tested specimens.

Figure 3.3 shows the first set of five samples for each cure cycle after curing and trimming. Tensile tests are then carried out for all the samples until failure which happens “suddenly” (fracture) since this is a brittle material. The results of the test show the stress-strain curves which have a direct relationship with the modulus (the slope). The latter is calculated via the insertion of a linear trendline since the curves are almost linear in this brittle test. For the same last reason, the ultimate stress (highest stress on the curve) is the same as the tensile strength since there is no yielding in this case.

Figure 3.4 shows four distinct stress-strain curves, two for the 4hr-soak cycle and two for the 3hr-soak cycle of random specimens.

Figure 3.5 summarizes the tensile test results. It shows the Young's modulus (3.5 (a)) and the strength (3.5 (b)) of the material for each specimen for both curing cycles. The averaged tensile modulus and tensile strength for both cure cycles specimens are shown along with the standard deviation in Table 3.1. The averaged E for the regular 4hr-soak cycle is 50.6 GPa while that of the modified 3hr-soak cycle is higher at 55.8 GPa. The same can be said for the averaged strength as they compare at 671 MPa and 703 MPa, respectively. While the standard deviation is very close in both cases, it can be said that the cycle modification is in fact an enhancement not only by cutting time but also by improving mechanical properties to an extent, especially the tensile modulus. These values should be compared to that of the manufacturer where they claim the tensile modulus to be 55.1 GPa (very close to the 3hr-soak cycle average) and the tensile strength to be 645 MPa (exceeded in both cycles). The enhanced mechanical properties in the trimmed cycle could be due to better and more optimized cross-linking between the matrix and the fibers during curing, especially since the cycle proposed by the manufacturer usually has a safety factor large enough to actually lower the efficiency of this cross-linking. [93]

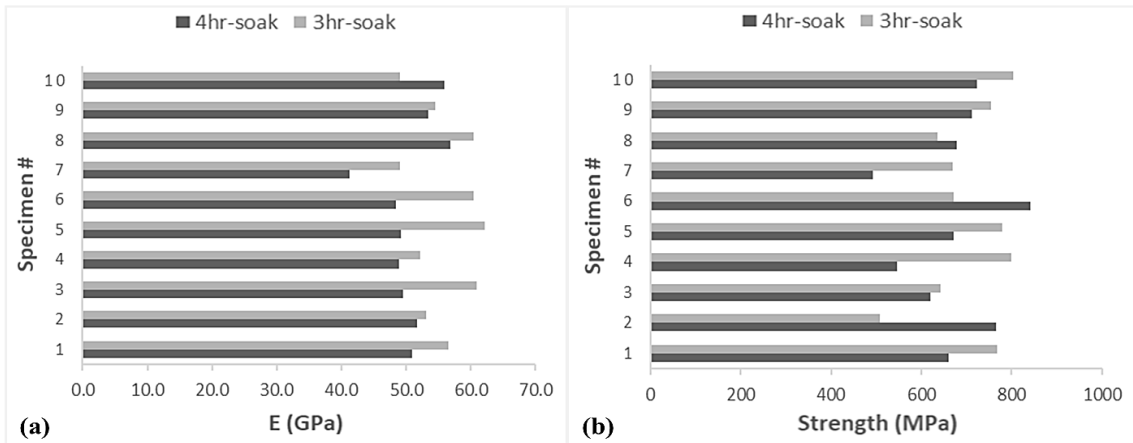


Figure 3.5: Results of the tensile test for all specimens for both cure cycles.

Table 3.1: Averaged tensile modulus and tensile strength for both cure cycles.

Cycle	E (GPa)		Strength (MPa)	
	4hr-soak	3hr-soak	4hr-soak	3hr-soak
Average	50.6	55.8	671.2	703.1
standard deviation	4.4	5.0	101.3	94.6

3.3. Dynamic Mechanical Analysis

To further prove the effectiveness of this cycle time shortening, a DMA machine was used to test both cycles for small woven CFRP specimens. DMA measures the complex modulus and compliance as a function of temperature, time and frequency. Thermoset properties measured include storage and loss modulus, storage and loss compliance, $\tan \delta$ and several more. $\tan \delta$ is the phase lag between stress and strain (the ratio of loss modulus over storage modulus), and a typical measure of damping or energy dissipation. [90]

The most common use for DMA is to get the glass transition temperature T_g . It can also be used to monitor the curing cycle of any polymer. For the latter use, the same cycle can be implemented inside the machine with the addition of a sinusoidal constant strain at a single or several frequencies. [90] In order to compare this reliable method

with the ultrasonic method used in this work, the same cycle is used on the woven prepreg to differentiate the cure parameters. Figure 3.6 shows the setup of the DMA experiment inside the PerkinElmer DMA 8000. A couple of differences between the oven cured CFRP and the DMA tested CFRP are present. First, the size of the sample in DMA ($30 \times 10 \times 1 \text{ mm}^3$ using the same [0/90/0] layup) is much smaller than the original cured plate size and has a much larger thickness to length ratio than the latter. Second, during the DMA test, a constant straining vibration of the specimen is used at a frequency of 1 Hz in a single-cantilever setup with initial force and displacement of 2 N and 0.05 mm, respectively. This cyclic loading is required for the calculation of the gain and loss moduli during the cycle. Last, the specimen in the DMA furnace chamber can't be set under vacuum which is essential to the proper cure and the acquisition of good mechanical properties in the CFRP. However, this test is only performed to verify the previous cycle trimming and its inertness regarding the cure parameters. Therefore, two sets of specimens were tested, some for the regular 4hr-soak cycle and others for the new 3hr-soak cycle.

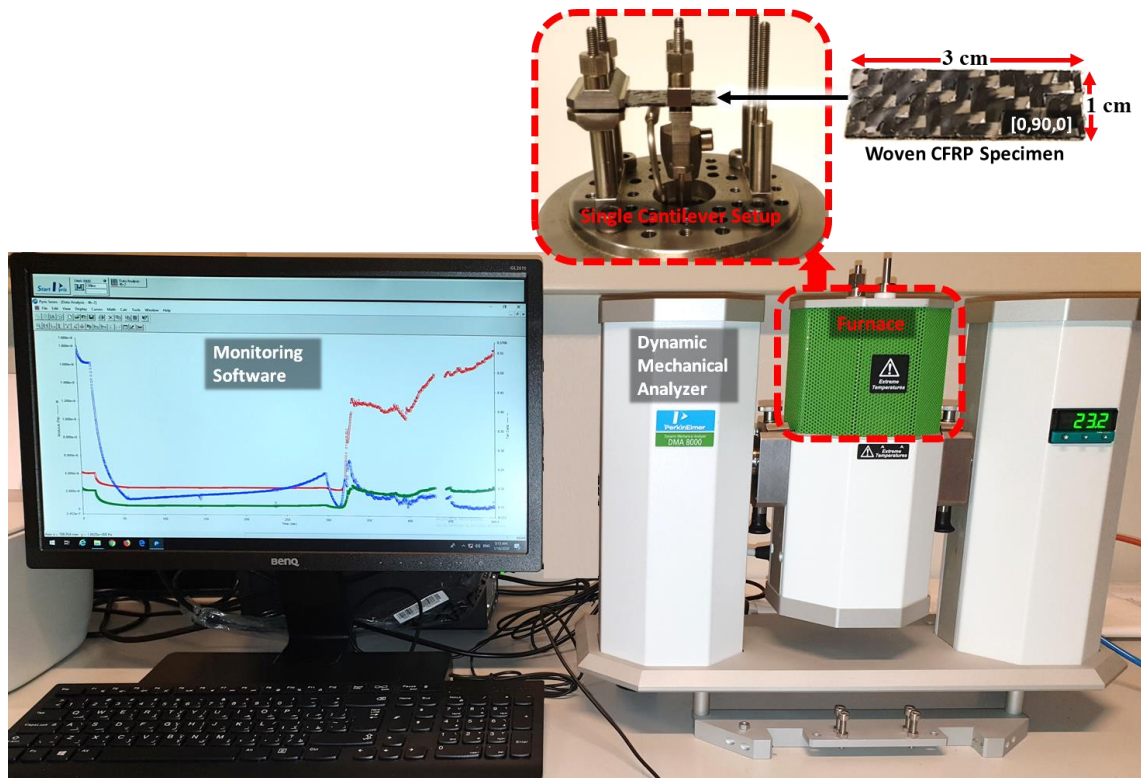


Figure 3.6: Setup of DMA experiments showing the specimen in single cantilever mode.

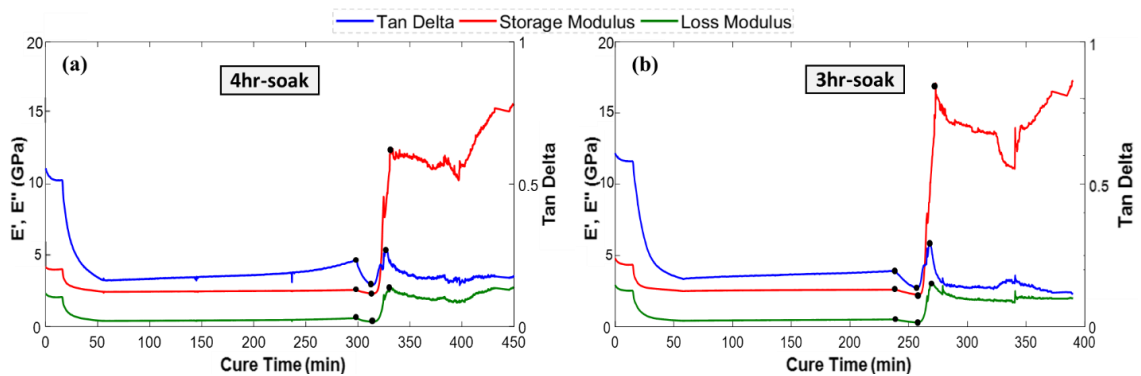


Figure 3.7: DMA results showing loss factor, gain and loss moduli vs cure time for both cycles.

The graphs in Figure 3.7 show the storage and loss moduli, E' and E'' respectively, and $\tan \delta$ (E''/E') with respect to curing time for both cycles. The trends of these curves at first glance directly replicate the trends of the previous ultrasonic curves

with the three main cure parameters clearly present as denoted in black dots. Table 3.2 summarizes the time values of these points concerning both cycles and all three represented curves. Each given time in the table is averaged for five different specimens for each curing cycle. The average time difference between the vitrification onsets of both cycles is 60 minutes while full gelation and minimum viscosity are shifted by 57 and 58 minutes, respectively. This is more dependable and accurate since data is taken every second whereas in the ultrasound case it was taken every 10 minutes hence the minor difference in 2 to 3 minutes. This one hour shift between the cure parameters of the two cycles further proves the effectiveness of this cycle shortening. However, comparing these times to the ultrasonic ones, the minimum viscosity of the resin occurring at the end of the first soak is still present at the same time while gelation is shifted earlier by approximately 20 minutes and vitrification also occurring earlier by almost 35 minutes for both cycles. This could be due to several reasons, some of them are mentioned in the previous paragraph: having different length-to-thickness ratios than the original plates, no vacuum, and cyclic loading at a constant frequency. Also, the small specimen in the furnace is moulded by the temperature faster and better than the respectively larger CFRP plate that is in a large oven surrounded by the vacuum bag, Teflon, and a thick aluminium plate. This time shift in the last two cure parameters between the oven-cured, ultrasonically-tested plate and the DMA-tested specimen can also be considered as a safety factor for the cure cycle, meaning it would be safe to say that the part is cured if the ultrasound cure parameters are present within the cycle.

Table 3.2: Cure parameters deduced from DMA experiment comparing 4hr-soak and 3hr-soak cycles.

	Minimum Viscosity (min)			Full Gelation (min)			Vitrification (min)		
	4hr-soak	3hr-soak	Difference	4hr-soak	3hr-soak	Difference	4hr-soak	3hr-soak	Difference
Storage	296.3	238.9	57.4	314.1	257.7	56.4	331.6	272.9	58.7
Loss	297	238.7	58.3	314.1	257.3	56.8	330.8	269.4	61.4
Tan δ	297	238.7	58.3	314.1	257.3	56.8	327.1	267.2	59.9
Average	296.77	238.77	58	314.1	257.43	57	329.83	269.83	60

As for the variance in values between the curves of each cycle, all three curves start at a slightly higher value for the 3hr-soak specimen, this is due only to the specimen itself. The loss modulus and $\tan \delta$ resemble their counterparts in the two cycles for the rest of the curing time. However, the storage modulus, which indicates mainly the complex dynamic modulus of the specimen (since the loss modulus is very low), ascends to a higher value during the transition from rubbery to glassy state (before vitrification onset) in the 3hr-soak cycle than in the regular 4hr-soak cycle. Then, it keeps on rising at a slower rate after entering the glassy state for both cycles while the 3hr-soak reaching a higher value of around 17.5 GPa compared to 15 GPa in the 4hr-soak cycle case. This affirms the previous results concluded from the tensile test that the mechanical properties of the CFRP at the end of the new shortened cycle are improved. These values for the moduli are low when compared to 51 and 56 GPa for the 4hr-soak and 3hr-soak cycles respectively from the previous tensile test. In fact, Stark tested another carbon fiber prepreg during curing in a DMA machine between -90°C and 280°C. [94] At the minimum temperature, the storage modulus was high at 45 GPa but within the temperature range used in this experiment (above room temperature), the storage modulus had a similar maximum to this experiment (around 15 GPa). This mechanical property value decrease in the DMA while the CFRP is curing inside could be due to the absence of vacuum within the furnace and the extensive dynamic strain on

the specimen while it's curing. This, however, does not affect any of the conclusions as it is sufficient in this test to check for the trend of the curves and compare the cycles to each other.

Curing CFRP inside the dynamic mechanical analyser is not the most traditional use in DMA testing. Conventionally, DMA is used in a heating ramp cycle while oscillating at a constant or varying frequency to find T_g , the glass transition temperature, of these polymer composites. Thus, two sets of specimens of the same size mentioned above, were cured in the oven separately, each by one of the two cycles. After proper curing, these specimens were tested in the DMA machine on a $10^\circ\text{C}/\text{min}$ temperature ramp from 25°C to 180°C and at a frequency of 1 Hz with initial force and displacement of 2 N and 0.05 mm respectively, to get both the initial storage moduli and the glass transition temperature. Traditionally, T_g is found in two ways, either from the $\tan \delta$ peak, or from the first onset of the storage modulus curve drop. The manufacturer states that T_g calculated from the storage modulus curve onset is 121°C , whereas the T_g found from the $\tan \delta$ maximum (usually denoted T_t) is 135°C . The results are summarized in Table 3.3 below. This table shows the averaged values of at least five specimens tested for each cycle. The storage moduli found are comparable to the previous tensile testing results with 54.1 GPa and 50.4 GPa respectively for the 3hr-soak and 4hr-soak cycles, whereas the Young's moduli found previously were 55.8 GPa and 50.6 GPa, respectively. This confirms that the mechanical properties conclusions from the previous experiment are intact at this smaller scale in the DMA machine. As for T_g , in the original 4hr-soak cycle results, the values of 122°C and 136°C are very close to the manufacturer's (difference by only 1°C). In the 3hr-soak case, onset T_g and T_t are 129°C and 142°C respectively, which are also higher than those of the 4hr-soak cycle.

This, and the modulus change, could be due to better cross-linking in the curing of the shortened cycle, and/or a more stress-relaxed composite rubber after the additional 1 hour in the original cycle, resulting in better mechanical and thermal properties for the shortened cycle. Figure 3.8 shows the averaged storage modulus and $\tan \delta$ curves for the woven CFRP specimens of both cycles. Notice that the storage moduli in Table 3.3 were found using many more samples that were tested isothermally only and are not shown in Figure 3.8. This is why in the averaged curves, the storage moduli values at the start of the temperature ramp are different from the storage moduli values in the table.

Table 3.3: Averaged modulus and T_g results for specimens cured in 4hr-soak and 3hr-soak cycles.

	3h-soak specimens	4h-soak specimens
Average E' (GPa)	54.11	50.41
Average T_t ($^{\circ}$C)	142.1	136.2
Average Onset T_g ($^{\circ}$C)	129.1	122.3

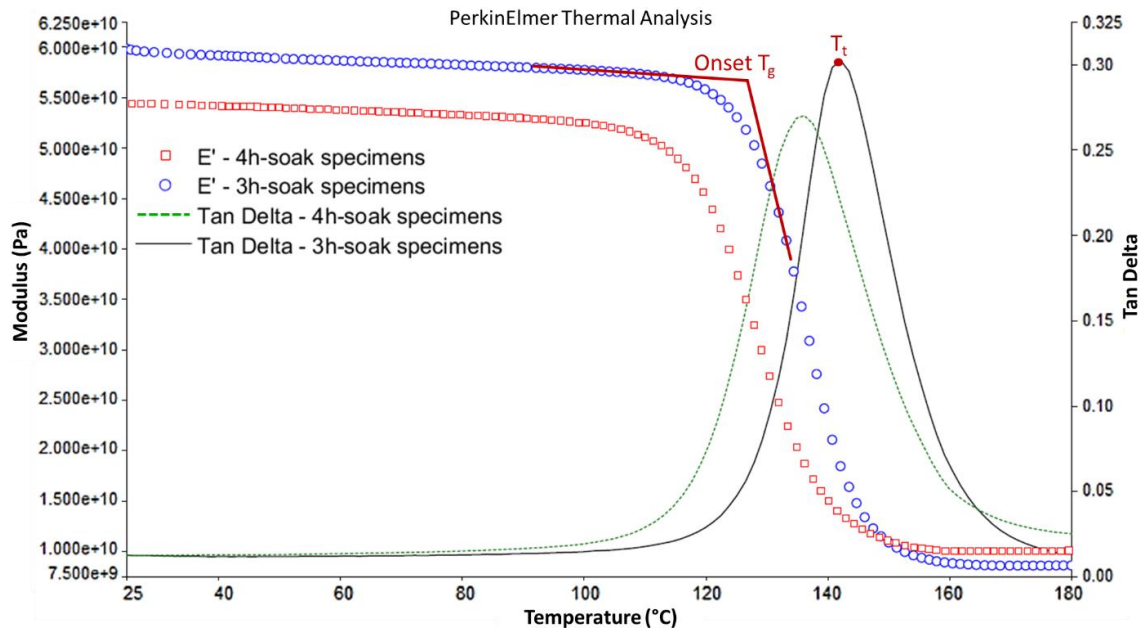


Figure 3.8: DMA temperature ramp results for oven-cured specimens showing averaged storage modulus and tan δ curves for both cycles.

One final use of the DMA machine is to test for creep and compare both cycles in terms of static fatigue properties. Creep is the tendency of a material to strain gradually or deform permanently when constant stress, lower than the strength of the material, is applied. [95] Therefore, it is a time-dependant form of deformation. After extended periods of time, and depending on the properties of the material, creep can lead to static fatigue failure, known as rupture. [96] To compare creep testing for the two cycles in a relatively short period of time, heat should also be added since high temperature expedites the severity of the creep process. Thus, the following experiment was conducted in the DMA machine. Two sets of three specimens, each cured in one of the two cycles, were tested at three different temperatures each: room temperature, T_t temperature, and one in between. The manufacturer T_t temperature is 135°C. At this temperature, the CFRP is clearly rubbery since it surpassed the onset T_g temperature of 121°C and exceeded its service temperature given by the manufacturer (115°C).

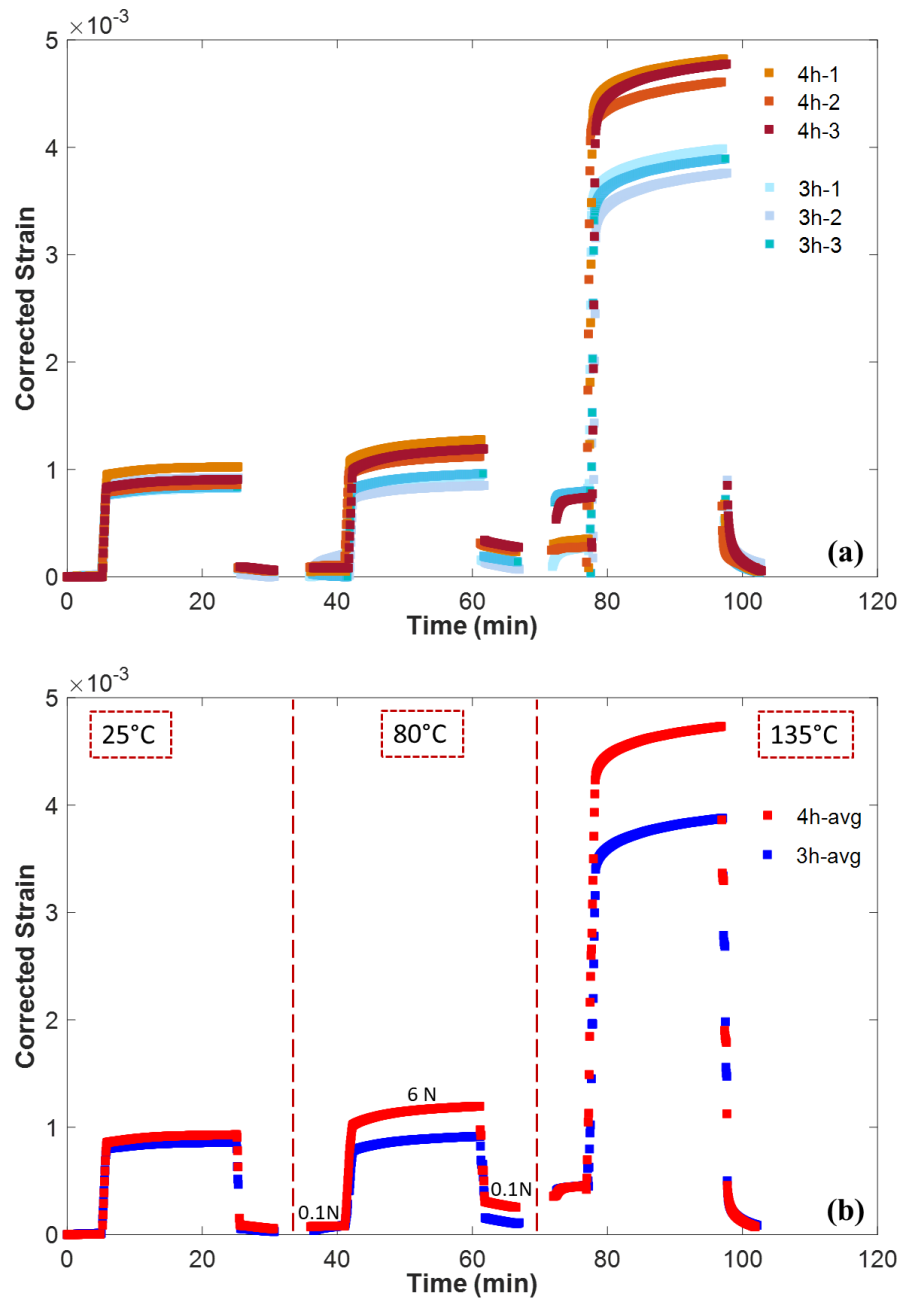


Figure 3.9: Creep test results for (a) all specimens from both cycles, and (b) averaged curves for each cycle, also showing temperature and loading schemes.

The tests are conducted in a way that each specimen will strain for 5 minutes under minimal loading (0.1 N) before promptly increasing the load to 6 N and maintaining it for 20 minutes, then going back to the minimal loading for another five

minutes. After that, the temperature will increase from 25°C to 80°C and the specimen will be loaded in the same previous fashion for 30 minutes. Then the process is again repeated at 135°C. This type of loading is not bound by frequency since it is held statically. Figure 3.9 (a) shows each specimen's strain vs. time during the creep test, and Figure 3.9 (b) shows the averaged strain curves for the 3hr-soak and 4hr-soak cycles specimens. In the latter, it is clear that the response at room temperature is very similar in both averaged curves. After applying the high load at 80°C, the 3hr-soak curve strains less than the 4hr-soak one by an average of 0.03% strain, before also bouncing back to a lower value in the post-load region of 0.1 N. At 135°C, the pre-loaded and post-loaded regions are very similar in both cycles, almost returning to 0.005% (negligible) strain at the end of the experiment. However, within the high-loaded region at this temperature, the 3hr-soak average curve response is much lower than that of the 4hr-soak curve (an average of 0.1% strain difference). This shows that although almost all specimens bounce back to a regular state after loading, the response of the 3hr-soak cycle specimens to this creep test is similar if not better than that of the 4hr-soak cycle specimens, thus confirming that this cycle shortening did not diminish the static fatigue performance of the tested composite. Rather, it might also have improved it.

3.4. Summary

In this chapter, a thin reusable Skived PTFE sensing film was effectively used to shorten the curing cycle time of a woven CFRP laminate by in-situ cure monitoring using Lamb waves at 70 kHz excitation. Three key cure parameters were looked at to determine the cure stages of the laminate and conclude that the cycle shortening was

done successfully, all determined from the velocity and amplitude curves of the recorded A_0 mode: minimum viscosity, full gelation, and vitrification, all occurring after the first soak period which was cut by one hour. The new 3hr-soak curing cycle was then viably tested for Young's modulus and tensile strength by doing tensile testing on specimens that were cured at both cycles. The 3hr-soak cycle proved to have superiority in values of both these properties from averaging ten different specimens for each cycle. To further validate the new cycle enhancement, DMA testing was also used on both cycles in the single cantilever setup. DMA cure findings were similar to both conclusions, as the shift between the cure parameters were also averaged at 1 hour, and the final storage modulus recorded slightly higher values for the 3hr-soak cycles. Then, already cured specimens for both cycles were tested in the DMA machine for storage modulus and glass transition temperature. The findings proved better mechanical and thermal properties for the shortened cycle. Finally, DMA was used to test for static fatigue properties in both cycles. Already cured specimens were tested for creep at three temperature scans and the results showed similar performance for both cycles at 25 °C and 80 °C, and better performance for the shortened cycle at T_g of 135 °C. Thus, the viability of this cycle shortening was proved. More development can be tested in future work to possibly cut the soaking period by more than one hour, or to cut down time on different single-soak cure cycles.

CHAPTER 4

NUMERICAL MODELING

In this chapter, a computational model for a CFRP plate is developed to imitate experimental monitoring of its cure cycle and degree of cure. Using extensive DMA cure testing and averaging the results, the storage modulus for the woven CFRP is determined throughout the curing cycle and its trend is implemented into COMSOL Multiphysics using two modules: solid mechanics and electrostatics, to create a piezoelectric effect and simulate the same mechanical fluctuations of the CFRP during curing. Then, Lamb waves are excited and sensed via sandwiched piezoelectric transducers in a thin PTFE film to replicate the monitoring of the curing plates. Minimum viscosity, gelation and vitrification are the cure parameters observed from analyzing the voltage and velocity curves of the A_0 mode of the sensed signal. The simulations are then repeated for a shortened curing cycle trimmed by one hour compared to the original cycle. In the latter cycle, the same cure parameters are shown offset by the one hour deducted from the cycle, proving that the numerical method is validated. Also, through the analysis of the computationally generated curves, an additional cure parameter defined as “gelation initiation” is proposed. Finally, CFRP viscoelastic properties found from literature are deployed into this numerical model to scrutinize a more accurate response. The velocity wavefields of the propagated signal are also studied to assess this propagation and verify the studied anti-symmetrical mode.

4.1. Experimental Cure Monitoring

To summarize the cure monitoring experiments, the vacuum bagging setup inside the oven is shown again in Figure 4.1. Two cylindrical PZT-5J transducers [0.5mm-thick, 7mm-diameter, 320°C-Curie] are sandwiched by 0.25 mm thick Skived PTFE layers. This sensing film is in direct contact above the CFRP laminate. During vacuum, it adheres temporarily to the laminate, and debonds easily after full curing. This brief adhesion yields enough wave propagation to go through inside both the laminate and the tooling plate. The latter is sprayed with a silicone release agent so that the CFRP does not glue to it. This creates a PTFE-CFRP-Aluminum path for the signal to go through while the cure process occurs. The CFRP laminate and the PTFE films are 220 x 350 mm² in width and length, respectively. The distance between the PZTs inside the PTFE is 240 mm along the 0° direction of the fibers and centred along the 90° direction. The curing cycle set by the manufacturer is as follows: temperature ramps up from room to 70°C in 50 minutes, the part soaks at this temperature for 4 hours, temperature ramps up again to 120°C within 25 minutes, the part soaks for 1 hour, and then cools naturally.

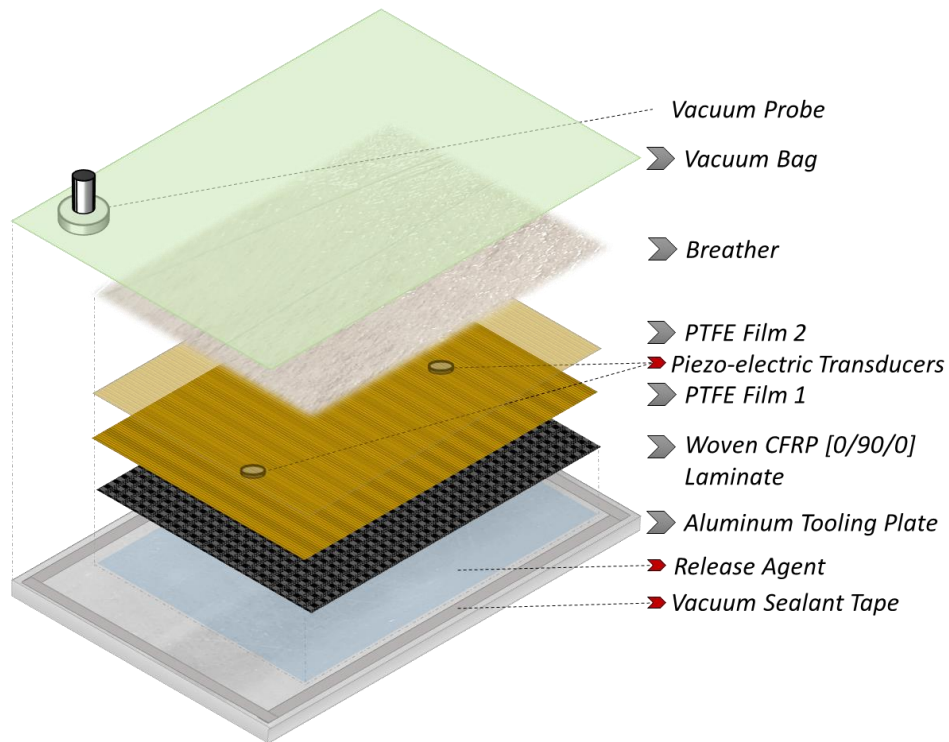


Figure 4.1: Layup process of the CFRP composite along with the described sensing film layers.

The described sensing film is connected, from the wired and soldered PZT actuator to the amplifier which intensify the five-peak sinusoidal Hanning-windowed signal generated by the signal generator. The PZT sensor is connected to an oscilloscope that records the travelling wave signal every ten minutes. The cure cycle shortening by one hour is cut from the first soak of the cycle because minimum viscosity always occurs at the end of this long soak and the other cure parameters are present later. Thus, the total time of the 3hr-soak cure cycle is 390 min compared to 450 min for the original 4hr-soak cycle. The monitoring experiment is repeated for the new cycle and data for both cycles are analyzed through the speed and amplitude of the recorded A_0 mode. Figure 2.15 shows the group velocity and voltage curves for both 4hr-soak and 3hr-soak experiments. Minimum viscosity of the composite is the

maximum before the start of the second ramp. At the following minimum, for both cycles, full gelation occurs denoting the presence of rubber in the polymer. During the following ascent, the change of slope denotes the vitrification point. The latter cure parameter is more effectively extracted from the velocity curves while the minimum viscosity and gelation points are better determined from the voltage curves. [37]

Comparing the two cycles together, all three cure parameters are clearly shifted 60 minutes backward in the 3hr-soak curves. Hence, this cycle time shortening does not affect curing from an ultrasonic standpoint.

To make sure that the cured CFRP by the new 3hr-soak cycle is mechanically inert, DMA is used to compare the mechanical and thermal performance of the two curing cycles. The results show that the properties of the 3hr-soak cured specimens are slightly better than those of the 4hr-soak specimens. The formers have a higher storage modulus, higher T_g , and even better fatigue properties (see Chapter 2) . Thus, after proving the feasibility of the cycle shortening, DMA can also be used to monitor the change in storage modulus during curing for both cycles. This change can then be extracted in a form of a curve trend and implemented into the computational model. Figure 4.2 shows the storage modulus (E') vs the cure time for the 4hr-soak cure cycle inside the DMA at different four different frequencies. Each frequency test is repeated at least five times and the curves shown are averaged for each respective frequency. The averaged curve of all frequencies is also shown in the figure. Curing is performed using $30 \times 10 \times 1 \text{ mm}^3$ woven CFRP specimens of the same orientation as the cure monitoring experiments, while implementing the same cycle ramps and soaks in a single cantilever setup and recording data every second.

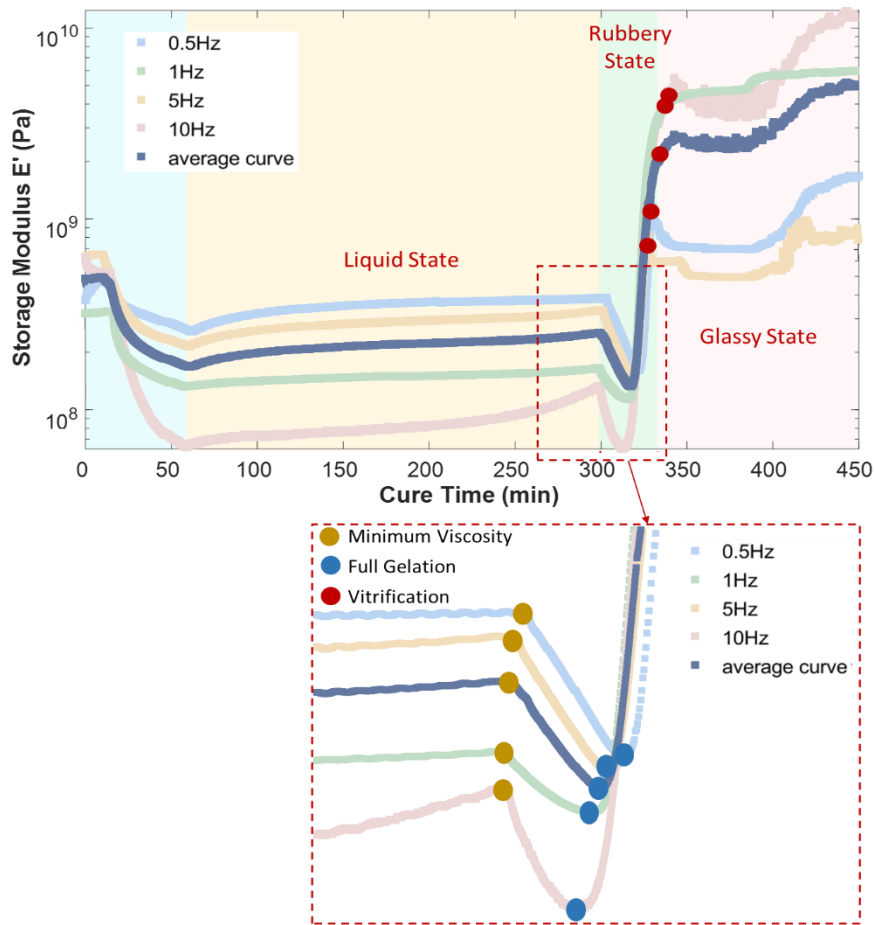


Figure 4.2: DMA 4hr-soak curing results for the woven CFRP specimens tested with the shown frequencies.

Higher and lower frequencies are not available to test at the selected applied force of 2 N, thus this small range of frequencies resulted. Notice that if the 5 Hz curve is neglected, the three other frequencies have a trend such that the higher the frequency, the steeper the curve goes downward in the liquid and rubbery states, and the higher it reaches in the glassy state. However, the 5 Hz curve lies between the 0.5 Hz and the 1 Hz curves for most of the curing cycle, and below the 0.5 Hz curve after vitrification. Nonetheless, it follows the same curve trend and yields the same cure parameters. On the zoomed-in part of Figure 4.2, the minimum viscosity point varies only 3 degrees between 299°C for the 1 Hz and 10 Hz curves and 302°C for the 0.5 Hz curve. The full

gelation point varies 5 degrees between 314°C and 319°C. On the other hand, the vitrification point is almost constant between 330°C for the 0.5 Hz and 5 Hz curves and 331°C for the 1 Hz and 10 Hz curves. This shows that these variations, although present, are minimal and do not affect the average storage curve considerably. This is why testing the 3hr-soak cycle and comparing its average E' curve to the shown 4hr-soak average curve is a valid approach as the frequency variation is not respectively significant. Note that the gelation and vitrification points occur at previous times when compared with Lamb wave results from Figure 2.15: gelation is at 315°C in the DMA results compared to 335°C in the ultrasonics testing, whereas vitrification is at 330°C compared to 365°C (Figures 4.2 and 2.15, respectively). Also, the final storage modulus in the average E' curve reaches around 5 GPa, where in reality, tensile testing of cured samples shows that the Young's modulus in the 0° direction is averaged at 51 and 56 GPa for the 4hr- and 3hr-soak cycles, respectively. These two setbacks could be due to differences in curing environment as there is no vacuum present in the DMA chamber. The small specimen size affects the heat transfer process compared to the large CFRP plate along with all the added bagging consumables and aluminum tooling plate in the ultrasonic cure testing. Also, the cyclic loading and constant straining of the DMA specimens might deteriorate the final mechanical properties and affect the cure parameters. However, this is not a major concern as these DMA curves are only compared to their ultrasonic testing counterparts qualitatively. [94]

Figure 4.3 shows the extracted DMA curing results of the averaged E' curves for both 4hr-soak and 3hr-soak cycles after intentionally amplifying the ascent in the rubbery and glassy regions by a multiple of four. This is done to make the final modulus

of both curves higher and more impactful in wave characterization within the numerical model in COMSOL later on. Note that the modulus reaches higher values for the 3hr-soak cycle in the figure as expected and previously concluded from tensile and DMA testing results in Chapter 3. E' reaches between 20 to 30 GPa in these curves but in reality, cooling inside the DMA is proceeded for another five hours and the storage modulus, after the same amplification, reaches 45 GPa for the 4hr-soak which is 88% of its real final Young's modulus, and 52 GPa for the 3hr-soak which is 93% of its cured Young's modulus. Hence, this multiplication for the curves gives a truer representation for mechanical properties inside the cure monitored CFRP specimens than the actual DMA storage curves. The importance lies in the qualitative nature of the curve trends imported to the FEM software, compared to the quantitative actual storage moduli data.

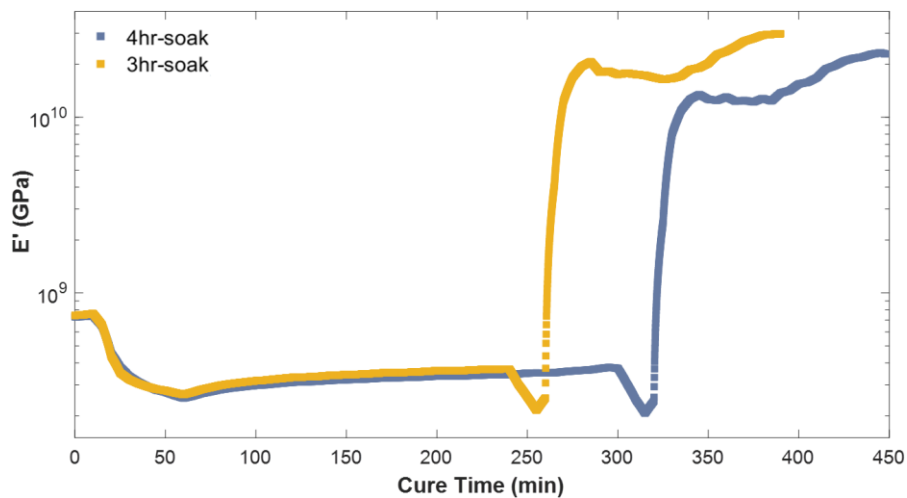


Figure 4.3: The amplified DMA storage modulus average curves for both cycles that are implemented into the computational model.

4.2. Computational Modeling

4.2.1. Material Properties

In COMSOL Multiphysics FEM software, three different blank materials are defined, and one PZT-5J material is assigned from the software's library for the two transducers. Aluminum-1050 and Skived PTFE are defined as isotropic material so that the solid mechanics module requires only each of their Young's modulus (E), Poisson's ratio (ν), and density (ρ), while the additional electrostatics module requires only the relative permittivity (ϵ_r). The material properties for aluminum are found from literature whereas the properties for PTFE are obtained from the manufacturer's technical sheets. [97] Both of these properties are shown in Table 4.1 below and are assumed to stay constant during the curing cycle, although this assumption is not entirely accurate since mechanical properties would be affected by the elevated temperatures, but for the scope of this study, they are considered intact.

Table 4.1: The required properties in COMSOL for the present isotropic materials.

	E (GPa)	ν	ρ (kg/m ³)	ϵ_r
Aluminum-1050	70	0.33	2700	1
Skived PTFE	0.55	0.46	2200	2.1

The woven CFRP laminate is considered an orthotropic material which has the final cured mechanical properties shown in Table 4.2 for both cycles. The Young's modulus in the first direction (E_1) is known from previous tensile testing on specimens cured in each cycle (see Chapter 3). The modulus in the planar 90° direction (E_2) is considered the same as E_1 since this is a woven composite. The modulus in the out-of-plane direction (E_3) is taken as 10% from E_1 and E_2 since it is also assumed to be close to the modulus of epoxy only. The remaining shear moduli and Poisson's ratios in all

directions are obtained by comparing this composite to ones from literature and having these properties proportional to E1 and E2. To make the analysis simpler, Poisson's ratios are assumed the same for both cycles since not enough information is found about the relationship between them and the moduli. The fully cured density is calculated in-lab and the relative permittivity is found from literature. [98,99] The latter is assumed constant throughout the curing cycle. The moduli and Poisson's ratios shown in the table are for the fully cured state in each cycle. To implement the changes in these mechanical properties during curing in COMSOL, a parametric study is deployed on these variables where their values are stored for each five minutes of the curing cycle. This is done by segmenting the previous DMA E' average curves from Figure 4.3 into data points taken each five minutes. Then, E1 and E2 for each cycle are considered to have the same values as the averaged E' moduli throughout the cycle. Figure 4.4 (a) shows the values of E1 and E2 implemented into COMSOL for the 4hr-soak cycle. The remaining moduli E3, G12, G23, and G13 have the same cure curve trend as Figure 4.4 (a) but the values are proportional to their final cured state from Table 4.2. For example, the curve for the implemented E3 modulus for the 4hr-soak cycle is the same as in Figure 4.4 (a) curve but divided by 10.

Table 4.2: Final cured state CFRP mechanical properties for each cycle.

	E1 (GPa)	E2 (GPa)	E3 (GPa)	G12 (GPa)	G23 (GPa)	G13 (GPa)	ν_{12}	ν_{23}	ν_{13}	ρ (kg/m³)	ϵ_r
4hr-soak	51	51	5.1	7.0	4.0	5.0	0.05	0.38	0.38	1800	20
3hr-soak	56	56	5.6	7.7	4.4	5.5	0.05	0.38	0.38	1800	20

As for the Poisson's ratios ν_{12} , ν_{23} , and ν_{13} , the same proportionality is applied with regards to the fully cured values in Table 4.2. However, their trends do not follow

the same averaged DMA storage curve since during the consolidation of the epoxy resin in the first soak period, Poisson's ratio is usually elevated near an incompressible fluid value of 0.5 instead of having a decrease. The rubbery and glassy regions in the curve trends are adjusted to fulfill several claims about the Poisson's ratio during curing for an epoxy resin since ν_{23} and ν_{13} are mainly very similar to the isotropic Poisson's ratio of the impregnated epoxy within the composite. According to Saseendran [100], experimental evidence shows that the viscoelastic Poisson's ratio in the rubbery region can be assumed approximately 0.5 for epoxy resins. O'Brien [101] states that the Poisson's ratio reaches equilibrium where $\nu = 0.4925$ when the shear relaxation modulus fall below a certain value. Since in the scope of this study, viscoelasticity is not considered for the main studied model but discussed shortly at the end, linear elastic Poisson's ratios are considered for ν_{23} and ν_{13} to be just below 0.5 at full gelation and decaying logarithmically until reaching a value slightly higher than that of the fully cured. [102,103]. The final trend implemented in COMSOL for these two Poisson's ratios for the 4hr-soak cycle is shown in Figure 4.4 (b). The ν_{12} trend is the same but proportional to its final fully cured value of 0.05. Due to chemical shrinkage from 0 to almost 6 % after full curing, and the expansion of epoxy due to the heat cure cycle, the density of the curing CFRP is estimated to have a maximum change of 5.8%. It is measured in-lab before the start and after the end of curing, and its curing trend seen in Figure 4.4 (c) is based several statements from literature. It is also based on the combination of the thermal expansion effect and the chemical shrinkage vs degree of cure curve trend. Thus, density ramps slightly during the first and second heating phases until reaching a maximum during the rubbery phase. After full gelation, it starts heavily

decaying before a slope change is noticed just prior to vitrification. After that, it diminishes logarithmically until reaching a final cooled fully cured stage of the CFRP.

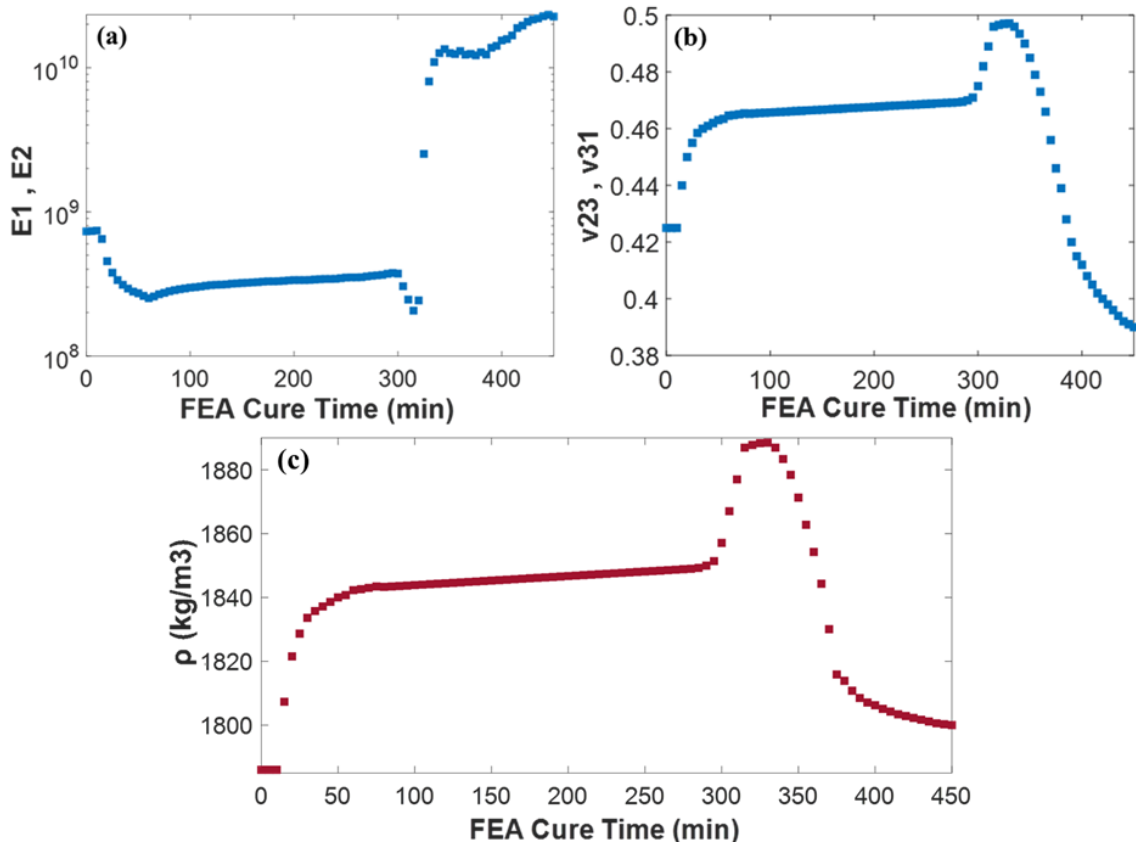


Figure 4.4: Segmented DMA results that are implemented into COMSOL for a parametric study on the mechanical properties of the woven CFRP. (a) Shows E1 and E2 for the 4hr-soak cure cycle segmented directly from the averaged E' curve, (b) shows the v23 and v13 curves for the 4hr-soak cycle based on literature and adjusted proportionally for the rubbery and glassy regions from their fully cured value, and (c) shows the density variations during curing based on chemical shrinkage and thermal expansion variations.

4.2.2. Combined Modules and Numerical Solving

The piezoelectric effect in COMSOL is enabled by combining two physics: structural solid mechanics and electrostatics. The former is governed by the displacement parameters in all three directions whereas the latter is controlled by the voltage calculated from electric displacement field equations. To assign the

“Piezoelectric Devices”, a Piezoelectric Material tab is inserted for both physics and the two transducers are selected so that only their volume is capable of measuring the electric signal. Two Linear Elastic Material tabs are added under solid mechanics. One for the two isotropic materials present and the other for the orthotropic CFRP. Under electrostatics, the upper surface faces of the two PZTs are selected as Ground with zero electric potential, and the lower face of the actuator PZT is designated as the Electric Potential from where the wave is fed and transmitted. The latter is a five-peak sinusoidal Hanning-windowed signal that represents the experimentally actuated wave and is approximated by the following equation:

$$Voltage = C \sin(2\pi f_c t) \left(1 - \cos\left(2\pi f_c \frac{t}{5}\right)\right) \left(flc2hs(t, .0) - flc2hs\left(\frac{t-5}{f_c}\right)\right); \quad (4)$$

where f_c is the excited central frequency of 70 kHz, t is the time in seconds, $flc2hs$ is a smoothed Heaviside step function with a continuous second derivative without overshoot, and C is a multiplication factor that one can vary until reaching the desired voltage amplitude. In this case, C is equal to 41 so that the peak to peak voltage reaches a value of 160 V, mimicking the experimental testing actuated value. The number of peaks in the Hanning-windowed signal is determined by the number 5 in equation (4), changing this number would change the number of peaks present in the transmitted sinusoidal signal.

The model geometry is created by building three blocks and two cylinders to represent the plates and PZTs, respectively. As shown in Figure 4.5, the three CFRP laminas lay on top of the aluminum tooling plate. The Skived PTFE film lays above the composite and is grooved to embed two circular PZT transducers that are capable of

transmitting mechanical and reading electrical signals along the x-axis. This model is scaled to the actual geometry of the experimental setup. The vacuum bagging consumables should have little to no effect on the wave propagation, thus they are not included in the model. There is no boundary conditions on the plate, as it is assumed to be floating in void since we are testing for Lamb wave excitation analysis, and fixating a surface would not be ideal for this application.

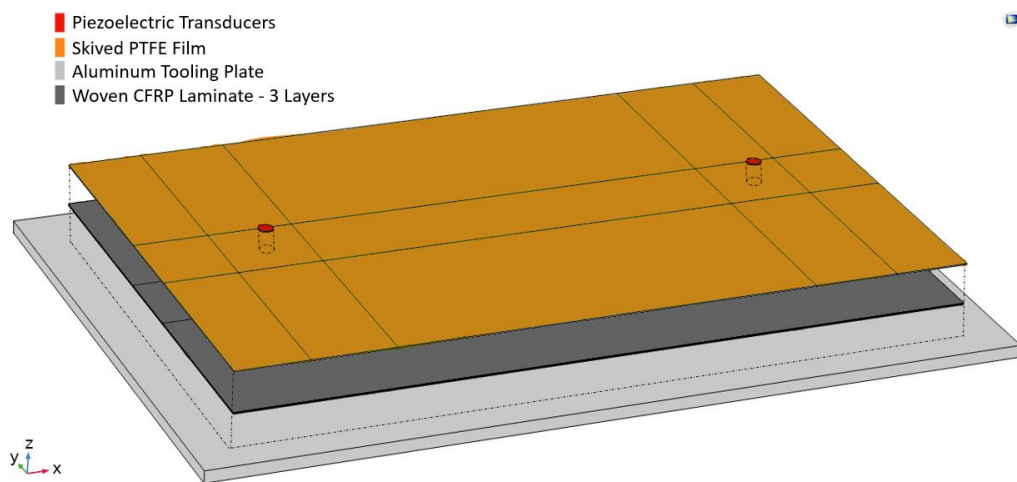


Figure 4.5: Geometry created using the aided design within COMSOL. The parts are spaced from each other in the z-direction only for the purpose of **demonstration** in this image.

Figure 4.6 shows the full meshed model and a zoomed-in scrutinized area around the actuating PZT. The cylindrical transducers are meshed with free tetrahedral elements since this is an area of interest and the mesh density needs to be relatively higher. At some distance from the two PZTs in the x and y-directions, the plates are mapped with quadrilateral or rectangular elements on one surface and extruded throughout the thickness, thus resulting in hexahedral elements for most of the geometry. At the vicinity of the two PZTs, a transition region between the two element

types is mapped on its top surface with triangular elements and extruded to result in prism elements. This is done to effectively connect the nodes in between the hexahedral and tetrahedral elements. As for the sizing, the physics-controlled setting is set to “extremely fine” mesh size but that still does not give sufficiently small “maximum elements” within the geometry to correctly solve for the wave propagation. When modeling elastic Lamb waves, the mesh density or maximum element size has to be dependent on the phase velocity of the slowest propagating mode, which in this case, is the A_0 mode. Usually, an appropriate maximum element size should not be larger than the tenth of the smallest wavelength. [104] The latter is simply the A_0 mode velocity found from the experimental signals divided by the excited frequency. For this model, the wave travels into many media, especially CFRP and aluminum, which both affect the wave mode separation and speed of the transmission. Thus, mesh size iterations are performed to study the mesh convergence rather than using the previously stated method. Results show that the ratio for wavelength over the maximum element size of 7.75 is sufficient for the first received A_0 mode packet, which is the focus of this study, to converge. The value of the mentioned ratio corresponds to a maximum element size of 3 mm. If the latter is reduced, the studied wave mode packet for the compared signals would match exactly at the peaks by both amplitude and time, and would no longer change. Thus, it is computationally optimal to use this size.

To optimize the study and its computation time, the choice of the best solver for the current time dependant model is crucial. **Multifrontal massively parallel sparse direct solver (MUMPS)** is the default solver in COMSOL for the current physics used. Many users advise to use the **parallel direct solver (PARDISO)** for this kind of application. Both softwares solve large systems of linear equations on multicore

processors thus distributing the allocated memory. [105] Another important factor to consider is the time step method used. Generalized alpha is the default transient stepping method in COMSOL. Backward differentiation formula (BDF) is another implicit time stepping method used. The latter is more stable and can be used for several purposes compared to the generalized alpha method, but concurrently generates more damping. [106] BDF is more robust and accurate for large step sizes used because it tends to smooth out any sharp gradients in the solution. This is not always desirable especially if the time step size is small enough to give accurate solution by itself. A brief comparison is made to test each solver with each step method by solving for the established mesh and an arbitrary cure time for the study. The computation time is shown in Table 4.3 for each solver-time step method used. Since all four waves from each simulation produced the exact same signal, the combination that yields the shortest solving time is chosen to solve for the current study: PARDISO – Generalized alpha. Unchecking the “Bunch-Kauffman pivoting” matrix factorization option generates a lower final computation time of approximately 79 minutes.

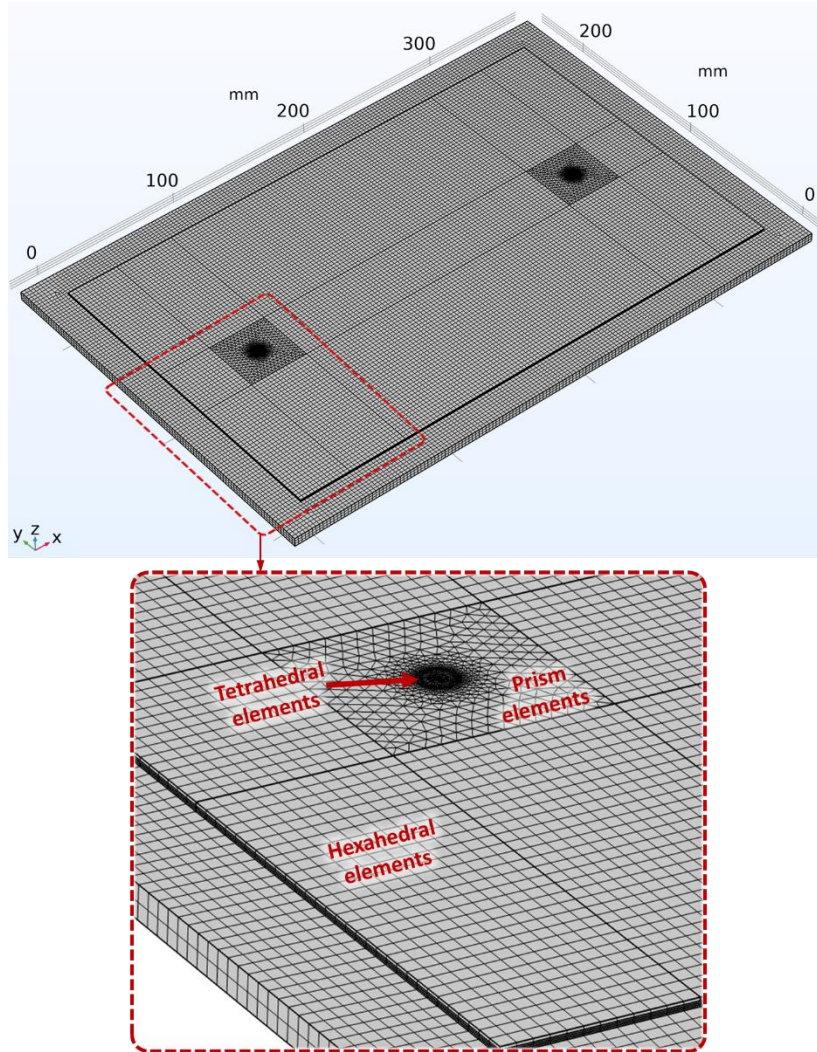


Figure 4.6: The fully meshed model with a maximum element size of 3 mm. There are 4443, 10432, and 39756 tetrahedrons, prisms, and hexahedrons, respectively present in the model, totaling at around $55E+3$ elements.

Table 4.3: Comparison between the computation time of each ‘solver - step method’ combination.

Solver - step method	Solving time
MUMPS – BDF	99 min 06 sec
MUMPS - Generalized alpha	87 min 12 sec
PARDISO – BDF	95 min 31 sec
PARDISO - Generalized alpha	84 min 22 sec

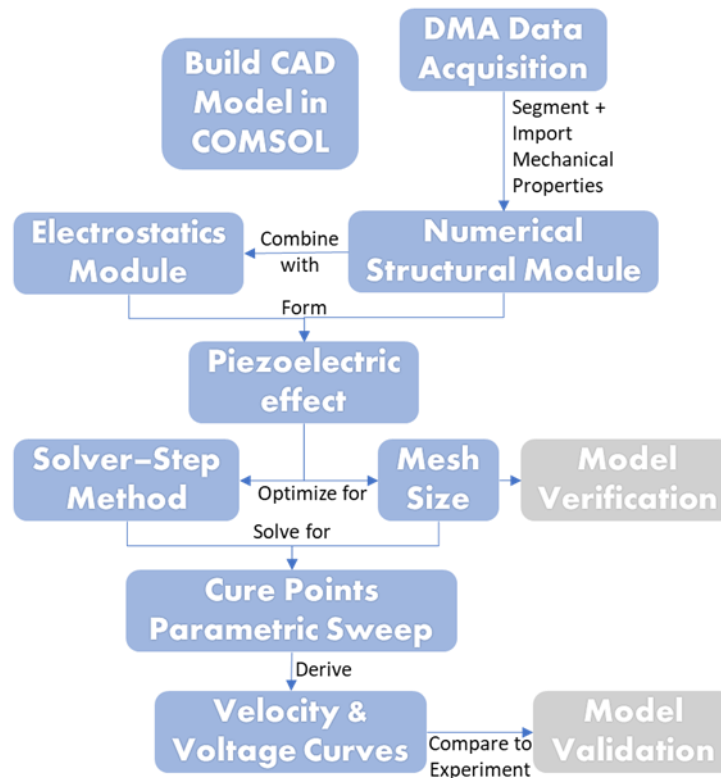


Figure 4.7: An algorithm showing the steps taken before and during solving the computational model.

Finally, a parametric sweep tab is included in the study to account for the changes during curing in all nine listed CFRP mechanical properties listed. This is done for each cycle separately. Since the 4hr-soak and the 3hr-soak cure cycles are respectively 450 min and 390 min long, and the data is segmented to simulate cure data points each five minutes, a total number of 91 simulations for the 4hr-soak cycle and 79 simulations for the 3hr-soak cycle are needed. The time-dependent study is solving for a signal propagation time of $300\ \mu\text{s}$ in each simulation, which is sufficient to receive the A_0 mode in all the curing stages. The time step interval is taken from experimental sampling and is $0.42\ \mu\text{s}$. The importance of a parametric study is that the model runs only once for each cycle. All the data points are solved where each one data point simulation takes about 80 min, and the stored solutions are available for visualization

and processing at the end of all simulations. Figure 4.7 shows a simple algorithm that summarizes the major steps taken before reaching valid numerical results from this computational model. This figure reviews all the discussion in sections 4.1 and 4.2.

4.2.3. Results

At any spatial point inside the cylindrical volumes of the piezoelectric materials, the transmitted mechanical wave can be transformed back into an electrical signal that can be read in Volts. The signal is read at the center of the sensor PZT, meaning at the midpoint of the axis of the cylinder. This imitates the averaging of the signal from the whole PZT during experimental testing. First, we compare results for the fully cured CFRP (not part of the curing trend) with and without the inclusion of the PTFE film, as shown in the signals of Figure 4.8. The amplitude of the signal is clearly affected when adding the PTFE layer beneath the PZTs. This damping, although clearly visible, does not distress the shape and speed of the different modes greatly for the first received wave mode packets. The boundary reflections are of no interest in the current study. The group velocity of the A_0 mode is 2671 m/s for without the PTFE and 2599 m/s with the PTFE. This is calculated by dividing the distance between the transducers (240 mm) by the time-of-flight between the actuator signal and the studied A_0 mode wave packet. The third peak of the wave packet is the one considered for time-of-flight calculations as it is the highest in the five-peak sinusoidal signal generated. From Chapter 2, we know that the group velocity of the A_0 mode in the aluminum tooling plate is 2735 m/s at 70 kHz which is very close to the speed of A_0 mentioned in this case. Knowing, from experimentally generated woven CFRP dispersion curves, that the CFRP A_0 group velocity at 70 kHz is around 1500 m/s, it is concluded that the wave modes are

dominated by the tooling plate and the fluctuations inside the CFRP during curing vary the speeds accordingly.

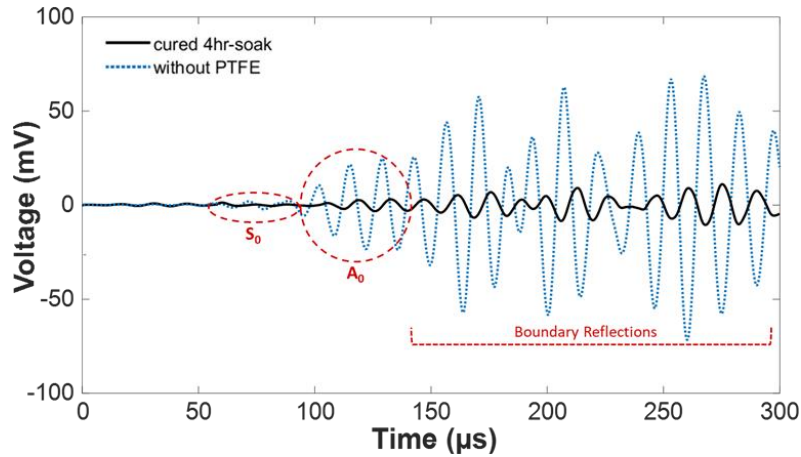


Figure 4.8: Computational signal for the fully cured state of the 4hr-soak cycle with and without PTFE film.

Figure 4.9 shows the comparison between experimental and numerical raw data points at two different cure times. Figure 4.9 (a) compares the results for the 3hr-soak cycle at 10 min which refers to the initiation of the first cure ramp (still at room temperature). The S_0 mode is barely recorded in both signals and the electromagnetic noise, which mimics the actuated signal, is even replicated in a good manner due to the accuracy of the dielectric constant of CFRP in the model. As for the studied A_0 packet, all the peaks fit the experimental signal, so the group velocity is the same. The numerical signal is attenuated slightly more than its experimental counterpart, but the difference is minor. The second packet, where the reflections from the upper and lower aluminum plate boundaries assemble, deviates more from the experimental signal but is still distinguishable. Beyond this reflection, the experimental signal is very damped mainly because of the vacuum bagging tape seen in Figure 4.1. Thus, the numerical

signal has higher peaks, but these packets are not of interest in our study. Figure 4.9 (b) shows the last cure data point in the 4hr-soak cycle experimentally and numerically. The first received A_0 packet also has the same group velocity as the peaks align but the experimental signal is more damped than the numerical one in this case, which makes more sense giving that the material attenuation is not accounted for in the computational model beyond the software's code. Despite this difference in attenuation, we can say that the numerical model gives good representation for the experiments, especially knowing all the simple mechanical assumptions taken in the model.

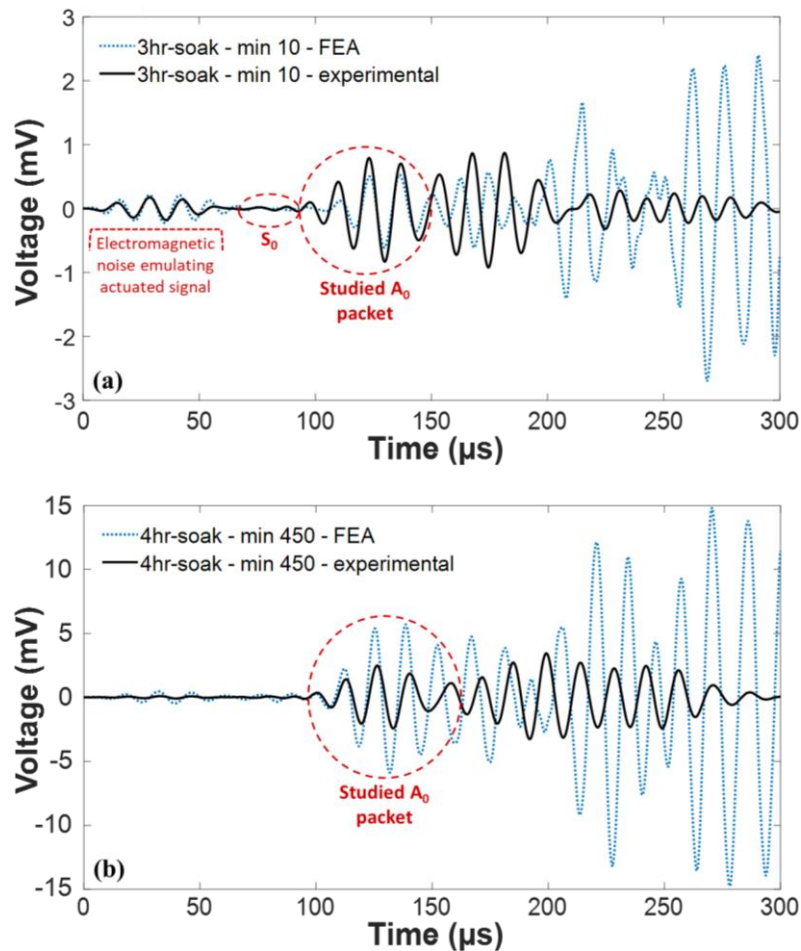


Figure 4.9: Comparing numerically computed signals from COMSOL to raw experimental data.

Signals from the 91 and 79 simulations for the 4hr-soak and 3hr-soak cycles respectively are all analyzed by obtaining the group velocity from the third peak of the A_0 mode and its voltage amplitude at that peak. The resultant group velocity and voltage curves vs. FEA cure time are shown for both cycles are shown in Figure 4.10. Compared to results of Figure 2.15, the same overall curve trends can be observed except for the clear decline in the voltage curves in Figure 4.10 (b) after the ascent in the rubbery region, whereas in Figure 2.15 (b) the voltage acts the same as the group velocity by increasing with a changed lower slope. This can be the effect of the assumptions made on Poisson's ratios during this curing period that are implemented inside the numerical model. To make sure that this is not the case, a brief sensitivity study is performed on the model where the Poisson's ratios are kept constant throughout the cure: the voltage analysis show the same diminishing factor post-vitrification, thus, the numerical model is not highly dependent on this particular parameter. The minimum viscosity maxima sit at the same time numerically and experimentally for each cycle, which is at the end of the first soak. However, the gelation and vitrification points are shifted backwards in the numerical results and appear faster than in the experiments. This is expected since the mechanical properties in this model are imported from DMA results which have the same shift in these two cure parameters. However, when comparing the numerical results for the 3hr-soak and 4hr-soak cycles to each other, the parameters are still 60 minutes apart just like the cycle shortening outcome from the experimental analysis, proving that the numerical method operates effectively by monitoring a CFRP laminate during curing using minimal mechanical property knowledge. In the next chapter, the variation in gelation and vitrification timing between experimental and numerical results is scrutinized further.

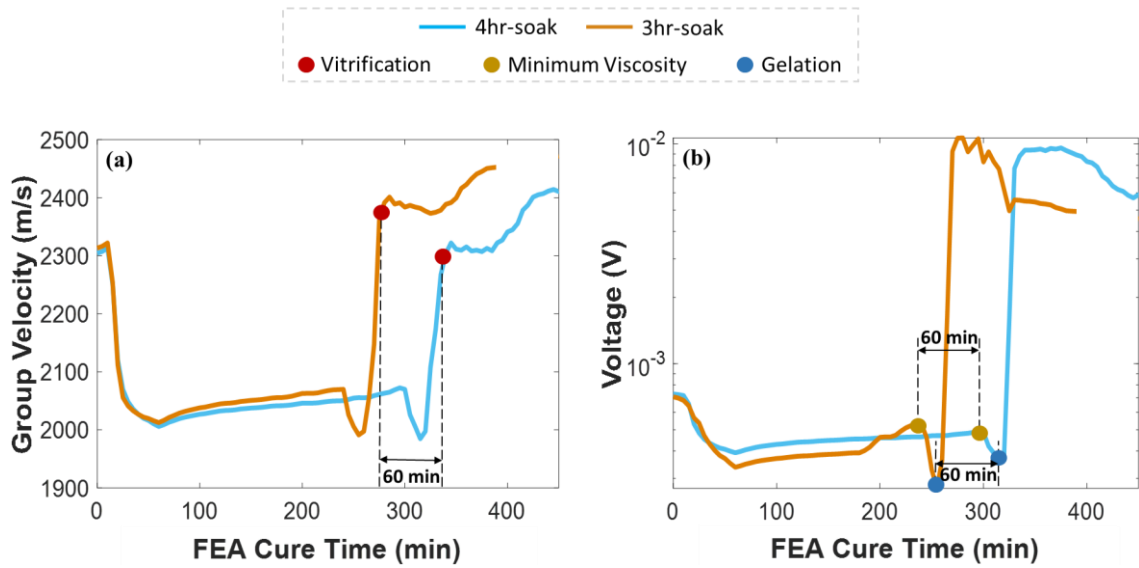


Figure 4.10: (a) Group velocity and (b) Amplitude of the first received A_0 mode packet for both curing cycles extracted from the numerical model simulations.

4.3. Discussion

4.3.1. Viscoelastic Considerations

Any polymer subjected to high temperatures, whether it is cured or not, acts as a viscoelastic material. Viscoelasticity is a characteristic of materials that display both viscous and elastic behaviors under loading. [107,108] In COMSOL, viscoelasticity is included in the solid mechanics module and can be added under the linear elastic material tab. It is fairly more accurate to use this added sub-module to predict the response of any polymer material, especially during curing. This is established by several studies as mentioned in Chapter 1. However, its inclusion would require more degrees of freedom for the software to solve. Also, to get the required constants for the used composite, further experimental testing is required in the form of stress-relaxation and/or DSC experiments. This is why it was not included in the scope of this study. To scrutinize the difference between the presence and absence of viscoelasticity, stress-

relaxation moduli and times are extracted from a similar composite. [109] The ten-branch Generalized Maxwell model includes the shear moduli starting from 5 GPa and descending to 0.8 GPa, and relaxation times increasing from 700 s to $3E+10$ s nonlinearly. The ten branches are added to the simulation of the fully cured state of the 4hr-soak cycle. Results in Figure 4.11 show the minor difference between including and excluding the viscoelastic module. The difference in amplitude between the two signals is negligible, while the scrutinized A_0 mode is slightly faster when the model is paired with viscoelasticity. Its group velocity is 2552 m/s compared to slower 2599 m/s speed of the original model. The heavy computation time derived from the large number of added degrees of freedom does not justify the use of the viscoelasticity module in this study as the improvements to the final results are not of high impact. It is, however, interesting to check this sub-module's effect on signals from different curing stages, especially in the liquid and rubbery regions. It would require further experimental and numerical testing to do so.

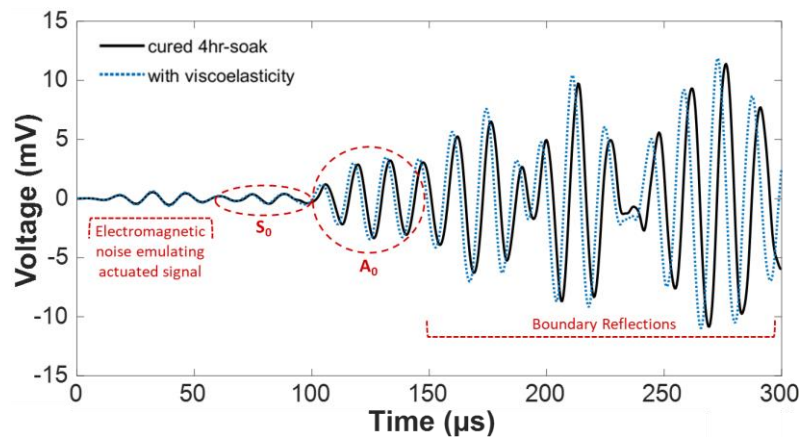


Figure 4.11: Signal comparison for the fully cured 4hr-soak cycle CFRP with and without viscoelastic considerations derived from literature.

4.3.2. *Lamb Wavefields*

One of the main benefits of building a computational model for Lamb wave generation is to visualize the propagation of different modes within the structures. This gives further credibility to many experimental statements such as assuming which mode is which and is extremely helpful when dissecting the boundary and damage reflections. Since the wave generated inside the plates is mechanical, it is more desirable to see its speed as it gives better representation than the electric voltage. Different wave mode types propagate differently as discussed in Chapter 2. The symmetric S_0 mode travels in-plane along with the propagation direction while the anti-symmetric A_0 mode fluctuates in an out-of-plane manner as it propagates. Therefore, the anti-symmetric modes can be seen better from the velocity component in the z-direction (V_z) as this is the out-of-plane through-thickness direction. The symmetric mode can be visualized better from either the x-direction (V_x) or the y-direction (V_y), but since the transducers are distant along the x-axis, V_x is used to scrutinize the S_0 mode propagation. This does not mean that we can only find A_0 along V_z , nor does it mean that we can only see S_0 along V_x . In fact, both modes are included in all velocity components but A_0 is more dominant along V_z while S_0 is more clearly visible along V_x and V_y . In this study, since A_0 is more dominant on this 70 kHz frequency for both CFRP (Figure 1.2 (a)) and aluminum (Chapter 2), it is also dominant over S_0 in V_x component since the laid-up plates on top of one another make an easier path for A_0 (out-of-plane) to travel across them while S_0 (in-plane) is largely damped. In fact, one could argue that the setup of the experiment was always designed to suit the A_0 mode and detect it clearly, rather than detecting a signal and analyzing its modes arbitrarily.

Figure 4.12 shows the propagating wave velocity profiles V_x (a) and V_z (b) in the PTFE-CFRP-Aluminum structure on both upper and lower sides and at different corresponding propagation times for the final curing point in the 4hr-soak cycle. This data point marks the examined signal of Figure 4.9 (b) at 450 min. Figure 4.12 includes the mechanical properties of the CFRP at this cure point and the propagation time at the instant the snapshot is taken on top of the upper boundaries of parts (a) and (b). Figure 4.12 (a) shows both modes in the V_x component at an early time before reaching the sensor PZT on the right. Each mode is clearly distinguished by the different wavelength size and speed. On the lower side of the tooling plate (Side II), the wave modes have the same velocities but are slightly attenuated compared to the upper side, which makes sense since the wave is actuated from a 1.25 mm height above the aluminum plate that is 6 mm thick. Figure 4.12 (b) shows only the visible A_0 mode from the V_z component at a time where the bulk of this mode hits the sensor PZT. The same figure also shows the boundary reflections generated by hitting the sides of the aluminum plate.

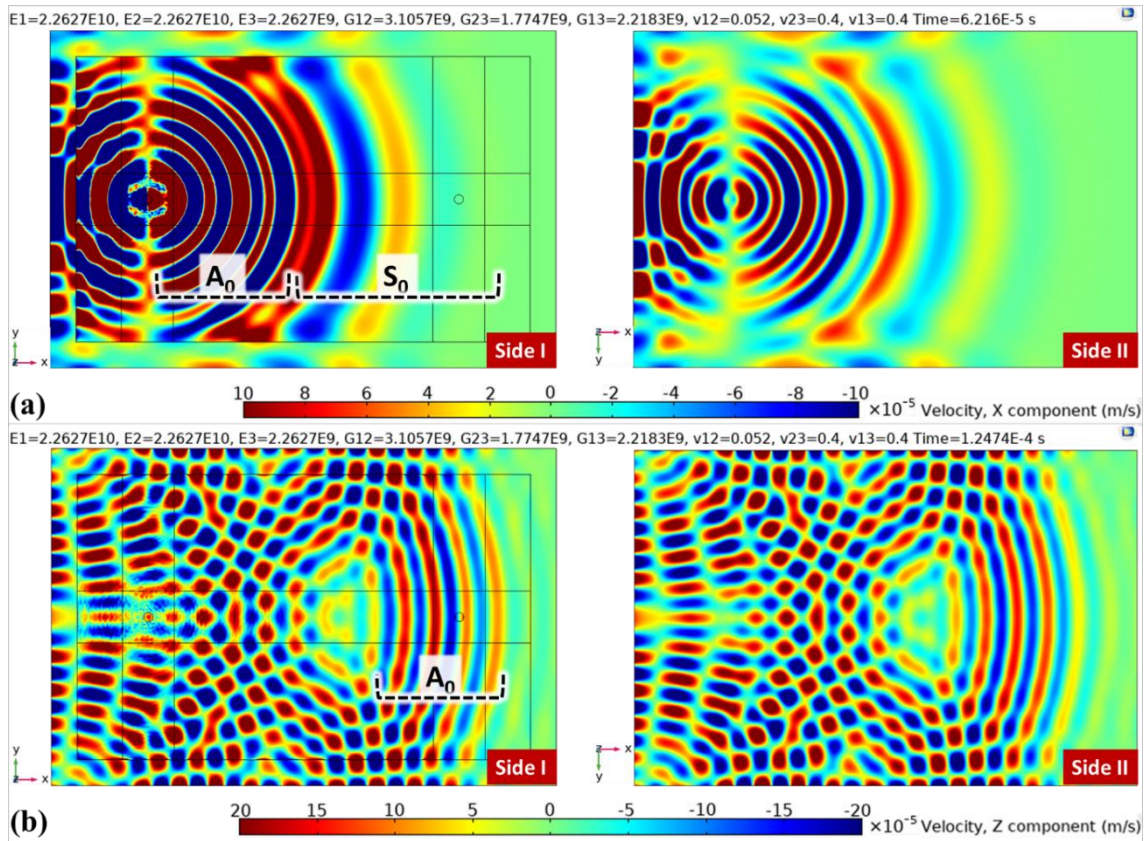


Figure 4.12: Upper and lower views of the Lamb waves velocity profiles inside the PTFE-CFRP-Aluminum structure at 450 min cure time for the 4hr-soak cycle along the (a) X velocity component, and (b) Z velocity component

Figure 4.13 shows the propagating wave velocity profiles along the same directions and propagation times for the third curing point in the 3hr-soak cycle. This data point marks the read signal of Figure 4.9 (a) at 10 min. On Side II for both Figures 4.13 (a) and (b), we notice a similar behavior for the S_0 and A_0 modes as seen in Figure 4.12. On Side I, also the same behavior occurs for the travelling modes inside the PTFE-CFRP-Aluminum structure. However, an added wave packet with smaller wavelength than both modes is shown in the vicinity of the actuator PZT. This is clearly the effect caused by the decreased mechanical properties of the CFRP at the beginning of the cycle. This is why this mode is correlated with the composite laminate tested and not with the whole structure, especially since it does not show on Side II. Particularly,

this can be the A_0 mode generated inside the CFRP solely or inside the PTFE-CFRP structure. In the previous analysis, it was always assumed that the CFRP A_0 mode was travelling inside the aluminum and creating a combined anti-symmetric mode that was analyzed throughout the cycle. That mode would initially reflect on thickness boundaries of the aluminum plate and yield the S_0 and A_0 modes seen during the entirety of curing. Now, however, it is clear that this assumption was incorrect. The added CFRP A_0 mode when the mechanical properties are lower show that the excited wave is initially a symmetric mode inside the CFRP that reflects near the actuator PZT boundaries thus creating both mode conversion and transmission phenomena which yields $S_{CFRP-0A_0}$ and $S_{CFRP-0-S_0}$ modes inside the entire structure, especially inside the aluminum tooling plate which dominates the wave propagation because of its thickness and high mechanical properties. In Figure 4.12, the CFRP A_0 mode does not show because it is faster as a result of the higher laminate properties. Thus, it blends with the total signal because the difference in speeds between them is lower. In Figure 4.13, the same CFRP A_0 mode is so slow that it is almost trapped (static) inside the shown region and keeps reflecting off the actuated PZT and CFRP boundaries (especially shown in Side I of Figure 4.13 (b)). Also, note that the mesh is not optimized to represent the wave propagation of such slow mode, meaning that the shown CFRP A_0 mode is not solved for correctly and can have a slightly different behavior had the model been meshed accordingly. That, however, is too computationally expensive and irrelevant to try for the scope of this study. We are only interested in the generated symmetric and anti-symmetric modes in the entire structure and the latter's changes during the curing process. Nevertheless, the computational model here allows better understanding and

analysis of the wave propagation process by visualizing and understanding the velocity profiles.

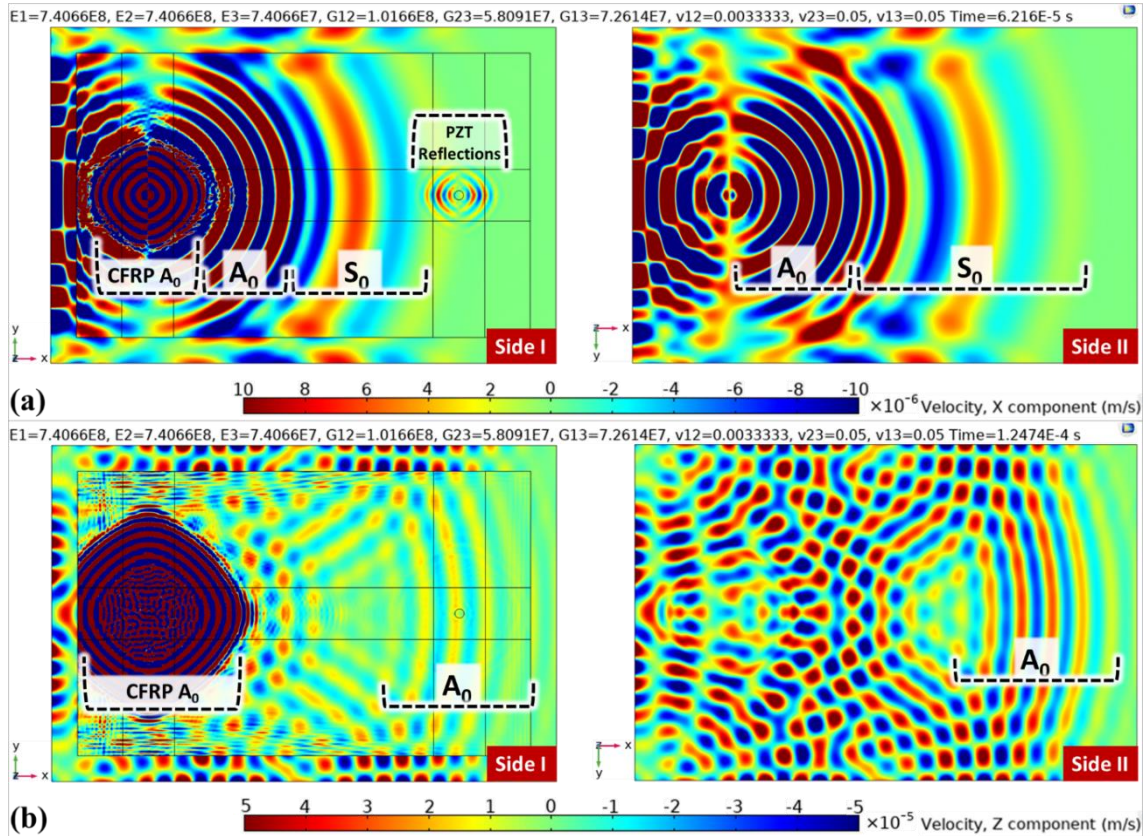


Figure 4.13: Upper and lower views of the Lamb waves velocity profiles inside the PTFE-CFRP-Aluminum structure at 10 min cure time for the 3hr-soak cycle along the (a) X velocity component, and (b) Z velocity component

4.3.3. Added Cure Parameter

To improve the comparison between the experimental and numerical findings of the group velocity and voltage curves vs cure time, the results are shown together in Figure 4.14. The previously assigned vitrification points for the numerical results from Figure 4.10 are changed because it is noticed that the velocity curves (Figure 4.10 (a)) indicate a change of slope near the end of cure with times very close to the experimental vitrification times for both cycles (which are indicated by the slope change in the

ascent). Figure 4.14 (c) shows the new assigned vitrification points for the numerical results at 315 min and 375 min for the 3hr-soak and 4hr-soak cycles, respectively. These values compare very closely to 305 min and 365 min vitrification points for the experimental 3hr-soak and 4hr-soak cycles. In Figure 4.10 (a), they were assigned at 280 min and 340 min accordingly. The considered gelation points in Figure 4.10 (b) are very close in time to the minimum viscosity points separated by only 15 minutes for each cycle. The new full gelation considerations in Figure 4.14 (d) are at the end of the rubbery region ascent in the numerical voltage curves at 270 min and 330 min for the 3hr-soak and 4hr-soak cycles. Compared to the minima in experimental voltage curves of Figure 4.14 (b), they differ by only five minutes since full gelation points are set to 275 min and 335 min for the 3hr-soak and 4hr-soak cycles in these experimental results. In Figure 4.10 (b), they were assigned at 255 min and 315 min for the 3hr-soak and 4hr-soak cycles. The new times for full gelation and vitrification points for the numerical results (Figures 4.14 (c) and (d)) make more sense than those assigned in Figure 4.10 since they are closer to their experimental counterparts (Figures 4.14 (a) and (b)). If this is the correct case, there remain the minima of the numerical velocity and voltage curves in Figures 4.14 (c) and (d) that is not assigned to neither full gelation nor vitrification. Since this new parameter appears at the same time in the voltage and velocity curves for each cycle, it is labeled by a hollow black circle in both figures. The times here are 255 min and 315 min for the 3hr-soak and 4hr-soak, respectively. When projected up to the experimental results in Figures 4.14 (a) and (b), it is shown how the black circle lies between the minimum viscosity and the full gelation points, in the second descent of the curves occurring during the second temperature ramp. Since this new parameter is fairly close to the minimum viscosity points, it can be implied that the

initiation of the gelation process occurs at these times. Thus, a new added cure parameter called “gelation initiation” is assigned in Figure 4.14. This cure parameter is also shifted by exactly 60 minutes backwards for the 3hr-soak cycle. If these assumptions are not correct, the differences between gelation and vitrification points for the ultrasonic experimental test and the DMA generated E' curves would still be due to the several reasons stated previously: difference in vacuum and bagging material, tooling plate and heat transfer consideration, and the difference in the length-to-thickness ratio of the specimens for both experiments.

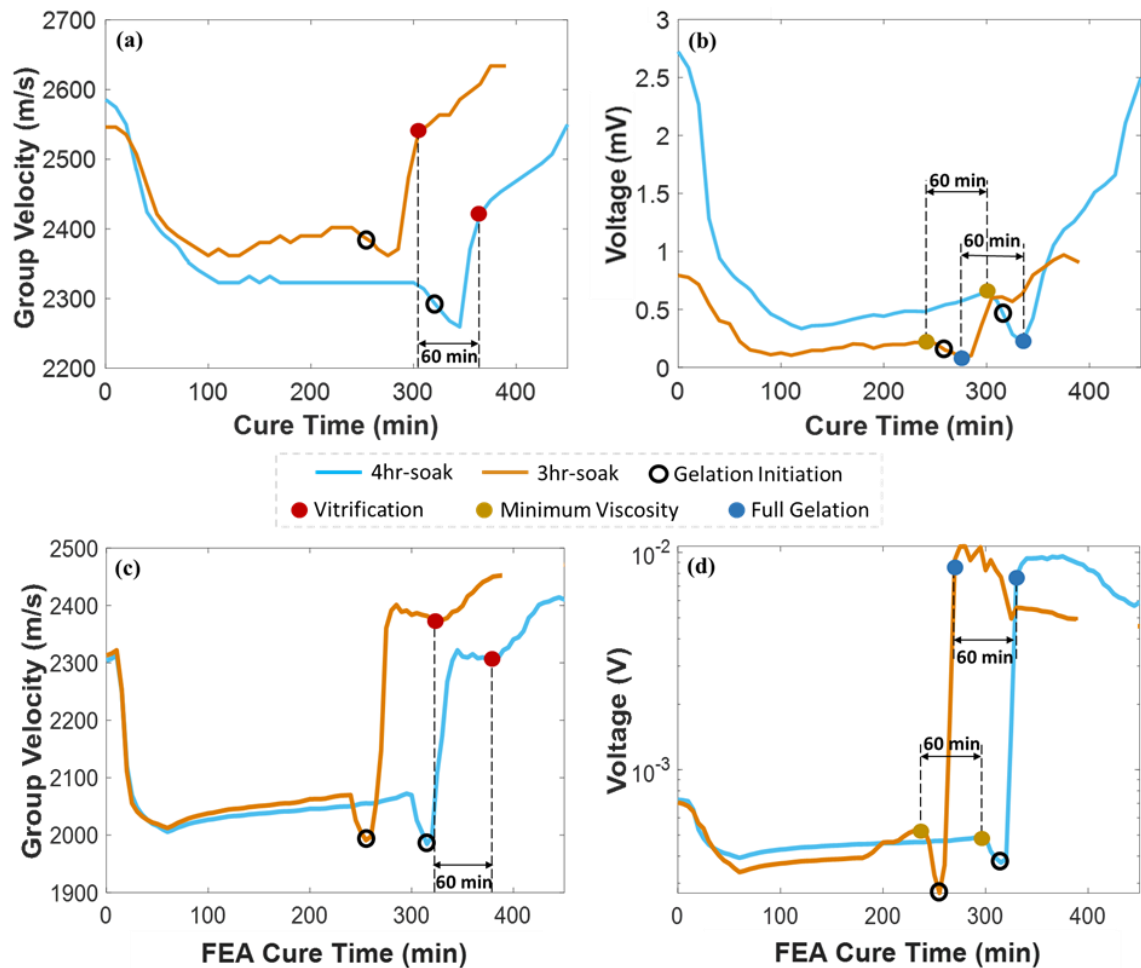


Figure 4.14: Rearrangement of the gelation and vitrification cure parameters points for the numerical results. (a) and (b) show, respectively, the group velocity and voltage

curves vs experimental cure time. (c) and (d) show, respectively, the numerically generated group velocity and voltage curves vs FEA cure time.

Further studies and validation are needed to justify the inclusion of the new gelation initiation parameter and the rearrangement of full gelation and vitrification points for the numerical study. However, if accurate, these changes should also be applied to the DMA storage moduli curves since they have the main influence on the numerical model results considering all the CFRP material properties changes during the cure are extracted from these curves. Thus, the cure parameters in Figure 4.2 are rearranged accordingly to include the gelation initiation parameter and to shift the full gelation and vitrification parameters. Figure 4.15 shows the implementation of these changes and their effect on the adjusted rubbery and glassy states regions. The rubbery region now starts from the gelation initiation parameter, which is relatively close to the minimum viscosity, and extends to the new assumed vitrification time spot. The glassy state is also shifted to start from the latter cure parameter and extends to the end of the cure cycle.

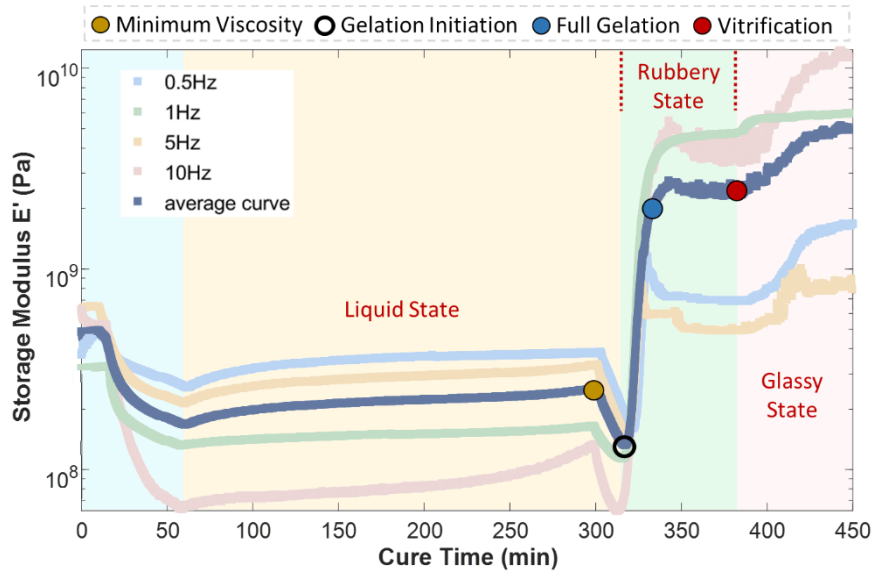


Figure 4.15: Rearranged states for the DMA 4hr-soak curing results of the woven CFRP specimens tested with different frequencies. The rearrangement includes the new assumed “gelation initiation” cure parameter where the rubbery region starts. The relocated vitrification point also shifts the rubbery region end / glassy region start.

4.3.4. Study Limitations

This numerical study yields good results overall, but many assumptions are made along the different sections. First, the DMA frequency range for the cure testing can be enlarged to get a more accurate average E' curve. Also, the loss modulus E'' and/or the $\tan \delta$ parameter are not considered for this study. They could slightly change the implemented modulus curve in COMSOL if employed. The averaged storage moduli curves for both cycles are amplified by a factor of four for better signal propagation response in the software. On the other hand, the changes in moduli for CFRP are all based on the imported storage modulus changes. Aluminum and PTFE are assumed to have no property changes during the increase in temperature, whereas in reality, their mechanical properties have slight changes. Also, relative permittivity of the woven CFRP is assumed to stay constant during the cure, which is not entirely accurate. Moreover, the Poisson’s ratios assumptions within and after the rubbery

region clearly affected the resulting voltage curves. This is why, after slope change in this region, the amplitude of the signals starts to decrease although it keeps rising in the experimental test results. Modeling-wise, the exclusion of the different bagging consumables might affect the resulting signal. Particularly, modeling the vacuum gum tape correctly around the aluminum plate edges might improve the reflections accuracy of the studied mode. Additionally, viscoelasticity is ignored because it needs more experimental testing and generates large numbers of degrees of freedom and hefty computational time within the model. Further studies on the wavefield velocity profile are required to validate the claims about the slow CFRP A₀ mode at uncured stages. Finally, theoretical and experimental validations are needed to justify the statements about the new “gelation initiation” cure parameter.

4.3.5. *Practical Importance of the Numerical Model*

Since the crosslinking reaction is irreversible, the absolute values of voltage and velocity fluctuations can be integrated over time using the following equation by Liu X et al.:

$$\int_{t_1}^{t_n} X dt \approx \sum_{i=1}^{n-2} (t_{i+1} - t_i)(|x_{i+2} - x_{i+1}| + |x_{i+1} - x_i|); \quad (5)$$

where x_i is the studied parameter (voltage or velocity) at a time t_i . The data is then normalized to get the progress of reaction (POR) curves, or degree of cure, of experimental and numerical results for each parameter and for each curing cycle. The results are shown in Figures 4.16 (a) and (b) for the POR curves integrated from velocity and voltage curves, respectively. The figures compare POR from experimental

and numerical studies at both cycles. The velocity POR curves show very similar trends between the numerical and experimental trends for each cycle. The FEA curves have a slight lead in time after the gelation process commences. This is understandable since the DMA curing parameters occur prior to those of the ultrasonically tested experiments. Other than that, the numerical trends compare to their experimental counterparts quite effectively. The FEA voltage POR curves, however, have very low values compared to the experimental voltage POR curves, until minimum viscosity occurs. The curves then match for both cycles until the end of the cure.

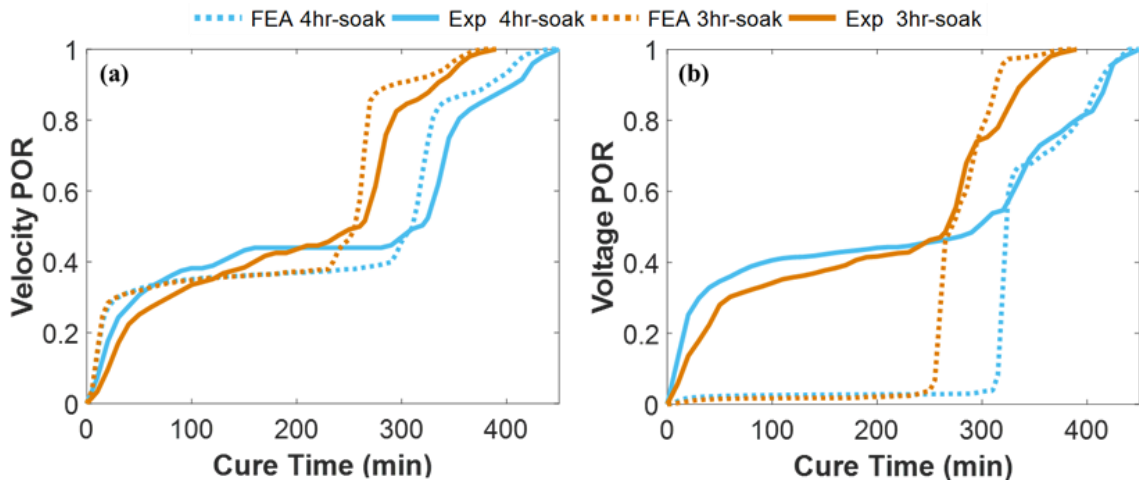


Figure 4.16: Progress of reaction (POR) curves normalized vs cure time as derived from (a) group velocity curves and (b) voltage curves. These results are shown for both cycles experimentally and numerically.

This preliminary calculation of the degree of cure in the form of POR lays the roadmap for future projects that expand on the use of this numerical model. The end goal is to reach a full digital twin that conveys information to the user prior to the experimental setup, thus, optimizing the entire cure monitoring process and reducing material waste. Reaching this stage would require, as previously mentioned, the

addition of other modules to the numerical model. These are ‘heat transfer’ and ‘differential equations’ modules to emulate the chemical reaction effect by simulating the curing kinetics. This addition needs prior DSC testing to acquire all the kinetic constants for the Arrhenius equation of the curing CFRP. Viscoelastic sub-module would also be required to simulate the proper mechanical performance of the curing polymer composite. Supplementing the numerical model with the latter module demands stress-relaxation experiments to find all the constants during several curing phases. Combining all of these additions with the current developed model will definitely add value and novelty in future advancements. The numerical model would then be used to simulate new parts and structures that have different shapes and sizes where the cure monitoring readings would behave distinctly for each part. The cure monitoring of complex shapes numerically prior to fabrication gives the objective of this work a real practical importance, especially that the ultrasonic guided waves technique is valid for systems that cure at any pace, whether slow or rapid.

4.4. Summary

In this work, a numerical model for woven CFRP cure monitoring of a shortened curing cycle using guided Lamb waves is presented. First, the experimental ultrasonic results and conclusions are described such that the three main cure parameters: minimum viscosity, gelation, and vitrification are presented on the velocity and voltage curves. Then, DMA curing storage modulus results are extracted for both the original and a trimmed cycle by one hour and imported into COMSOL Multiphysics after segmenting data points each five minutes and amplifying the curve trends by a constant factor. All CFRP mechanical properties are taken as function of the E’ trend, each with

respect to their known final cured stage value. The numerical model is introduced by combining the solid mechanics and electrostatics physics in COMSOL. The geometry and mesh are described and the criteria for the time-dependent solver is defined. The numerical results show that the Lamb wave received signals match the experimental raw data especially in the studied region of the first received anti-symmetric mode. The concluded velocity and voltage curves are then compared to the experimental results as the cure parameters are shown clearly but deviate because of the DMA E' curve trends. Then, viscoelastic modeling is discussed and examined for one simulation. Also, velocity profiles of the Lamb wavefields in the x and z directions are scrutinized. Additionally, a new cure parameter called “gelation initiation” is proposed by analyzing the numerically generated voltage and velocity curves vs cure time results. Finally, degree of cure is integrated for both cure cycles from the velocity and voltage curves and compared numerically and experimentally. This model is a computational foundation to monitor the curing of several composites in the future. The cycle shortening is a major benefit to the industry and can be studied and applied on multiple composites with different cycles. More investigations are needed to improve the model and overcome some of the listed limitations present in the study.

CHAPTER 5

CURE MONITORING OF ADHESIVE FILMS AND COCURE MONITORING WITH CFRP LAMINATES

In this chapter, the curing of an adhesive film that's used for bonding purposes is monitored by joining two fully cured CFRP plates with a prepreg epoxy film to be cured in the oven. The same previous methods are used to analyse the data extracted from the ultrasound monitoring of this adhesive. Also, post-cure monitoring on the CFRP plates is performed to remove the effect of heat and determine more accurate cure parameters. DMA curing is then done on the epoxy film so that the results are implemented in the numerical model developed earlier. Sole A_0 mode is actuated numerically to enhance the scrutiny of mode conversion at the overlap. The numerical results, although heavily dependent on the DMA curing results input, still highlight the desired cure points. Finally, cocuring of both adhesive film and non-cured CFRP prepreg laminates is also tested experimentally at the end of this chapter where the amplitude curves show more sensitivity towards the added epoxy cure parameters.

5.1. Background

Since the used cure monitoring techniques have proved to be viable, they can now be used for other purposes. One of the growing trends in the aerospace and composites industries is the use of structural adhesive bonding. The main benefits of using such technique are elimination of drilled holes and thus micro-cracks and stress concentrations, weight reduction, and faster assemblies. [110] It is still, however, not extensively used in critical components of different structures as inspections may become exhaustive. This is why further structural health monitoring techniques are

being developed to monitor adhesive bonded joints. The ultrasonic non-destructive testing (NDT) techniques have been one of the most commonly used NDT techniques to evaluate bonding quality [111]. The ultrasonic NDT methods have been used not only to evaluate adherend integrity, but also for interface quality determination, debonding detection, and weak bond investigations [112].

Many studies focused on the use of ultrasonics to deduce the gel time of various epoxy adhesives. [113,114] Koissin et al. [115] used a nonlinear ultrasonic immersion technique to monitor the isothermal cure of an aluminum-adhesive-aluminum laminate. He describes this technique as the closest to DMA as both can capture minimum viscosity, gel onset, gel peak, and vitrification. Other techniques such as DSC and linear ultrasonics don't have the capacity to show some of these cure parameters, according to the authors. On the other hand, Yilmaz et al. [116] monitored defects and delamination in single lap joints made of the same laminate type using multiple ultrasonic techniques including bulk wave testing, air-coupled testing, and contact guided wave testing. The latter is more practical industrially but has a higher error percentage than the other testing methods.

Since adhesive bonding of two or more structures inherently derivates some overlap between them, some studies focused on the ultrasonic guided wave mode conversion occurring at these overlaps in-between structures. For example, Alkassar et al. [117] simulated the mode conversion numerically when the excited Lamb wave is passing through a defect present on a metallic plate. Wandowski et al. [118,119] analyzed the conversion of an S_0 mode to A_0 mode in glass fiber composites due to the inclusion of impact damages and artificial Teflon delamination.

To inspect this phenomenon, two plates which have the mechanical properties of fully cured woven CFRP (see Chapter 4) overlap on an adhesive layer of 2 cm width and are simulated in COMSOL where the actuator PZT is attached to the higher plate and sensor PZT to the lower one. Figure 5.1 compares both sole S_0 and sole A_0 excitations as read by the sensor. These actuations are done by adding a second actuator PZT on other side of the plate such that when the two actuators are polarized in the same way with the respect to the plate, only antisymmetric modes are actuated, and when they are polarized in reverse, only symmetric modes are actuated. Since the actuator and sensor are located at an equal distance from the overlap, the converted modes S_0A_0 and A_0S_0 reach the sensor at the same time. Thus, Figure 5.1 (b) compares the sum of these two actuated cases with the normal actuation of a single PZT, where it is notable that the difference between the two signals is minor, and the converted wave mode packets are comparable.

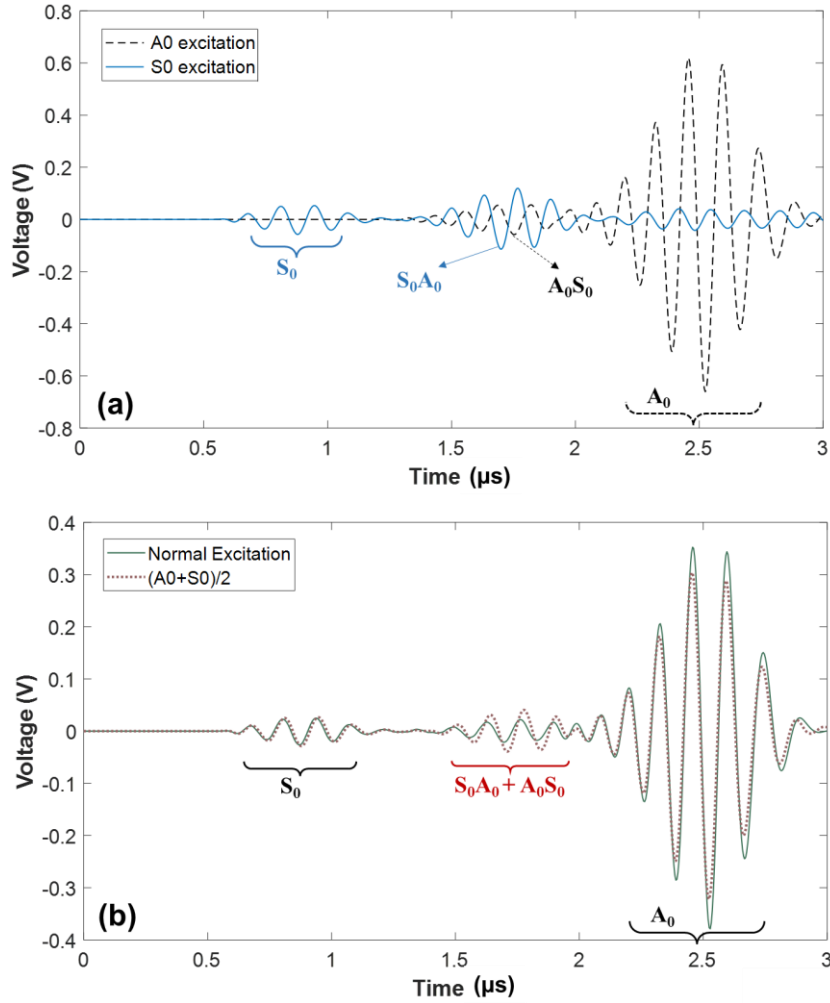


Figure 5.1: (a) Actuated and sensed signals by the inclusion of a second PZT actuator to transmit one mode only, either A_0 or S_0 . The mode conversion occurs in both cases. (b) Pristine sensed signal through actuated wave propagation vs the reconstructed signal by adding the two S_0 - and A_0 -actuated signals.

Figure 5.2 shows the y-direction velocity wavefields of the S_0 - and A_0 -solely actuated modes, respectively. These wavefields are essential in the analysis and inspection of any wave propagation experiment. The importance of the numerical or computational model lies in this wave scrutiny and obviously in lowering the consumables waste through experimental iterations. After optimizing the problem numerically and testing for the signal passing through the adhesive film at the overlap, the setup will be replicated experimentally. Also, for future work, it would be

interesting to see whether it is useful to actuate an A_0 mode only experimentally, since it might be less complex to analyse the signal that way.

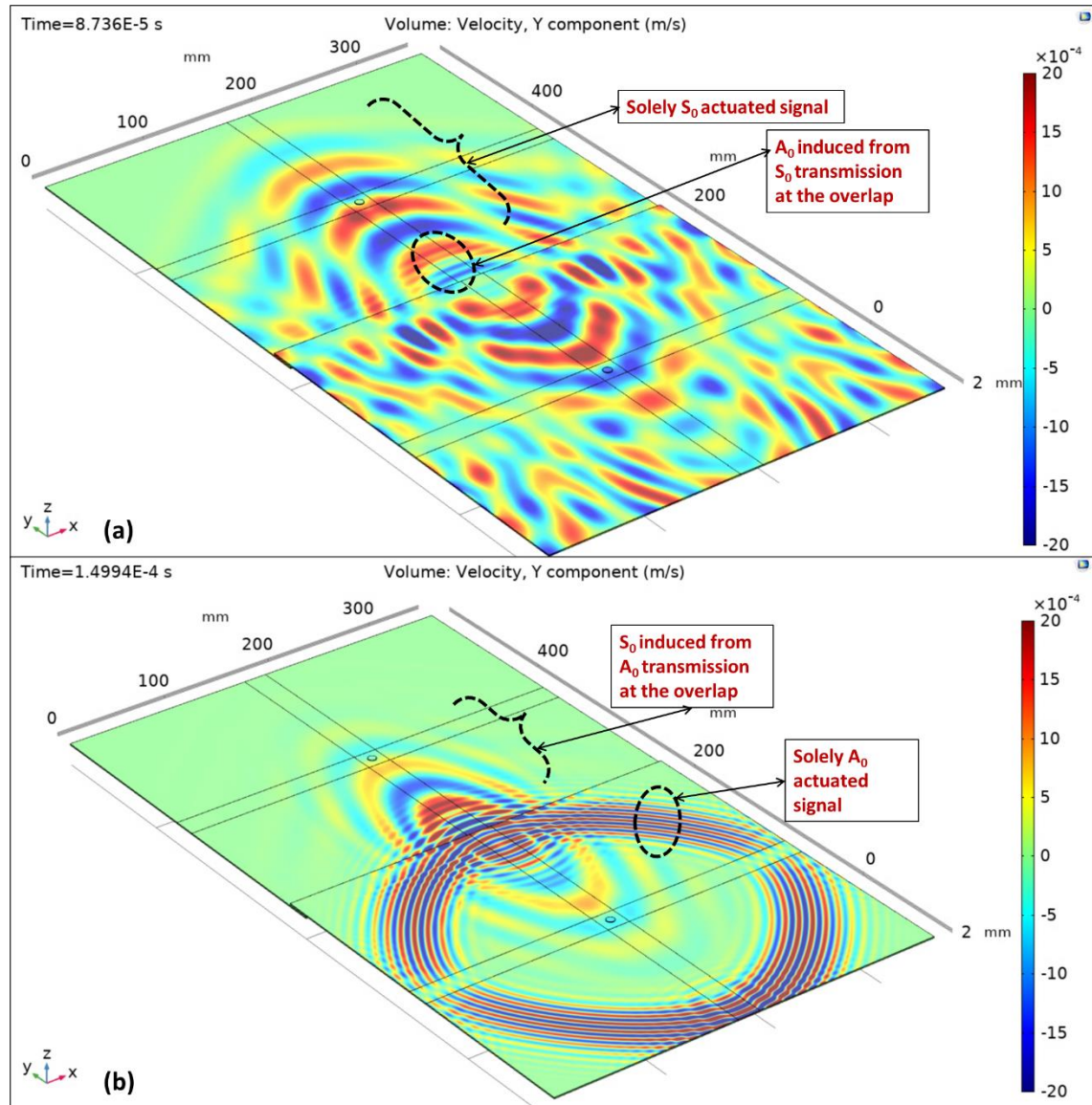


Figure 5.2: (a) Solely S_0 -actuated signal and (b) solely A_0 -actuated signal, seen by the y-direction velocities at two different times to emphasize on the mode conversion phenomenon in each case.

5.2. Experimental Adhesive Cure Monitoring

To test the prepreg adhesive film cure monitoring experimentally, seven layers of XPREG XA120 are stacked to form a thickness ≈ 1 mm. This epoxy film have planar dimensions of $350 \times 20 \text{ mm}^2$ and is layed-up in-between two overlapping $350 \times 320 \times 1 \text{ mm}^3$ XC110 woven CFRP plates that were previously cured. Figure 5.3 (a) shows this setup prior to the adhesion of the two plates together.

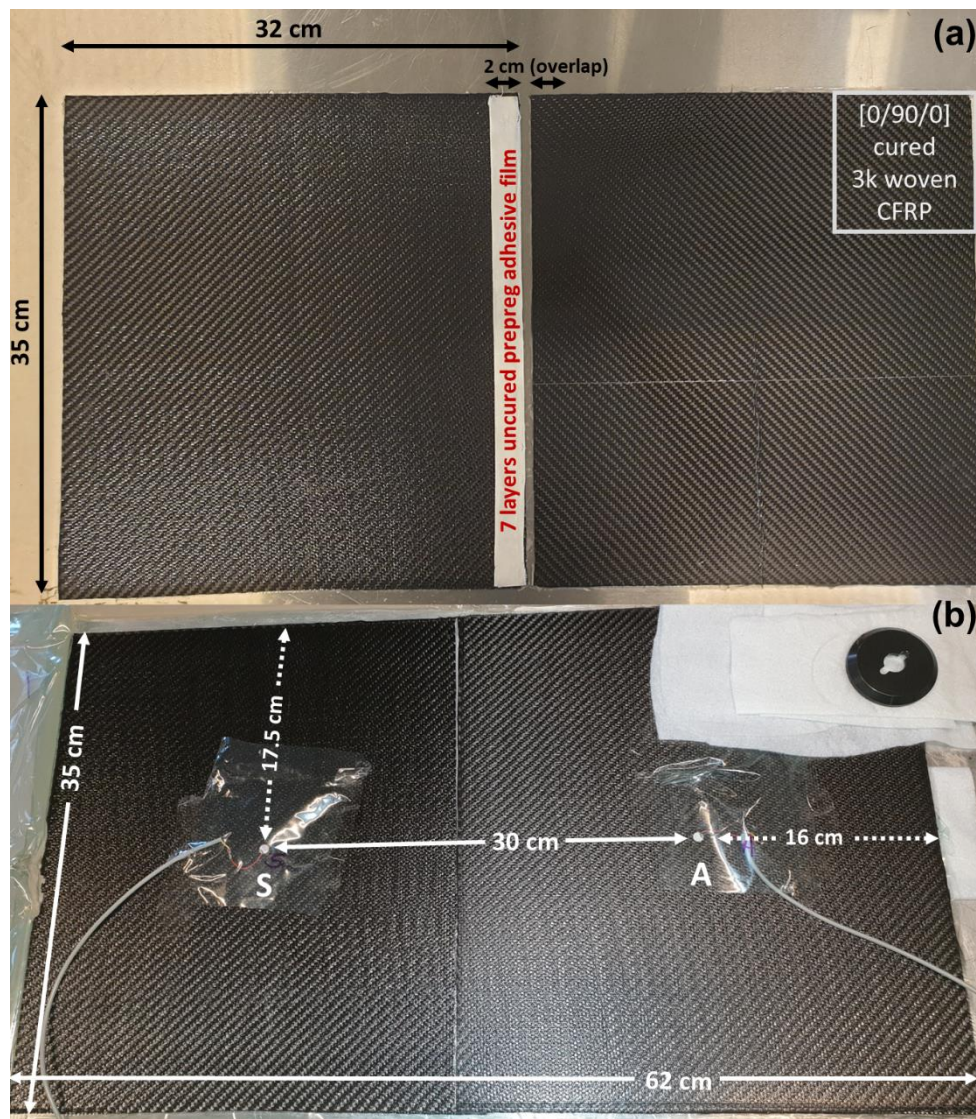


Figure 5.3: Experimental setup of the adhesive film cure monitoring (a) before the two fully cured woven CFRP plates are overlapped, and (b) after they are adhered to each other and the PZTs are installed. The setup is put under vacuum after these steps.

Figure 5.3 (b) shows the two plates adhered on the overlap and the two PZT transducers glued on top of the CFRP laminates. The actuator is on the higher plate and the distance between the latter and the sensor is 30 cm. The PZTs are directly glued to the CFRP because the latter is fully cured, and the previously fabricated sensing film would not adhere to it enough to actuate any signal even with the presence of vacuum.

The curing is done by ramping from room temperature up to 120°C with a heating rate of 3°C/min, soaking for one hour at the said temperature, then cooling naturally. Figure 5.4 shows the heat cycle recommended by the manufacturer for this type of epoxy adhesive. This data shows the operating oven temperature in five-minute interval as data is collected at this rate. The natural cooling is interrupted when the oven doors are open to fasten the cooling and end the cycle monitoring.

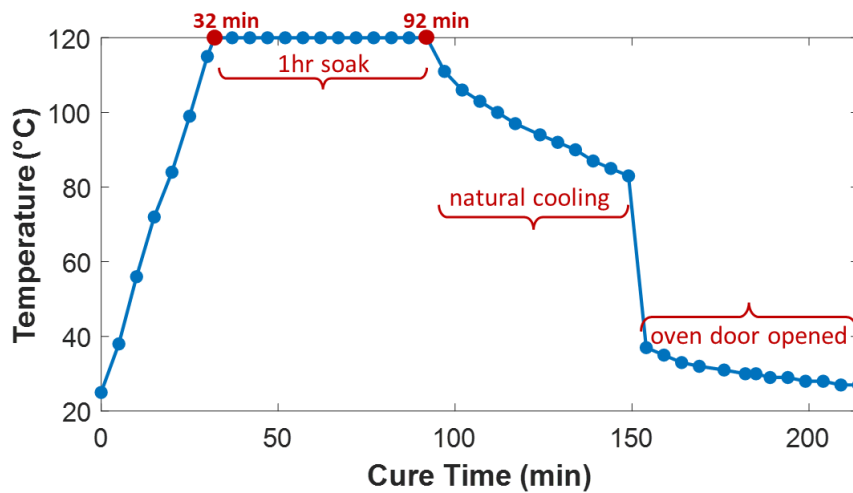


Figure 5.4: The cure cycle implemented for adhesive film curing. At 32 min, the oven temperature reaches 120°C, since the ramp starts at 25°C and the heat rate $\approx 3^\circ\text{C}/\text{min}$. Cooling data reaches 214 min but not all shown experiments in this section reach that much cooling time.

The data collected is analyzed, as seen in previous chapters, through the wave group velocity and amplitude. The frequency is always 70 kHz. This time, the analysis includes not only A_0 , but also S_0 and the combined converted mode $S_0A_0+A_0S_0$ which will be referred to as S_0A_0 for simplicity.

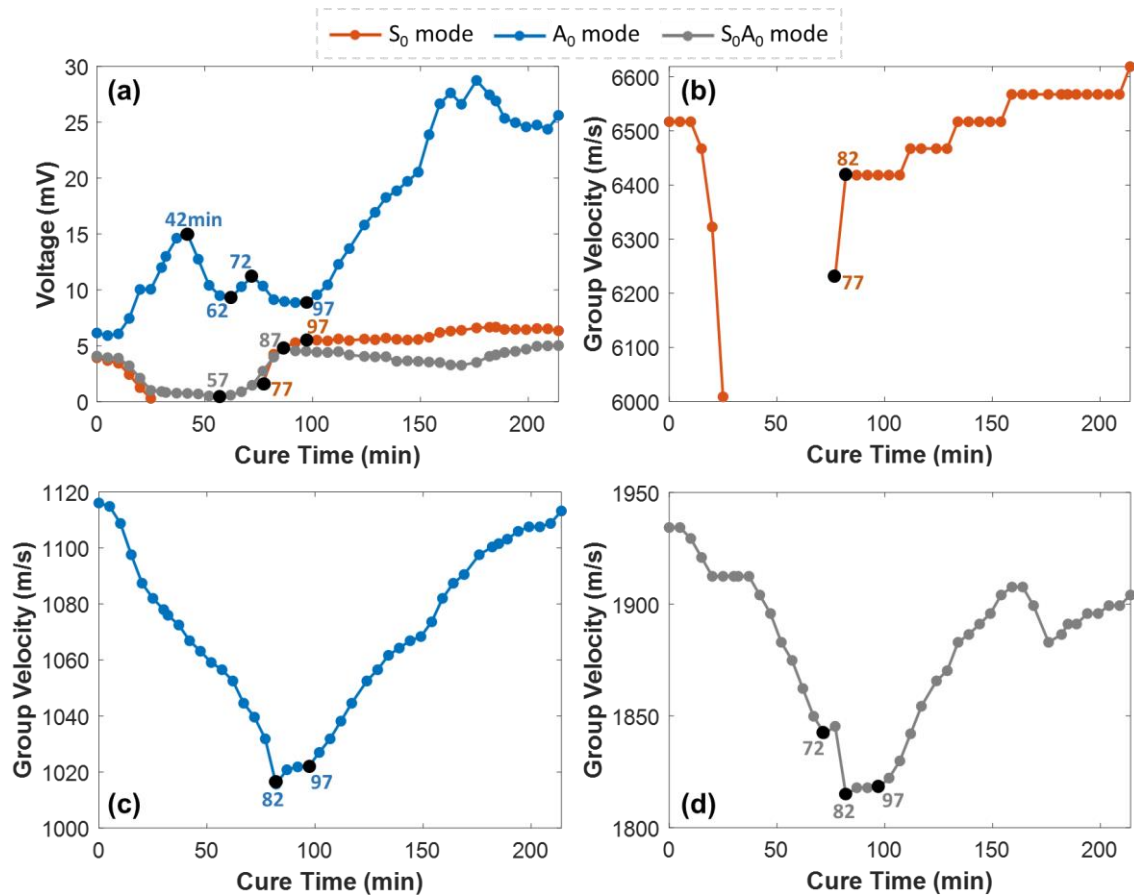


Figure 5.5: The adhesive film experimental cure monitoring results showing (a) the voltage curves for all three studied modes, and the group velocity curves vs cure time for (b) the S_0 mode, (c) the A_0 mode, and (d) the S_0A_0 mode. The minima, maxima, and onsets of interest are marked in black along with each specific time colored to its corresponding mode curve.

Figure 5.5 (a) shows the amplitude curves of the three analyzed modes. Points of interest are highlighted in black dots with corresponding times coloured to match their corresponding curve. The A_0 mode voltage rises to a maximum at 42 min then proceeds

to have one more maximum at 72 min and two minima at 62 min and 97 min. The latter also acts like an onset as the curve ascends to higher values during cooling and then shifts its slope around 150 min when the sudden temperature changes occur due to oven door opening. This is why anything beyond this latter point is neglected in all curves since it is just an indication of this temperature variation. The S_0 mode disappears during the ramp before reaching 120°C and then reappears at 77 min, 15 mins before the soak ends. Its reappearance could indicate a fully gelled adhesive. Its voltage curve shows the same 97 min onset. On the other hand, the S_0A_0 voltage curve follows a similar trend to that of S_0 except that the mode is visible throughout the cure. A minimum occurs at 57 min, before a quick rise and a slope change occurring at 87 min.

Figure 5.5 (b) shows the group velocity of S_0 having a similar trendline to its voltage counterpart. It reappears at 77 min but has the onset occurring at 82 min, which is why 82 min could be the vitrification point deduced from this curve (since, as seen in Chapter 2, vitrification is usually concluded from velocity curves). Figure 5.5 (c) shows the group velocity of A_0 mode that is going through the CFRP-adhesive-CFRP laminate. Its velocity descends to a minimum at 82 min before ascending to an onset at 97 min, and rapidly increasing in value until reaching similar values to its starting point. Figure 5.5 (d) shows a similar trend from the group velocity of S_0A_0 mode which has the same two minimum and onset at 82 min and 97 min, respectively. It also has an added minimum at 72 min. From these two latter velocity curves, one would first assume that the onset at 97 min can be vitrification, but since S_0 vitrifies at 82 min, and since it is known that at 97 min, the soak period is over and natural cooling has already started, then all onsets of 92 or 97 min from Figure 5.5 can be due to the effect of temperature changes in the already cured CFRP, and not because of phase changes in the curing

adhesive. The same can be said for other mentioned maxima and minima from the voltage curves, from which minimum viscosity and gelation points are usually extracted. Thus, the effect of temperature on the post-curing CFRP will be studied to remove any discrepancy from these curing parameters shown in this figure.

5.2.1. CFRP Post-cure Monitoring

To remove the temperature effect on the CFRP from the studied mode curves in Figure 5.5, an identical CFRP layup is cured without the use of adhesive film to do a post-cure study on it using the same temperature cure cycle as the one used for adhesive curing. Two PZTs were glued on the new fully cured CFRP laminate, separated by a distance of 20 cm. Figure 5.6 shows the voltage and group velocity curves for the studied S_0 and A_0 Lamb wave modes. Since there is no overlap in this case, the S_0A_0 mode is not present.

The group velocity curves in Figures 5.6 (c) and (d) have slightly different trendlines during post-cure heating since S_0 and A_0 propagate differently within the thin plate structure as mentioned in the previous chapters. S_0 propagates in-plane, thus influenced by the planar moduli of the laminate, while A_0 propagates out-of-plane, hence more guided by the z-axis moduli which are more related to the epoxy matrix component of the composite. They both, however, spring back towards their initial velocity value after cooling, with the velocity ramp starting from 97 min in both cases. This indicates that the previous assumption is real: the temperature variations effects on the CFRP are the ones influencing the 97 min onsets in the adhesive curing velocity curves in Figure 5.5.

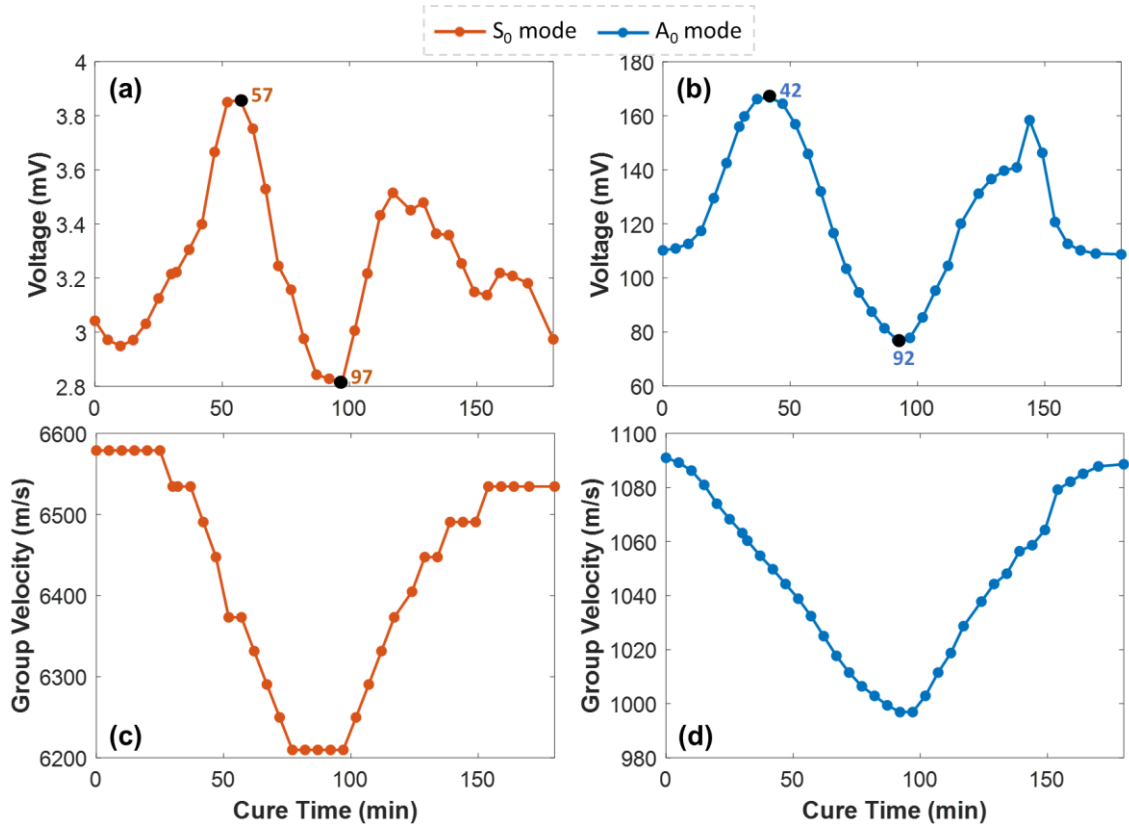


Figure 5.6: CFRP post-cure monitoring results showing the voltages curves for (a) S₀ and (b) A₀, and the velocity curves for (c) S₀ and (d) A₀.

Figure 5.6 (a) shows the voltage fluctuations of the S₀ mode during CFRP post-curing. The same 97 min onset is present as a minimum before the voltage increases back after cooling starts. However, a maximum at 57 min is also present indicating that the composite laminate has reached a temperature beyond its T_g and/or service temperature (as indicated by the manufacturer and discussed in Chapter 2). Figure 5.6 (b) shows the same thing for voltage curve of A₀ mode. The maximum, however, is at 42 min. These two points already have major influence on voltage curves of S₀A₀, and A₀ modes, respectively, in Figure 5.5 (a). As they are both minima in each respective curve.

5.2.2. Removal of CFRP Temperature Effect

After acquiring the CFRP post-curing thermal effects on voltage and velocity curves for both symmetric and anti-symmetric modes (Figure 5.6), their effect is respectively and proportionally removed from the voltage and velocity curves of S_0 and A_0 modes (Figure 5.5) such that S_0 mode voltage in Figure 5.6 (a) is proportionally deducted from the S_0 mode voltage in Figure 5.5 (a), and so on for A_0 voltage curve, S_0 velocity curve, and A_0 velocity curve. The results of this deduction are shown in Figure 5.7 below.

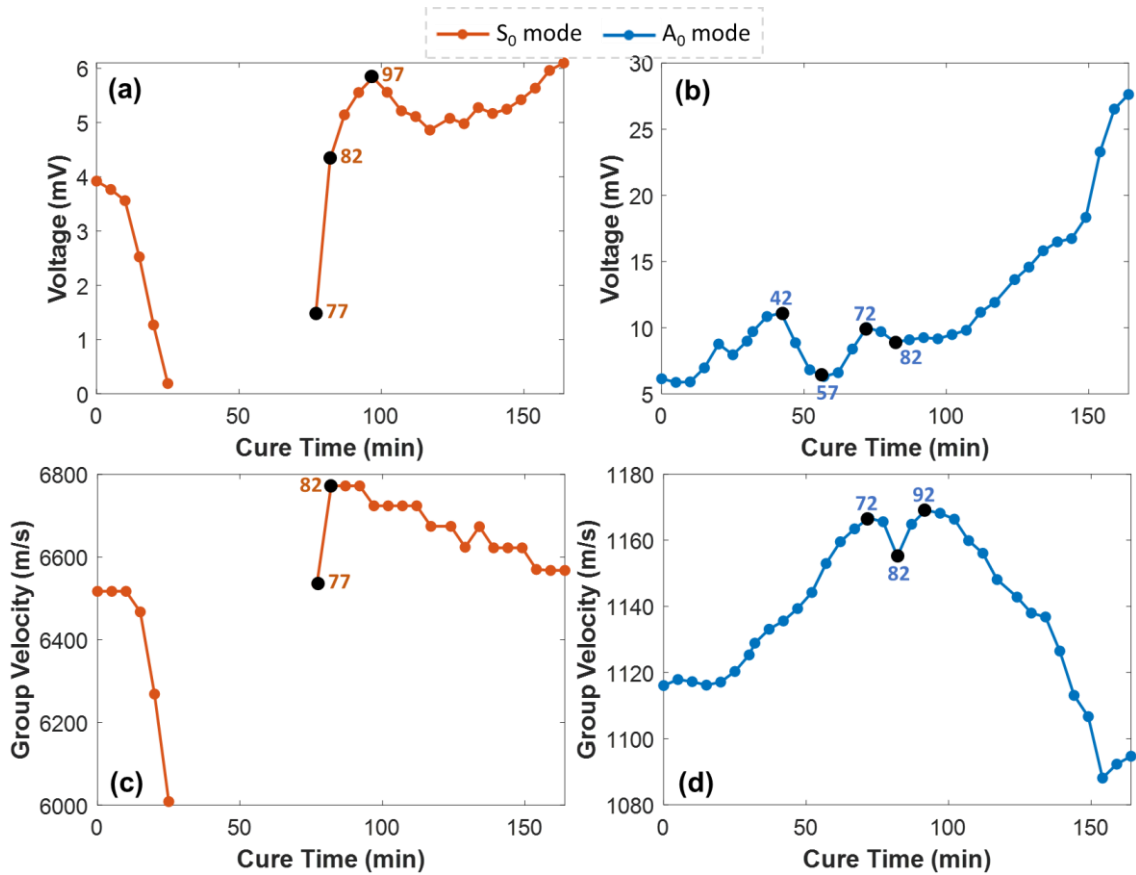


Figure 5.7: The adhesive film experimental cure monitoring results after proportionally deducting the thermal effect on CFRP post-curing from each curve, respectively. The figure shows the voltages curves for (a) S_0 and (b) A_0 , and the velocity curves for (c) S_0 and (d) A_0 . Since The S_0A_0 mode is not studied in the same post-curing CFRP fashion, its curves are not included in this figure.

Starting with S_0 , the trends of both velocity in Figure 5.7 (a) and voltage in Figure 5.7 (c) are intact. The mode curves descend until it disappears then reappear at 77 min where this is considered a fully gelled adhesive film. Then, vitrification occurs at 82 min from the velocity curve since an onset exists at that time. From the voltage curve, it is clear that the maximum at 97 min still exists so the effect of CFRP post-curing is still visible after the deduction. However, a slope change at 82 min in the same curve suggests that the previous conclusion is valid.

As for A_0 , Figure 5.7 (b) shows that the voltage curve still holds the points of interests after removal of CFRP post-curing effect. The maximum at 42 min which clearly shows in Figure 5.6 (b) still shows, so it might not be completely removed. However, the minimum at 62 min from Figure 5.5 (a) is now shifted to 57 min, which might suggest a minimum viscosity of the resin at this point. The maximum at 72 min is intact, which is clearly a gelation peak. Finally, the onset at 97 min from Figure 5.5 (a) is not very visible anymore and instead, a minimum/onset is present at 82 min. The latter time is of high interest in Figure 5.7 (d) where the velocity curve of this mode has a clear minimum at this point. This leads to concluding that the conclusions made from the S_0 curves are correct. In fact, the other two maxima sit at 72 min and 92 min, which are established by now as gelation peak, and CFRP post-cure effect, respectively.

From this section, a conclusion can be made that vitrification of the adhesive film occurs at 82 min (10 mins before soak period ends), this is deduced from the S_0 and A_0 velocity curves in Figure 5.7. Also, Figure 5.5 (d) shows the same point as a clear onset for S_0A_0 velocity curve, which is not even enhanced by removing the heat effect on CFRP. From the voltage curves in Figure 5.7, it is clear that minimum

viscosity, gelation peak, and full gelation occur at 57 min, 72 min, and 77 min, respectively. Out of these cure parameters, only minimum viscosity is deduced from the S_0A_0 voltage curve in Figure 5.5 (a), but this is also without CFRP heat effect removal. Thus, it is safe to say that analyzing A_0 mode alone is enough to get information about the cure kinetics of the adhesive prepreg film. However, the S_0 mode and the converted S_0A_0 mode add higher value to the cure parameters conclusions by confirming most of the parameters and adding a “full gelation” cure parameter to the findings.

One can argue that the converted mode replicates the trendline of S_0 in both voltage and velocity curves. This is why, in case of actuating a single A_0 mode, the analysis of the converted A_0S_0 mode should add enough information about the curing to be considered complete. The next section discusses replicating these findings in a numerical model.

5.3. Numerical Adhesive Cure Monitoring

5.3.1. Adhesive Film DMA Curing

DMA curing is performed on the adhesive film in order to have its Young’s modulus imported into the COMSOL model to replicate its experimental cure monitoring. Five different specimens of seven adhesive layers are stacked with a release film on each side and tested in the same cantilever setup used earlier in Chapter 3, using 1 Hz straining frequency. The results are shown in Figure 5.8 below.

Points of interest occur at 32 min, 52 min, and 92 min. The first and last are due to thermal changes: reaching soaking temperature and ending soaking period, respectively. Only slope change at 52 min occurs in between, possibly indicating gelation. The latter might occur this much faster in DMA than in the ultrasonic

experimental setup tested before (difference in 20 mins) due to heating reasons discussed in Chapter 3. However, The only other slope change prior to the cooling phase is at 92 min where the soaking period ends. It cannot be stated that this point is vitrification since there is a 40 mins time difference from the last discussed onset.

Since these storage modulus curves do not indicate cure parameters properly, perhaps a DSC experiment on the adhesive prepreg could give better results to compare with the ultrasonic measurement conclusions.

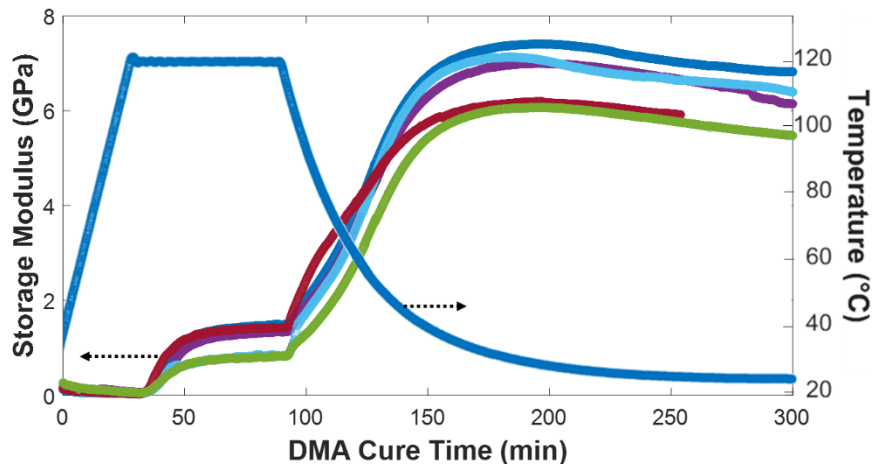


Figure 5.8: DMA curing temperature curve with natural cooling and storage modulus curve results of five tested adhesive film specimens.

5.3.2. Numerical Model Input and Results

To replicate the curing cycle in COMSOL, the DMA storage modulus results are averaged and imported as data with five-minute intervals. The averaged curve however, is divided by two since the modulus of epoxy would not reach 7 GPa as seen in Figure 5.8. In fact, tensile testing specimens are prepared from this material and tested to get an average Young's modulus of 3.4 GPa and an average tensile strength of 41.85 MPa. Figure 5.9 (a) shows the modulus curve that is imported into COMSOL for the adhesive

film material vs finite element cure time of the cycle. It reaches a maximum of 3.34 GPa after dividing the DMA averaged curve by two which is feasible compared to the stated tensile testing results.

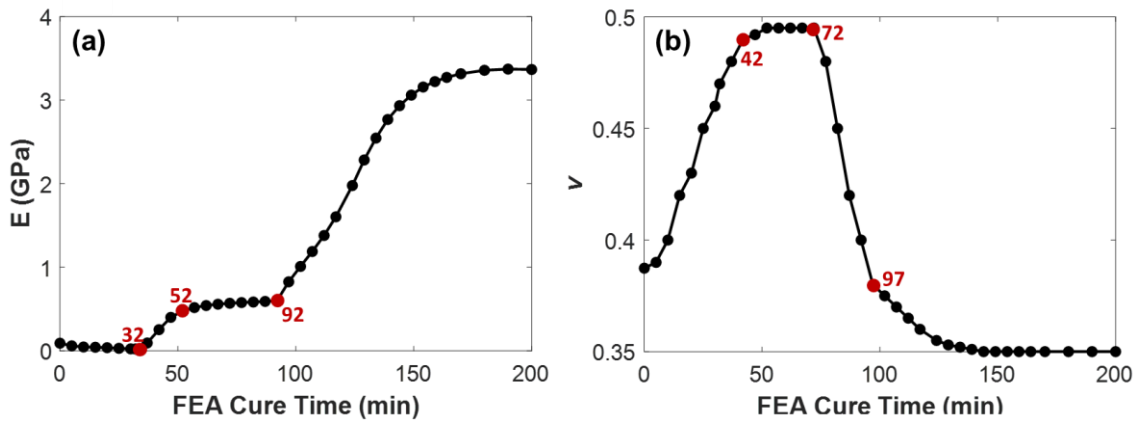


Figure 5.9: Imported material properties of the adhesive film into the numerical model where (a) shows the Young's modulus and (b) shows the Poisson's ratio, both vs the numerical cure time.

Figure 5.9 (b) shows the manually imported Poisson's ratio curve of adhesive film into the COMSOL model. Points of interest are at 42 min, 72 min, and 97 min. The first, from previous ultrasonic analysis, is most likely when the epoxy reaches the soaking temperature and becomes liquid. This is why it is approaching the value of 0.5 (incompressible liquid value) at this time. It continues to rise until 0.495 and then drops suddenly after 72 min where gelation occurs (also from ultrasonic experiment conclusions). After the epoxy is glassed beyond the vitrification point, the descending slope slows down at 97 min where the natural cooling affects the cured epoxy. Then, it slowly reaches a value of 0.35 after full cooldown.

Since the fully cured CFRP laminates' properties change during the adhesive film curing cycle, these changes must also be implemented in the numerical model to

reflect proper monitoring setup. These changes are proportional to the Lamb wave modes' amplitude and velocity, thus, the fully cured mechanical properties of CFRP from Chapter 4 are proportionally modified to resemble the changes from the previous CFRP post-cure analysis from Figure 5.6. Knowing that the antisymmetric and symmetric modes are affected by the out-of-plane and in-plane properties, respectively, and since the velocity changes due to heat are a derivatives of moduli changes [120], the S_0 mode velocity curve in Figure 5.6 (c) is implemented on moduli E_{11} , E_{22} , and G_{12} , and the A_0 mode velocity in Figure 5.6 (d) is implemented on moduli E_{33} , G_{13} , and G_{23} , with respect to each modulus' starting fully cured value. Also, the S_0 voltage curve in Figure 5.6 (a) is employed on the planar Poisson's ratio ν_{12} , while the out-of-plane ratios curves ν_{13} and ν_{23} are proportionally extracted from the A_0 voltage curve in Figure 5.6 (b). These model inputs are shown in Figure 5.10.

The numerical model is run with a parametric sweep with the same model settings seen in Chapter 4. The mesh maximum element size is set to 2 mm after trial and error findings that it covers the slowest studied mode A_0 in all cure data points. To capitalize on the first section discussions in this chapter, the numerical model is also set so that only A_0 mode is being actuated, and the analysis focuses on its velocity and voltage and those of the converted A_0S_0 mode from the overlap. This is to check whether is it feasible to eliminate a set of modes for more complex wave generation problems, and still be able to distinguish the same conclusions regarding cure parameters from analyzing the actuated set of modes and their converted counterparts. Numerical results are shown in Figure 5.11.

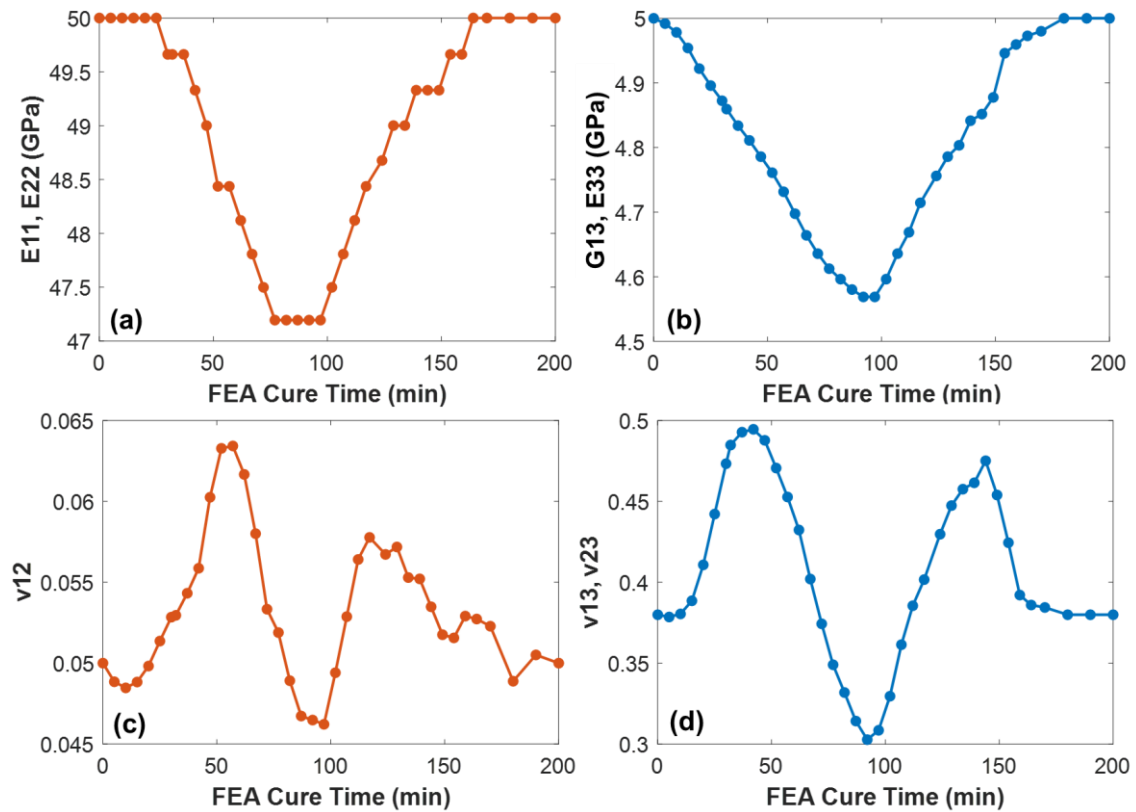


Figure 5.10: Imported material properties for the post-cured CFRP into the numerical model where (a) shows the E_{11} and E_{22} moduli, (b) shows the G_{13} and E_{33} moduli, (c) shows the v_{12} Poisson's ratio, and (d) shows the v_{13} and v_{23} ratios, all vs FEA cure time. Note that G_{12} follows the trend seen in (a) proportional to 7 GPa and G_{23} follows the trend seen in (b) proportional to 4 GPa.

The numerical curves do not resemble the ultrasonic experimental results mainly due to the inclusion of DMA modulus for the adhesive film. However, cure parameters derived from the shown points of interest are intact. In Figure 5.11, all curves include one or more of the following minima, maxima, and onsets: 32 min, 42 min, 92 min, and 97 min. The first and third times are inherited from the DMA imported properties as shown in Figure 5.9 (a), while the second and fourth times are inherited from the CFRP imported properties since 42 min and 97 min showed up heavily in those curves.

On the other hand, Figure 5.11 (a) which shows the A_0 voltage curve, clearly distinguishes the minimum viscosity at 57 min and gelation maximum at 72 min. Figure

5.11 (b), showing the A_0S_0 voltage curve, only shows the 57 min minimum, just like its experimental counterpart in S_0A_0 results. Both curves also have an 82 min minimum. Figures 5.11 (c) and 5.11 (d), which show the group velocity curves of each studied mode, both have the same vitrification onset at 82 min. Thus, all results deduced from the experimental study can be found here except for the 77 min full gelation point when the S_0 mode reappears experimentally. This is enough data to show again that the numerical model is valid and that this is a step closer towards a digital twin.

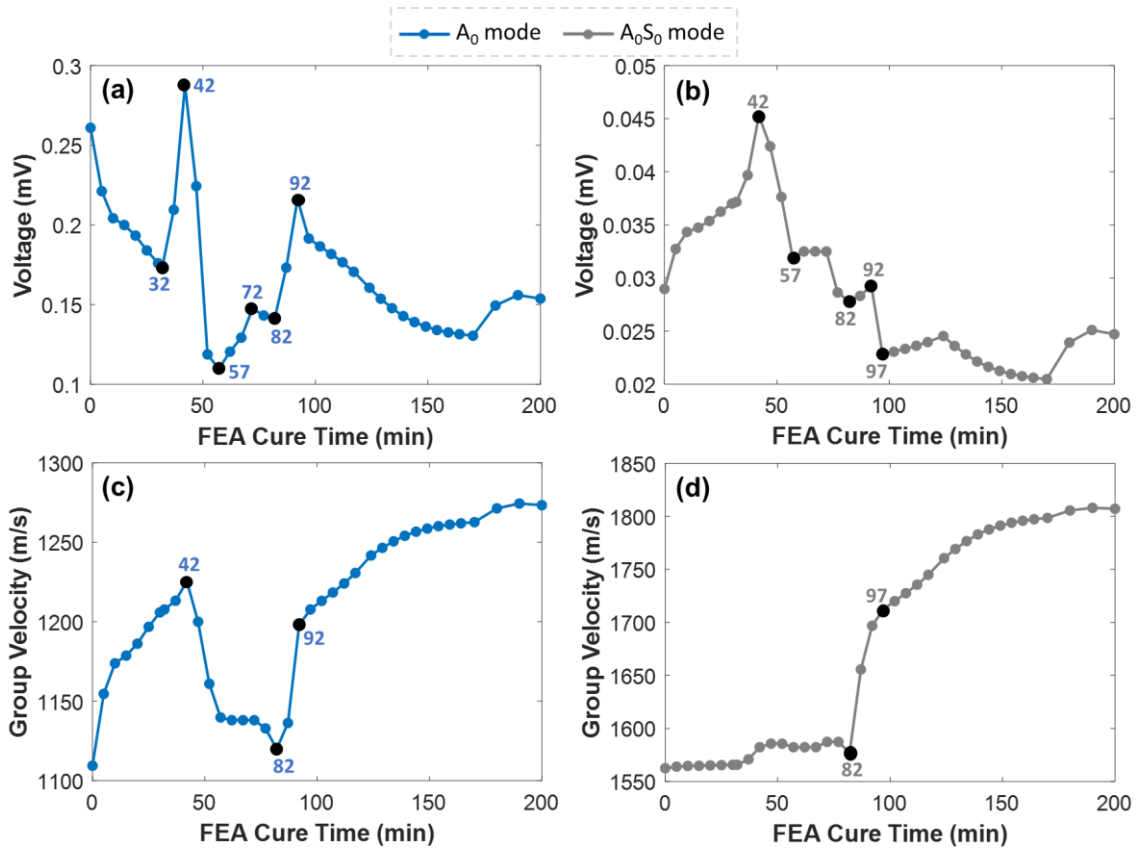


Figure 5.11: Numerical simulations results in the form of voltage curves for (a) A_0 mode and (b) A_0S_0 mode, and velocity curves for (c) A_0 mode and (d) A_0S_0 mode. The minima, maxima, and onsets of interest are marked in black along with each specific time colored to its corresponding mode curve.

5.4. Cocuring

Another important examination for the composites industry is the monitoring of cocured composites along with the adhesive bonding joint. To do so, two identical laminates to those discussed in Section 5.2 are laid-up and joint by the same 7-layers adhesive film at the 2 cm overlap. Since the woven CFRP is uncured, the reusable sensing film technology is used to cover the entire CFRP-adhesive-CFRP laminate during curing. The sensing film is made from two enclosed Skived PTFE sheets sandwiching two PZT transducers, similar to that discussed in Chapter 2 but with larger dimensions to cover the entire plate. The dimensions are shown in Figure 5.12 which includes the setup prior to applying vacuum.

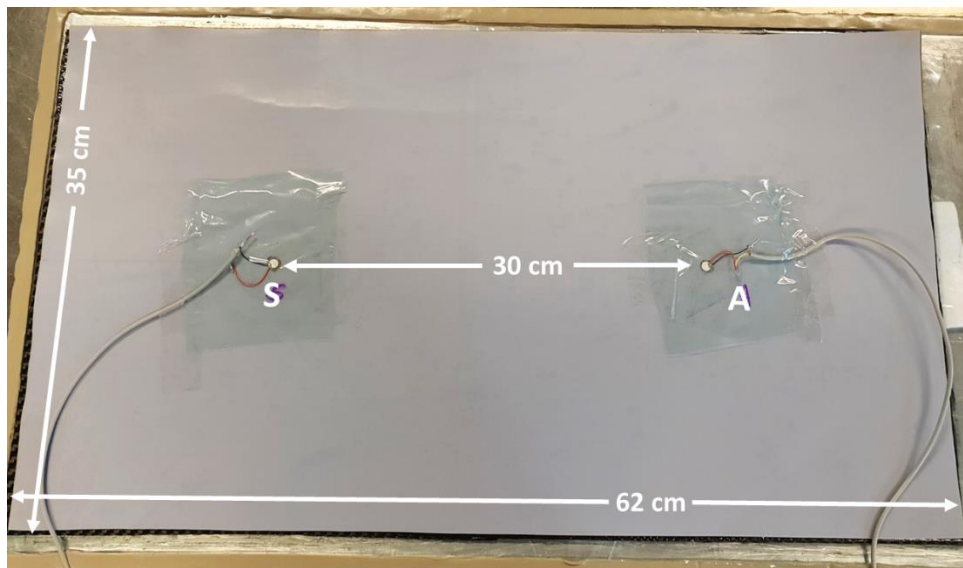


Figure 5.12: The cocuring experiment setup with the PTFE sensing film on top of the CFRP-adhesive-CFRP structure.

The curing cycle of the composite is followed since it already includes a one hour soak at 120°C similar to the curing cycle of the adhesive film. The difference is that the manufacturer recommends a 4hr-soak prior to that at 70°C, which is optimized

to a 3hr-soak in Chapter 3. Thus, the curing cycle, as seen in Figure 5.13, starts by ramping from room temperature to 70°C at a rate of 1°C/min before soaking at the said temperature for 3 hours. Then, a second ramp at a rate of 2°C/min is applied until reaching 120°C and holding for one more hour before cooling naturally. Figure 5.13 shows the curing cycle implemented for this experiment by displaying the oven temperature with data collected each five minutes.

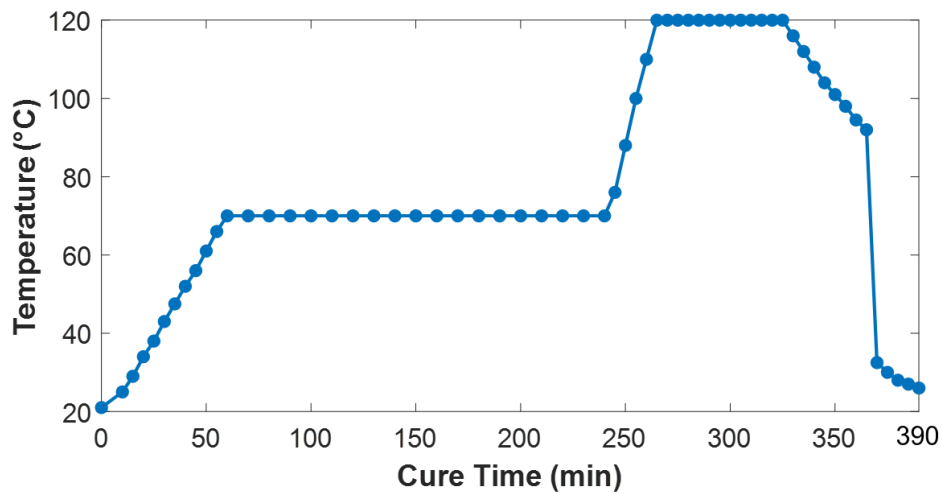


Figure 5.13: The cure cycle oven temperature data collected each five minutes vs cure time. A 10 mins threshold is maintained at the start to replicate the CFRP cure monitoring experiments in previous chapters. Thus, 70°C is reached at 60 min and its soak is done at 240 min, while 120°C is reached at 265 min and its soak is over at 325 min.

Again, the excited frequency is 70kHz and the actuator is set to have a constant amplitude of 160 Vpp. Due to vacuum, and similar to Chapter 2, the signal passes through the aluminum tooling plate making the A₀ wave mode faster in the region of 2300 m/s. This happens despite the fact that release films are placed at the bottom of the laminate separating the CFRP and the aluminum, unlike in Chapter 2 where only release agent was sprayed in-between the two. This is why the A₀ mode wave speed is lower

and not in the 2600 m/s range as seen in Figure 2.13. Nonetheless, the data collected and analyzed matches the cure of the CFRP plates. Results are shown in Figure 5.14.

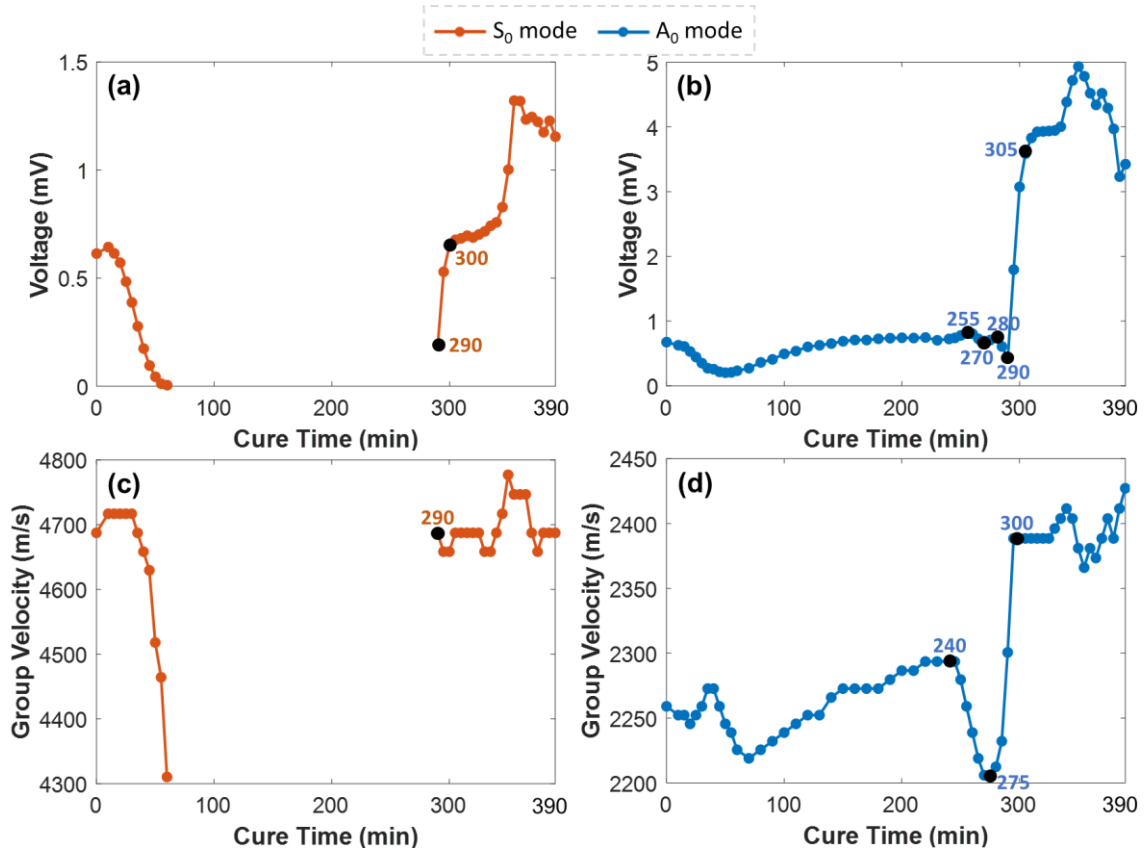


Figure 5.14: Cocuring results showing voltage and velocity curves for both S_0 and A_0 modes. The S_0A_0 mode is not as distinguishable as previously seen in the adhesive monitoring experiment because the antisymmetric mode is passing through the aluminum tooling plate and is faster than what S_0A_0 would be, thus it is not included in the analysis. Points of interest are marked in black.

Analyzing the results in Figure 5.14, the S_0 mode trends are very similar in velocity and voltage where a dip occurs during the first ramp and the mode disappears before reaching 70°C. The mode reappears at 290 min, 25 mins after the second soak period commences. This can be seen as a sign that both the composite and the adhesive film have fully gelled at this point, regardless which one reached gelation first. This

time is seen as an onset from the velocity curve in Figure 5.14 (c) while it is not the case in the voltage curve in Figure 5.14 (a) since the amplitude ascends to an onset at 300 min.

As for A_0 , the velocity curve in Figure 5.14 (d) replicates exactly that of Figure 2.15 (a) from the CFRP cure cycle monitoring in Chapter 2. The minimum viscosity at 240 min and the full gelation at 275 min are the same. The vitrification onset at 300 min is only 5 mins faster than that of 305 min in Figure 2.15 (a). Thus, the adhesive film curing does not impact the velocity of the transmitted A_0 mode. However, Figure 5.14 (b), showing the voltage curve of this mode, displays a set of maxima and minima that some are not seen in the sole CFRP cure monitoring experiment. Since gelation of CFRP is supposed to be at a minimum around 275 min according to Chapter 2, the 270 min minimum can be assumed to be full gelation point of the CFRP. Prior to that, the maximum shown at 255 min can be gel peak or gelation initiation as concluded from the end of Chapter 4. Since from S_0 mode considerations, the 290 min marks a fully gelled structure, then the 290 min minimum in this graph should be full gelation of the adhesive film. Prior to that, and similar to the CFRP gelation points, 280 min could mark a gel peak or gelation initiation point for the adhesive. The voltage then ascends swiftly and has an onset at 305 or 310 min. This can mark the onset vitrification of the adhesive film, which is not shown in the group velocity curve of A_0 but is clear and logical here since it follows the gelation point by not more than 15 mins, similar to the results of the adhesive cure monitoring in Section 5.2.

All in all, the cure parameters deduced can be, for CFRP: minimum viscosity at 240 min, gel peak at 255 min, full gelation at 270 min, and vitrification at 300 min, and for the adhesive film: gel peak at 280 min, full gelation at 290 min, and vitrification

ranging from 300 min to 310 min. The adhesive film parameters only show in the A_0 mode voltage curve and full gelation deduced from the reappearance of S_0 at this time. This cocuring experiment needs further exploration in the form of repeatability and perhaps numerical modeling, but nevertheless, it proves the viability to monitor the cocuring composite structures and adhesive joints by binding them together using a single in-situ experiment.

5.5. Summary

In this work, the curing of an adhesive prepreg film used for bonding purposes is monitored using the same ultrasound methods. By joining two fully cured CFRP plates with a prepreg epoxy film to be cured in the oven, the adhesive is monitored via guided Lamb waves passing through both the CFRP laminates and the epoxy. The same previous methods are used to analyse the data extracted from the S_0 and A_0 modes. The former disappears mid-cure and reappears again at full gelation of the adhesive film while the latter shows several cure parameters throughout its voltage and velocity curves. The converted mode S_0A_0 derived at the overlap is also analyzed and found to replicate the trend of S_0 without disappearing throughout the cure. To remove the thermal effects which are present on the CFRP plates during this adhesive cure and determine more accurate cure parameters, post-cure monitoring on a sole CFRP plate is performed before deducting this effect from the original adhesive monitoring curves. DMA curing is then done on the epoxy film so that the results are implemented in the numerical model developed in Chapter 4. Sole A_0 mode is actuated numerically to enhance the scrutiny of mode conversion at the overlap. The numerical results, although heavily dependent on the DMA curing inputs, still highlight the desired cure points

which consist of minimum viscosity, gel peak, full gelation, and vitrification. Finally, cocuring of both adhesive film and non-cured CFRP prepreg laminates is also tested experimentally where the A_0 amplitude curve show more sensitivity towards the added epoxy cure parameters, unlike the mode's velocity curve which replicates that of the sole CFRP cure monitoring. This chapter expands on the cure monitoring aspect while diving towards more complex problems.

CHAPTER 6

CONCLUSIONS AND FUTURE WORK

The composites industry is concerned with the manufacturing processes as they cannot provide fast enough cycle time to match metal alloy processes. This research aimed to develop a sensing technology in the form of a reusable in-situ cure monitoring and assessment system that can monitor the degree of cure of CFRPs through certain wave parameters. To study the feasibility of this monitoring process, a reusable flexible thin film of PTFE material was viably used to monitor the curing cycle of two composites: unidirectional and woven pre-impregnated CFRP laminates. First, the best material for the sensing film was chosen by eliminating candidates from both bonding and signal transmission experiments. Then, Skived PTFE was used as a sensing film by having sandwiched two disc shaped PZTs inside. Using this film, identification of important curing parameters such as gelation and vitrification points was done through the analysis of the group velocity and the voltage curves of the generated fundamental Lamb wave modes (mainly the dominant mode A_0 at the used 70 kHz frequency) with the help of the aluminum plate placed below the laminates creating a bond during curing that allowed the monitoring during the liquid phase to be easier. After proving its reliability in terms of cure cycle monitoring, the film was used to monitor the post-curing of the same laminates which are either bonded to the aluminum tooling plate, or loose. Further studies are still required to analyze the behavior of Lamb waves when PTFE layers are present on both sides of the composite plates separating it from the aluminum base plate. This system can also be used in future work to monitor in real-time any induced manufacturing defects within the manufactured part while curing.

In Chapter 3, the same flexible reusable Skived PTFE sensing film was effectively used to shorten the curing cycle time of a woven CFRP laminate by in-situ cure monitoring using Lamb waves at 70 kHz excitation. Three key cure parameters were looked at to determine the cure stages of the laminate and conclude that the cycle shortening was done successfully, all determined from the velocity and amplitude curves of the recorded A_0 mode: minimum viscosity, full gelation, and vitrification, all occurring after the first soak period which was cut by one hour. The new 3hr-soak curing cycle was then viably tested for Young's modulus and tensile strength by doing tensile testing on specimens that were cured at both cycles. The 3hr-soak cycle proved to have superiority in values of both these properties from averaging ten different specimens for each cycle. To further validate the new cycle enhancement, DMA testing was also used on both cycles in the single cantilever setup. DMA cure findings were similar to both conclusions, as the shift between the cure parameters were also averaged at 1 hour, and the final storage modulus recorded slightly higher values for the 3hr-soak cycles. Then, already cured specimens for both cycles were tested in the DMA machine for storage modulus and glass transition temperature. The findings proved better mechanical and thermal properties for the shortened cycle. Finally, DMA was used to test for static fatigue properties in both cycles. Already cured specimens were tested for creep at three temperature scans and the results showed similar performance for both cycles at 25 °C and 80 °C, and better performance for the shortened cycle at T_g of 135 °C. Thus, the viability of this cycle shortening was proved. More development can be made in future work to further optimize the curing cycle by cutting down more time from the soaking period and enhance the composites industry by making the manufacturing process faster and reducing waste. Also, different composites with

distinct curing cycles could be tested and optimized in the future, such as single-soak cure cycles which may be of more interest to the industry.

In Chapter 4, a numerical model for woven CFRP cure monitoring of a shortened curing cycle using guided Lamb waves was presented. First, the experimental ultrasonic results and conclusions were described such that the three main cure parameters: minimum viscosity, gelation, and vitrification were presented on the velocity and voltage curves. Then, DMA curing storage modulus results were extracted for both the original and a trimmed cycle by one hour and imported into COMSOL Multiphysics after segmenting data points each five minutes and amplifying the curve trends by a constant factor. All CFRP mechanical properties were taken as function of the E' trend, each with respect to their known final cured stage value. The numerical model was introduced by combining the solid mechanics and electrostatics physics in COMSOL. The geometry and mesh were described and the criteria for the time-dependent solver was defined. The results showed that the Lamb wave received signals match the experimental raw data especially in the studied region of the first received anti-symmetric mode. The concluded velocity and voltage curves were then compared to the experimental results as the cure parameters were shown clearly but deviate because of the DMA E' curve trends. Then, viscoelastic modeling was discussed and examined for one simulation. Also, velocity profiles of the Lamb wavefields in the x and z directions were scrutinized. Additionally, a new cure parameter called “gelation initiation” was proposed by analyzing the numerically generated voltage and velocity curves vs cure time results. This model is a computational foundation to monitor the curing of several composites in the future, and to eventually reach a digital twin model which facilitates the curing by reducing time and waste material. The cycle shortening

is a major benefit to the industry and can be studied and applied on multiple composites with different cycles. Finally, more investigations are needed to improve the model and overcome some of the listed limitations present in the study. For example, the loss modulus E'' and/or the $\tan \delta$ parameter are not considered for this study. They could slightly change the implemented modulus curve in COMSOL if employed. Also, density and relative permittivity of the woven CFRP are assumed to stay constant during the cure, which is not entirely accurate. Moreover, viscoelasticity is ignored because it needs more experimental testing and generates large numbers of degrees of freedom within the model. Further studies on the wavefield velocity profile is required to validate the claims about the slow CFRP A_0 mode at uncured stages. Finally, theoretical and experimental validations are needed to justify the statements about the new “gelation initiation” cure parameter.

Finally, the curing of an adhesive prepreg film used for bonding purposes was monitored using the same ultrasound methods. By joining two fully cured CFRP plates with a prepreg epoxy film to be cured in the oven, the adhesive was monitored via guided Lamb waves passing through both the CFRP laminates and the epoxy. The same previous methods were used to analyse the data extracted from the S_0 and A_0 modes. The former disappeared mid-cure and reappeared again at full gelation of the adhesive film while the latter showed several cure parameters throughout its voltage and velocity curves. The converted mode S_0A_0 derived at the overlap was also analyzed and found to replicate the trend of S_0 without disappearing throughout the cure. To remove the thermal effects which are present on the CFRP plates during this adhesive cure and determine more accurate cure parameters, post-cure monitoring on a sole CFRP plate was performed before deducting this effect from the original adhesive monitoring

curves. DMA curing was then performed on the epoxy film so that the results are implemented in the numerical model developed in Chapter 4. Sole A_0 mode was actuated numerically to enhance the scrutiny of mode conversion at the overlap. The numerical results, although heavily dependent on the DMA curing inputs, still highlighted the desired cure points which consist of minimum viscosity, gel peak, full gelation, and vitrification. Lastly, cocuring of both adhesive film and non-cured CFRP prepreg laminates was also tested experimentally where the A_0 amplitude curve show more sensitivity towards the added epoxy cure parameters, unlike the mode's velocity curve which replicates that of the sole CFRP cure monitoring. This work expanded on the cure monitoring aspect while diving towards more complex problems. However, future work may include some more refined traditional methods to fully understand the curing of the adhesive film, such as DSC. The numerical work can be upgraded by including better moduli representation, especially for the adhesive. In addition, the cocuring experiments need much more work to be established as a viable monitoring method.

REFERENCES

1. Holmes M (2019) Additive Manufacturing continues composites market growth. *Reinforced Plastics* 63(6): 296–301.
2. Mathes V (2018) The composites industry: Plenty of opportunities in heterogeneous market. *Reinforced Plastics* 62(1): 44–51.
3. Marsh G (2007) Airbus takes on Boeing with reinforced plastic A350 XWB. *Reinforced Plastics* 51(11): 26–29.
4. Jollivet T, Peyrac C and Lefebvre F (2013) Damage of composite materials. *Procedia Engineering* 66: 746–758.
5. Lindrose AM (1978) Ultrasonic wave and moduli changes in a curing epoxy resin. *Experimental Mechanics* 18(6): 227–232.
6. van Grootel A, Chang J, Wardle BL, et al. (2020) Manufacturing variability drives significant environmental and economic impact: The case of carbon fiber reinforced polymer composites in the aerospace industry. *Journal of Cleaner Production* 261: 121087.
7. Oromiehie E, Garbe U and Gangadhara Prusty B (2019) Porosity analysis of carbon fibre-reinforced polymer laminates manufactured using automated fibre placement. *Journal of Composite Materials* 54(9): 1217–1231.
8. Birt EA and Smith RA (2004) A review of NDE methods for porosity measurement in fibre-reinforced polymer composites. *Insight - Non-Destructive Testing and Condition Monitoring* 46(11): 681–686.
9. Bekas DG, Sharif-Khodaei Z and Aliabadi FM (2019) A smart multi-functional printed sensor for monitoring curing and damage of composite repair patch. *Smart Materials and Structures* 28(8): 085029.
10. Scheerer M, Simon Z, Marischler M, et al. (2017) A Multifunctional piezo and temperature sensor for process and structural health monitoring of CFRP structures made by resin transfer molding. In: 9th European workshop on structural health monitoring (EWSHM), Manchester, UK, 10–13 July 2018. Northhampton: BINDT.
11. Konstantopoulos S, Fauster E and Schledjewski R (2014) Monitoring the production of FRP Composites: A review of in-line sensing methods. *Express Polymer Letters* 8(11): 823–840.
12. Michel M and Ferrier E (2020) Effect of curing temperature conditions on glass transition temperature values of epoxy polymer used for wet lay-up applications. *Construction and Building Materials* 231: 117206.
13. Pang KP and Gillham JK (1990) Competition between cure and thermal degradation in a high TG epoxy system: Effect of time and temperature of isothermal cure on the glass transition temperature. *Journal of Applied Polymer Science* 39(4): 909–933.

14. Lange J, Altmann N, Kelly CT, et al. (2000) Understanding vitrification during cure of epoxy resins using dynamic scanning calorimetry and rheological techniques. *Polymer* 41(15): 5949–5955.
15. Nixdorf K and Busse G (2001) The dielectric properties of glass-fibre-reinforced epoxy resin during polymerisation. *Composites Science and Technology* 61(6): 889–894.
16. Stark W, Jaunich M and McHugh J (2015) Dynamic mechanical analysis (DMA) of epoxy carbon-fibre prepregs partially cured in a discontinued autoclave analogue process. *Polymer Testing* 41: 140–148.
17. Braun U, Balabanovich AI, Schartel B, et al. (2006) Influence of the oxidation state of phosphorus on the decomposition and fire behaviour of flame-retarded epoxy resin composites. *Polymer* 47(26): 8495–8508.
18. Sawicz-Kryniger K, Niezgodna P, Stalmach P, et al. (2022) Performance of FPT, FTIR and DSC methods in cure monitoring of epoxy resins. *European Polymer Journal* 162: 110933.
19. Kister G and Dossi E (2015) Cure monitoring of CFRP Composites by Dynamic Mechanical Analyser. *Polymer Testing* 47: 71–78.
20. Bilyeu B, Brostow W and Menard KP (2001) Evaluation of the curing process in a fiber-reinforced epoxy composite by temperature-modulated and step scan DSC and DMA. *Materials Characterization by Dynamic and Modulated Thermal Analytical Techniques*.
21. Hardis R, Jessop JLP, Peters FE, et al. (2013) Cure kinetics characterization and monitoring of an epoxy resin using DSC, Raman spectroscopy, and DEA. *Composites Part A: Applied Science and Manufacturing* 49: 100–108.
22. Kim HG and Lee DG (2002) Dielectric cure monitoring for glass/polyester prepreg composites. *Composite Structures* 57(1-4): 91–99.
23. Abraham D and McIlhagger R (1998) Glass fibre epoxy composite cure monitoring using parallel plate dielectric analysis in comparison with thermal and mechanical testing techniques. *Composites Part A: Applied Science and Manufacturing* 29(7): 811–819.
24. McIlhagger A, Brown D and Hill B (2000) The development of a dielectric system for the on-line cure monitoring of the resin transfer moulding process. *Composites Part A: Applied Science and Manufacturing* 31(12): 1373–1381.
25. Kahali Moghaddam M, Breede A, Chaloupka A, et al. (2016) Design, fabrication and embedding of microscale interdigital sensors for real-time cure monitoring during composite manufacturing. *Sensors and Actuators A: Physical* 243: 123–133.
26. Roberts SSJ and Davidson R (1993) Cure and fabrication monitoring of composite materials with fibre-optic sensors. *Composites Science and Technology* 49(3): 265–276.
27. García-Manrique JA, Marí B, Ribes-Greus A, et al. (2019) Study of the degree of cure through thermal analysis and Raman spectroscopy in composite-forming processes. *Materials* 12(23): 3991.

28. Wang D, Yu G, Liu S, et al. (2021) Monitoring the setting process of cementitious materials using guided waves in thin rods. *Materials* 14(3): 566.
29. Oral I, Guzel H and Ahmetli G (2012) Determining the mechanical properties of epoxy resin (DGEBA) composites by ultrasonic velocity measurement. *Journal of Applied Polymer Science* 127(3): 1667–1675.
30. Nawab Y, Casari P, Boyard N, et al. (2012) Characterization of the cure shrinkage, reaction kinetics, bulk modulus and thermal conductivity of thermoset resin from a single experiment. *Journal of Materials Science* 48(6): 2394–2403.
31. Yassene AA, Fares S, Ashour A, et al. (2017) Ultrasonic velocity and attenuation in epoxy resin/granite (marble) powder composite. *Research in Nondestructive Evaluation* 29(1): 48–60.
32. Aggelis DG and Paipetis AS (2012) Monitoring of resin curing and hardening by ultrasound. *Construction and Building Materials* 26(1): 755–760.
33. Maffezzoli A, Quarta E, Luprano VA, et al. (1999) Cure monitoring of epoxy matrices for composites by ultrasonic wave propagation. *Journal of Applied Polymer Science* 73(10): 1969–1977.
34. Dixon S, Jaques D, Palmer SB, et al. (2004) The measurement of shear and compression waves in curing epoxy adhesives using ultrasonic reflection and transmission techniques simultaneously. *Measurement Science and Technology* 15(5): 939–947.
35. Challis RE, Freemantle RJ, Cocker RP, et al. (2000) Ultrasonic measurements related to evolution of structure in curing epoxy resins. *Plastics, Rubber and Composites* 29(3): 109–118.
36. Pavlopoulou S, Soutis C and Staszewski WJ (2012) Cure monitoring through time–frequency analysis of guided ultrasonic waves. *Plastics, Rubber and Composites* 41(4-5): 180–186.
37. Lionetto F and Maffezzoli A (2013) Monitoring the cure state of thermosetting resins by ultrasound. *Materials* 6(9): 3783–3804.
38. Hudson TB and Yuan F-G (2018) Automated in-process cure monitoring of composite laminates using a guided wave-based system with high-temperature piezoelectric transducers. *Journal of Nondestructive Evaluation, Diagnostics and Prognostics of Engineering Systems* 1(2).
39. Mizukami K, Ikeda T and Ogi K (2019) Measurement of velocity and attenuation of ultrasonic guided wave for real-time estimation of cure-dependent anisotropic viscoelastic properties of carbon fiber-reinforced plastics. *Ultrasonics* 99: 105952.
40. Mizukami K, Ikeda T and Ogi K (2020) Ultrasonic guided wave technique for monitoring cure-dependent viscoelastic properties of carbon fiber composites with toughened interlaminar layers. *Advanced Composite Materials* 30(sup2): 85–105.
41. Liu X, Li J, Zhu J, et al. (2021) Cure monitoring and damage identification of CFRP using embedded Piezoelectric Sensors Network. *Ultrasonics* 115: 106470.
42. Sun F, Liao DM, Zhang ZC, et al. (2015) Simulation analysis of resin-based composites on temperature and degree of cure fields by thermoforming process

considering the influence of temperature distribution inside the Autoclave. *Materials Research Innovations* 19(sup5).

43. Aktas A, Krishnan L, Kandola B, et al. (2014) A cure modelling study of an unsaturated polyester resin system for the simulation of curing of fibre-reinforced composites during the vacuum infusion process. *Journal of Composite Materials* 49(20): 2529–2540.
44. Anandan S, Dhaliwal GS, Huo Z, et al. (2017) Curing of thick thermoset composite laminates: Multiphysics Modeling and experiments. *Applied Composite Materials* 25(5): 1155–1168.
45. Garschke C, Parlevliet PP, Weimer C, et al. (2013) Cure kinetics and viscosity modelling of a high-performance epoxy resin film. *Polymer Testing* 32(1): 150–157.
46. Behzad T and Sain M (2007) Finite element modeling of polymer curing in natural fiber reinforced composites. *Composites Science and Technology* 67(7-8): 1666–1673.
47. Nakouzi S, Pancrace J, Schmidt FM, et al. (2010) Curing simulation of composites coupled with infrared heating. *International Journal of Material Forming* 3(S1): 587–590.
48. Shi F and Dong X-H (2010) Numerical Study of Resin Transfer Molding (RTM) curing process. *Frontiers of Materials Science in China* 4(2): 217–224.
49. Dai J, Xi S and Li D (2019) Numerical analysis of curing residual stress and deformation in thermosetting composite laminates with comparison between different constitutive models. *Materials* 12(4): 572.
50. Zheng, Z., and Zhang, R. (2014) Implementation of a Viscoelastic Material Model to Simulate Relaxation in Glass Transition. In: COMSOL Conference Proceedings, Boston, USA.
51. Patham B (2012) Multiphysics simulations of cure residual stresses and springback in a thermoset resin using a viscoelastic model with cure-temperature-time superposition. *Journal of Applied Polymer Science* 129(3): 983–998.
52. Yoo S-H, Han M-G, Hong J-H, et al. (2015) Simulation of curing process of carbon/epoxy composite during autoclave degassing molding by considering phase changes of epoxy resin. *Composites Part B: Engineering* 77: 257–267.
53. Kravchenko OG, Kravchenko SG, Casares A, et al. (2015) Digital Image Correlation Measurement of resin chemical and thermal shrinkage after gelation. *Journal of Materials Science* 50(15): 5244–5252.
54. Liu L, Zhang B-M, Wang D-F, et al. (2006) Effects of cure cycles on void content and mechanical properties of composite laminates. *Composite Structures* 73(3): 303–309.
55. Pantelelis N, Vrouvakis T and Spentzas K (2003) Cure cycle design for composite materials using computer simulation and optimisation tools. *Forschung im Ingenieurwesen* 67(6): 254–262.

56. Dong A, Zhao Y, Zhao X, et al. (2018) Cure cycle optimization of rapidly cured out-of-autoclave composites. *Materials* 11(3): 421.
57. Costa ML, Botelho EC, Paiva JM, et al. (2005) Characterization of cure of carbon/epoxy prepreg used in aerospace field. *Materials Research* 8(3): 317–322.
58. Hernández S, Sket F, González C, et al. (2013) Optimization of curing cycle in carbon fiber-reinforced laminates: Void Distribution and mechanical properties. *Composites Science and Technology* 85: 73–82.
59. Hwang S-S, Park SY, Kwon G-C, et al. (2018) Cure kinetics and viscosity modeling for the optimization of cure cycles in a vacuum-bag-only prepreg process. *The International Journal of Advanced Manufacturing Technology* 99(9-12): 2743–2753.
60. Hamdan B, Lafi S and Hassan NM (2017) Optimizing the manufacturing processes of carbon fiber epoxy resin composite panels. *Journal of Manufacturing Science and Engineering* 140(1).
61. Frick A, Sich D, Heinrich G, et al. (2012) Relationship between structure and mechanical properties of melt processable PTFE: Influence of molecular weight and comonomer content. *Macromolecular Materials and Engineering* 298(9): 954–966.
62. Pernice MF, De Carvalho NV, Ratcliffe JG, et al. (2015) Experimental study on delamination migration in composite laminates. *Composites Part A: Applied Science and Manufacturing* 73: 20–34.
63. Le Cahain YM, Noden J and Hallett SR (2014) Effect of insert material on artificial delamination performance in composite laminates. *Journal of Composite Materials* 49(21): 2589–2597.
64. Deng X (1995) Mechanics of debonding and delamination in composites: Asymptotic studies. *Composites Engineering* 5(10-11): 1299–1315.
65. Vail JR, Krick BA, Marchman KR, et al. (2011) Polytetrafluoroethylene (PTFE) fiber reinforced polyetheretherketone (peek) composites. *Wear* 270(11-12): 737–741.
66. Vogelsang R, Brutsch R, Farr T, et al. (2002) Electrical tree propagation along barrier-interfaces in epoxy resin. In: Annual Report Conference on Electrical Insulation and Dielectric Phenomena, Cancun, Quintana Roo, Mexico, October 2002.
67. Coulson SR, Woodward I, Badyal JP, et al. (2000) Super-repellent composite fluoropolymer surfaces. *The Journal of Physical Chemistry B* 104(37): 8836–8840.
68. Lamb H (1917) On waves in an elastic plate. *Proceedings of the Royal Society of London. Series A, Containing Papers of a Mathematical and Physical Character* 93(648): 114–128.
69. Wang L and Yuan F (2007) Group velocity and characteristic wave curves of lamb waves in composites: Modeling and experiments. *Composites Science and Technology* 67(7-8): 1370–1384.
70. Moulin E, Assaad J, Delebarre C, et al. (2000) Modeling of lamb waves generated by integrated transducers in composite plates using a coupled finite element–

- normal modes expansion method. *The Journal of the Acoustical Society of America* 107(1): 87–94.
71. Vázquez S, Gosálbez J, Bosch I, et al. (2019) Comparative study of coupling techniques in lamb wave testing of metallic and cementitious plates. *Sensors* 19(19): 4068.
 72. El Najjar J and Mustapha S (2021) Condition assessment of timber utility poles using ultrasonic guided waves. *Construction and Building Materials* 272: 121902.
 73. Su Z, Ye L and Lu Y (2006) Guided lamb waves for identification of damage in composite structures: A Review. *Journal of Sound and Vibration* 295(3-5): 753–780.
 74. Harb MS and Yuan FG (2015) Lamb wave dispersion and anisotropy profiling of composite plates via non-contact air-coupled and laser ultrasound. *AIP Conference Proceedings*.
 75. Harb MS and Yuan FG (2016) Non-contact ultrasonic technique for lamb wave characterization in composite plates. *Ultrasonics* 64: 162–169.
 76. Harb MS and Yuan F-G (2018) Air-coupled nondestructive evaluation dissected. *Journal of Nondestructive Evaluation* 37(3).
 77. Harb MS and Yuan FG (2016) Barely visible impact damage imaging using non-contact air-coupled transducer/laser Doppler vibrometer system. *Structural Health Monitoring* 16(6): 663–673.
 78. Mustapha S, Ye L, Wang D, et al. (2011) Assessment of debonding in Sandwich cf/ep composite beams using A0 lamb wave at low frequency. *Composite Structures* 93(2): 483–491.
 79. Okabe Y, Fujibayashi K, Shimazaki M, et al. (2010) Delamination detection in composite laminates using dispersion change based on mode conversion of Lamb Waves. *Smart Materials and Structures* 19(11): 115013.
 80. Mehrabi M and Soorgee MH (2019) The use of ultrasonic guided waves in cure monitoring of adhesives. In: The 9th international conference on acoustics and vibrations, 24–25 December 2019. Tehran: ISAV.
 81. Fakh MA, Tarraf J, Mustapha S, et al. (2017) Characterization of Lamb waves propagation behavior in friction stir welded joints of dissimilar materials. In: The 11th international workshop on structural health monitoring (IWSHM), Stanford, California, 12–14 September 2017. Pennsylvania: DEStech Publications.
 82. Tarraf J, Mustapha S, Fakh MA, et al. (2018) Application of ultrasonic waves towards the inspection of similar and dissimilar friction stir welded joints. *Journal of Materials Processing Technology* 255: 570–583.
 83. Ismail Z, Mustapha S, Fakh MA, et al. (2019) Sensor placement optimization on complex and large metallic and composite structures. *Structural Health Monitoring* 19(1): 262–280.

84. Attar L, Leduc D, Ech Cherif El Kettani M, et al. (2020) Detection of the degraded interface in dissymmetrical glued structures using Lamb Waves. *NDT & E International* 111: 102213.
85. Dodson JC and Inman DJ (2013) Thermal sensitivity of lamb waves for structural health monitoring applications. *Ultrasonics* 53(3): 677–685.
86. Feng B, Ribeiro AL and Ramos HG (2018) Interaction of lamb waves with the edges of a delamination in CFRP composites and a reference-free localization method for delamination. *Measurement* 122: 424–431.
87. Malaeb RA, Mahfoud EN and Harb MS (2018) Decomposition of fundamental Lamb wave modes in complex metal structures using COMSOL®. In: COMSOL conference proceedings, Lausanne, Switzerland, October 2018. Stockholm: COMSOL.
88. Giurgiutiu V (2005) Tuned lamb wave excitation and detection with piezoelectric wafer active sensors for Structural Health Monitoring. *Journal of Intelligent Material Systems and Structures* 16(4): 291–305.
89. Gerlich D and Fisher ES (1969) The high temperature elastic moduli of aluminum. *Journal of Physics and Chemistry of Solids* 30(5): 1197–1205.
90. Prime RB (1970) Dynamic cure analysis of thermosetting polymers. *Analytical Calorimetry*: 201–210.
91. Wang J, GangaRao H, Liang R, et al. (2015) Durability and prediction models of fiber-reinforced polymer composites under various environmental conditions: A critical review. *Journal of Reinforced Plastics and Composites* 35(3): 179–211.
92. ASTM International (2017) ASTM D 3039/3039M-17: standard test method for tensile properties of polymer matrix composite materials. In: Annual book of ASTM standards. West Conshohocken, PA, American Society for Testing and Materials.
93. Ray BC and Rathore D (2014) Durability and integrity studies of environmentally conditioned interfaces in fibrous polymeric composites: Critical concepts and comments. *Advances in Colloid and Interface Science* 209: 68–83.
94. Stark W (2013) Investigation of the curing behaviour of carbon fibre epoxy prepreg by dynamic mechanical analysis DMA. *Polymer Testing* 32(2): 231–239.
95. Pedrazzoli D, Dorigato A and Pegoretti A (2012) Monitoring the mechanical behavior under ramp and creep conditions of electrically conductive polymer composites. *Composites Part A: Applied Science and Manufacturing* 43(8): 1285–1292.
96. Chang F-C, Lam F and Kadla JF (2014) The effect of temperature on creep behavior of wood-plastic composites. *Journal of Reinforced Plastics and Composites* 33(9): 883–892.
97. PTFE products and solutions for various industries: Materials: Polyflor (n.d.) Home. Available from: <https://www.polyflor.nl/en/materials/ptfe/> (accessed 12 May 2022).

98. Balzano A, De Rosa IM, Sarasini F, et al. (2007) Effective properties of carbon fiber composites: EM modeling versus experimental testing. *2007 IEEE International Symposium on Electromagnetic Compatibility*.
99. Eddib AA and Chung DDL (2019) Electric permittivity of carbon fiber. *Carbon* 143: 475–480.
100. Saseendran S, Wysocki M and Varna J (2016) Evolution of viscoelastic behavior of a curing ly5052 epoxy resin in the glassy state. *Advanced Manufacturing: Polymer & Composites Science* 2(2): 74–82.
101. O'Brien DJ, Sottos NR and White SR (2007) Cure-dependent viscoelastic Poisson's ratio of epoxy. *Experimental Mechanics* 47(2): 237–249.
102. O'Brien DJ, Mather PT and White SR (2001) Viscoelastic properties of an epoxy resin during cure. *Journal of Composite Materials* 35(10): 883–904.
103. Grassia L and D'Amore A (2009) The relative placement of linear viscoelastic functions in amorphous glassy polymers. *Journal of Rheology* 53(2): 339–356.
104. Ghose, B., Balasubramaniam, K., Krishnamurthy, C. V., and Rao, A. S. (2010) Two dimensional FEM simulation of ultrasonic wave propagation in isotropic Solid Media using COMSOL. In: COMSOL Conference Proceedings, Bangalore, India.
105. Schenk O (2003) Solving unsymmetric sparse systems of linear equations with Pardiso. *Future Generation Computer Systems*.
106. Brugnano L and Magherini C (2008) Blended general linear methods based on generalized BDF. *AIP Conference Proceedings*.
107. Eom Y, Boogh L, Michaud V, et al. (2000) Time-cure-temperature superposition for the prediction of instantaneous viscoelastic properties during cure. *Polymer Engineering & Science* 40(6): 1281–1292.
108. Brauner C, Frerich T and Herrmann AS (2016) Cure-dependent thermomechanical modelling of the stress relaxation behaviour of composite materials during manufacturing. *Journal of Composite Materials* 51(7): 877–898.
109. Ornaghi HL, Almeida JH, Monticeli FM, et al. (2020) Stress relaxation, creep, and recovery of carbon fiber non-crimp fabric composites. *Composites Part C: Open Access* 3: 100051.
110. Tornow C, Schlag M, Lima LC, et al. (2015) Quality assurance concepts for adhesive bonding of composite aircraft structures – characterisation of adherent surfaces by extended NDT. *Journal of Adhesion Science and Technology* 29(21): 2281–2294.
111. Asif M, Khan MA, Khan SZ, et al. (2018) Identification of an effective nondestructive technique for bond defect determination in laminate composites—a technical review. *Journal of Composite Materials* 52(26): 3589–3599.
112. Yilmaz B, Ba A, Jasiuniene E, et al. (2019) Comparison of different non-destructive testing techniques for bonding quality evaluation. *2019 IEEE 5th International Workshop on Metrology for Aerospace (MetroAeroSpace)*.

113. Bacri JC, Courdille JM, Dumas J, et al. (1980) Ultrasonic waves: A tool for gelation process measurements. *The Journal of Physical Chemistry Letters* 41(15):369–72.
114. White SR, Mather PT and Smith MJ (2002) Characterization of the cure-state of DGEBA- DDS epoxy using ultrasonic, dynamic mechanical, and thermal probes. *Polym Eng Sci* 42(1):51–67.
115. Koissin V, Demčenko A and Korneev VA (2014) Isothermal epoxy-cure monitoring using nonlinear ultrasonics. *International Journal of Adhesion and Adhesives* 52:11–18.
116. Yilmaz A, Asokkumar A, Jasiūnienė E, et al. (2020) Air-coupled, contact, and immersion ultrasonic non-destructive testing: Comparison for bonding quality evaluation. *Applied Sciences* 10(19):6757.
117. Alkassar Y, Agarwal VK and Alshrihi E (2017) Simulation of lamb wave modes conversions in a thin plate for damage detection. *Procedia Engineering* 173:948–955.
118. Wandowski T, Kudela P and Ostachowicz WM (2019) Numerical Analysis of Elastic Wave mode conversion on discontinuities. *Composite Structures* 215:317–330.
119. Wandowski T, Malinowski P and Ostachowicz WM (2019) Elastic wave mode conversion phenomenon in glass fiber-reinforced polymers. *International Journal of Structural Integrity* 10(3):337–355.
120. Fitzer E (1988) Composites for high temperatures. *Pure and Applied Chemistry* 60(3):287–302.
121. Liu X, Yu Y, Lomov S, et al. (2022) The numerical and experimental investigations for the curing monitoring of woven composites with Lamb Waves. *Measurement* 200: 111604.